NTNU
Norwegian University of
Science and Technology

Characterization of Aluminium Components Produced by Additive Manufacturing

Tobias Rønneberg

NTNU
**Norwegian University of
Science and Technology**

Characterization of Aluminium Components Produced by Additive Manufacturing

Tobias Rønneberg

Preface and Acknowledgements

This master thesis is submitted as a partial fulfilment of the requirements of the degree of Master of Science (MSc) in the field of Materials Science and Engineering at the Norwegian University of Science and Technology (NTNU). The work has been carried out at the Department of Materials Science and Engineering (IMT) between February and August of 2016. The work is a continuation of the project thesis of the same title presented for the course TMT4500 Materials Technology, Specialization Project in the fall of 2015. I hereby declare that the work presented in this master thesis has been preformed independently and in accordance with the rules and regulations of NTNU. However, there are many people that have contributed and deserve acknowledgement.

I would like to thank Eva Rise for her help with planning the laboratory work and ensuring it was done in a safe manner. In addition, wish to thank Torild Krogstad, Trygve Lindahl Schanche, Pål Christian Skaret and Yingda Yu for their help and technical expertise with regard to the experimental work. Further, I would like to thank Øystein Gjervan Hagemo and his colleagues at the workshop of the technical section of the Faculty of Natural Sciences and Technology at NTNU for their help with machining the components into test specimen.

This project would be impossible without the help of Vegard Brøtan at the Department of Production and Quality Engineering (IPK) at NTNU. I wish to thank him for his help with designing the components, his hard work to build them and his guidance throughout the last year.

Finally I would also like to show my gratitude to my supervisor Hans Jørgen Roven and co-supervisor Trond Furu for their guidance during the project.

<div align="center">

Trondheim, August 2016
Tobias Rønneberg

</div>

Characterization of Aluminium Components Produced by Additive Manufacturing

Tobias Rønneberg

Abstract

Additive manufacturing (AM) is a new method of manufacturing that can produce physical objects directly from CAD-models. Powder Bed Fusion (PBF) technology can produce metallic parts by selectively fusing powders layer by layer. The metallurgy and properties of such materials are still unknown, but they are clearly unlike equivalent parts produced by traditional manufacturing methods. Two aluminium alloys are investigated in this thesis; an Al-10%Si casting alloy and a 6061 wrought alloy. Both materials were received as powders and used to build a component in PBF process. Both powders and produced materials were characterized by microscopy and the mechanical properties of the materials were investigated.

The results show that the powders do not consitute an explosion hazard. Apropriate specimen preparaion can resolve the microstructure of the materials, which are various porosity. The porosity is characterized and quantified. Epitaxial microsturctures are found in both materials arising from solidification during production. That result has been observed before for the AlSi alloy, but not for the 6061 alloy. Due to the much lower alloying level of 6061, the structure is likely caused by the solidification conditions rather than the chemical composition. The 6061 alloy is mechanically far weaker than the AlSi alloy in compression and tension. This is partly attributed the large amount of cracks found in the alloy.

Karakterisering av Komponenter i Aluminium Fremstilt ved Additiv Tilvirkning

Tobias Rønneberg

Abstract

Additiv tilvirkning (AM) er en ny produksjonsmetode som kan bygge fysiske deler direkte fra CAD-modeller. Såkalte 'pulverbadmaskiner' kan produsere metalliske komponenter additivt ved å lagvis smelte sammen pulver. Forståelsen av slike materialer er fortsatt begrenset, men det er tydelig at metallurgien og egenskapene er forskjellige fra tilsvarende komponenter produsert ved tradisjonelle tilvirkningsmetoder. I dette studiet undersøkes to aluminiumlegeringer; en Al-10%Si støpelegering og en 6061 knalegering. Begge materialene ble mottatt som pulver og ble brukt til å bygge en modellkomponent i pulverbadmaskin. Både pulver og produsert materiale karakteriseres ved mikroskopi og mekaniske egenskaper i materialet utforskes.

Resultater viser at håndering av pulverene ikke innebærer høy brann- og eksplosjonsfare. Rett prøvepreparering kan fremheve strukturen i begge materialer. Disse inneholder mye porøsitet som karakterisers og kvantifiseres. Materialstrukturen på sub-mikronivå i begge materialer viser epitaksisk vekst ved størkning under produksjon. Dette er observert i AlSi-legeringen ved tidligere anledninger men ikke for 6061-legeringen. Da denne er mye lavere legert viser resultatet at strukturen er forårsaket av størkningsforhold heller enn kjemisk sammensetning. 6061-legeringen viser mye lavere styrke i strekk og kompresjon enn AlSi-legeringen, men dette er delvis pga høyt sprekkinnhold.

Contents

List of Figures

List of Tables

List of Abbreviations

2D   Two-dimensional. 5
3D   Three-dimensional. 3

AA6061   Name given to powder provided by LPW Technology Ltd. 36
AlMgSi   Aluminium-magnesium-silicon. 14
AlSi   Aluminium-silicon. 13
AlSi10Mg   Name given to powder provided by ConceptLaser GmbH. 36
AM   Additive Manufacturing. 1
ASTM   American Society for Testing and Materials. 3

BD   Building Direction. 8

CAD   Computer-Aided Design. 3

DMLS   Direct Metal Laser Sintering. 7

EBM   Electron Beam Melting. 7
EDM   Electrical Discharge Machining. 27
EDS   Energy-Dispersive X-ray spectroscopy. 30

F   Temper designation; as-fabricated condition. 12
FDM   Fused Deposition Modelling. 3

GP   Guinier-Preston. 15

H   Temper designation; cold-worked condition. 12
HAZ   Heat Affected Zone. 18
HPDC   High Pressure Die Casting. 25
HSE   Health, Safety and Environment. 26

ICP   Inductively Coupled Plasma. 25
IPK   Department of Production and Quality Engineering, NTNU. 36
ISO   International Organization for Standardization. 3

LENS   Laser Engineered Net Shaping. 7

MIG   Metal Inert Gas. 17
MLS   Micro Laser-Sintering. 7

NDT   Non-Destructive Testing. 27
NND   Nearest Neighbour Distance. 45
NTNU   The Norwegian University of Science and Technology. 36

O   Temper designation; annealed condition. 12
OM   Optical Microscope. 29

PBF   Powder Bed Fusion. 1
PEP   Propellant, Explosive and Pyrotechnic. 16

R&D   Research and Development. 1
RP   Rapid Prototyping. 3

SD   Scanning Direction. 10
SED   Secondary Electron Detector. 42
SEM   Scanning Electron Microscope. 25
SL   Stereolithography. 3
SLM   Selective Laser Melting. 7
SLS   Selective Laser Sintering. 7
SSSS   Supersaturated Solid Solution. 12

T1   Temper designation; cooled from fabrication temperature then naturally aged. 12
T2   Temper designation; cooled from fabrication temperature, cold-worked and naturally aged. 12
T3   Temper designation; solution-treated, cold-worked and naturally aged. 12
T4   Temper designation; solution-treated and naturally aged. 12
T5   Temper designation; cooled from fabrication temperature and artificially aged. 12
T6   Temper designation; solution-treated and artificially aged to peak strength. 12
T7   Temper designation; solution-treated and stabilized by overaging. 12
TD   Transverse Direction. 10
TEM   Transmission Electron Microscope. 30
TIG   Tungsten Inert Gas. 17

W   Temper designation; solution-treated condition. 12

List of Symbols

A	Area of a cross-section. 41, 46
B_{above}	Bit with surface of interest parallel to fabrication plane. 39
B_{side}	Bit with surface of interest normal to fabrication plane. 39
C	Circularity parameter. 42
C_0	Cylinder with length direction normal to the fabrication plane. 39
C_{45}	Cylinder with length direction 45° relative to the fabrication plane. 39
C_{90}	Cylinder with length direction in the fabrication plane. 39
E	Modulus of elasticity. 33, 78
F	Force. 46, 47
G	Temperature gradient at the rear of the fusion zone boundary. 22
H_0	Enthalpy at room temperature. 19
H_m	Enthalpy at melting point. 19
P	Length of perimeter. 41
Q	Quantity of heat applied to a weld. 19
R_N	Nominal crystal growth rate. 21
T	Temperature. 18
TT_0	Tensile specimen with length direction normal to the fabrication plane. 47, 78
TT_{45}	Tensile specimen with length direction 45° relative to the fabrication plane. 47, 78
TT_{90}	Tensile specimen with length direction in the fabrication plane. 47, 78
T_0	Initial temperature. 18
T_m	Melting point temperature. 22
T_p	Peak temperature (maximum temperature reached). 24
V_0	Initial volume. 46
$\Delta G°$	Change in Gibb's free energy at standard temperature and pressure. 15
ΔH_m	Latent heat of melting. 19
Δy_h	Hatching distance (distance between two parallel scanning lines). 9, 10, 34, 38, 84
Δz_{layer}	Layer thickness. 9, 34, 38, 83
α	Aluminium phase containing alloying elements in solid solution. 12
α	Angle between crystal orientation and welding direction. 21
$\bar{d}_{\text{powder}}$	Average powder particle size. 9, 41
β	Stoichiometric equilibrium phase Mg_2Si. 14
β'	Hardening precipitate in AlMgSi alloys (semi-coherent rods). 15

β''	Hardening precipitate in AlMgSi alloys (semi-coherent needles). 15
$\dot{V}$	Build rate of the PBF process. 34
γ_{AB}	Surface tension associated with the interface between phases A and B. 16
λ	Thermal conductivity. 18
ρ	Density. 18
σ	Stress. 46
σ_{UTS}	Ultimate tensile strength of a material. 11, 33, 78
σ_y	Yield strength of a material. 11, 33, 78
σ_{fl}	flow stress. 39, 77
θ	Contact angle in the sessile drop. 17
ε	strain. 46, 47
a	Diffusivity of heat. 18
c	Specific heat capacity. 18
d_0	Initial diameter. 46
$d_{\max}$	Maximum feret diameter. 41
$d_{\min}$	Minimum feret diameter. 41
d_{spot}	Spot size (focus diameter) of applied energy. 9, 38, 84
h	height. 46
h_0	Initial height. 46
n_3	Dimensionless operating parameter for fusion welding. 21
r	Distance from the heat source. 19
s	Stroke. 46
t	Time. 18
v	Speed of a moving heat source (welding speed or scanning speed). 9, 20, 38
v_{die}	Upper die speed. 46
d	Average grain size in Hall-Petch equation. 11
P	Power supplied by a heat source. 9, 20, 38
T_{FC}	Fabrication chamber temperature during production. 9, 38

1 Introduction

These are exciting times for design and manufacturing. Additive manufacturing (AM) is now often referred to as one of a series of disruptive technologies that could change the way we design products and set up new businesses [1]. In particular, a subset of AM processes known as powder bed fusion (PBF) shows promise to produce metallic products of similar or even superior properties to equivalent products produced by traditional manufacturing techniques [2]. The technology was first patented in 1984 [3, ch. 2.9] and the first commercial machine was released in 1992 [4, ch. 1.1]. Genuinely new methods of manufacture do not come along very often [1], so despite its novelty there is much industrial activity to prepare for implementation of AM [5].

There are still challenges to overcome. AM is currently only rarely cost-effective [6], but the greater challenge for wide adoption of AM is that the product material is not well understood [1]. Only a few materials have been studied in depth, but it is clear that AM produces materials with different metallurgical properties. Fundamental understanding of these materials is necessary before widespread adoption can occur.

As the most abundant metallic element on earth, aluminium's availability is practically infinite [7, ch. 14]. It is considered a green material because it can be recycled using only about 5% of the energy required to produce the metal from alumina. Aluminium alloys can be processed to have considerable strength and very high strength to weight ratios, thermal and electrical conductivity. This, along with its excellent corrosion resistance have allowed aluminium to replace other engineering materials (most notably steel) in many applications.

Aluminium has not received much attention from the AM community, despite its status as an important material for the future. This is likely because only a few AM aluminium alloys have been produced with satisfactory properties [8]. However, everything known about AM aluminium has been learnt very recently and much of what is published is unsubstantiated while the most reliable information is being privately generated and kept as commercial secrets [1]. As a result, knowledge regarding the fundamental metallurgy of AM aluminium is lacking.

It is now established that AM aluminium parts have completely different microstructures compared to cast or forged parts [9]. The mechanisms that produce these microstructures are not well understood, but they are thought to be related to the extremely high solidification rates associated with the PBF process [10]. Several studies have focused on process parameters to reduce the substantial porosity found in such AM parts [11]. Others have tried to optimize the production speed [12] or studied the effect of heat treatment [9]. In short, AM aluminium is still at a research and development (R&D) stage.

Objectives of the thesis

This thesis investigates two AM aluminium alloys. The first, commonly known as AlSi10Mg, is the most widely used and studied aluminium alloy for AM. It is an under-eutectic aluminium-silicon casting alloy containing 10 wt% silicon and small additions of other alloying elements. The second alloy is an aluminium-magnesium-silicon wrought alloy in accordance to alloy 6061 specification composition [13]. Both of these materials were received as gas atomized powders.

The experimental work in this thesis involves three phases. The first is to examine the powders to determine their geometry and size distribution. The second phase involves designing and producing a part of each material using a PBF process. The third and final phase of the experimental work is to characterize the produced material using various metallurgical methods.

The thesis seeks to study AM aluminium at several levels. There are therefore several different objectives, the first of which is to design a model suitable for material characterization of AM parts. The second objective is to characterize the materials produced of this model and determine some of their properties. There is a third objective linked with the second, as standards regarding characterization of AM materials are currently under development. Therefore the third objective is to evaluate various methods of characterization to find if any are particularly suitable for AM materials. The final aim of the thesis is to combine the experimental findings with established metallurgical theory to gain insight into the structure and properties of AM aluminium.

2 Background

2.1 Additive manufacturing

The term "additive manufacturing" is defined by the International Organization for Standardization (ISO) and the American Society for Testing and Materials (ASTM) as:

> **additive manufacturing (AM)**,n - process of joining materials to make parts from 3D model data, usually layer upon layer, as opposed to substractive manufacturing and formative manufacturing methodologies [14].

AM can be considered a family of manufacturing processes that abide by this definition. Such processes combine new developments from many engineering disciplines including computer-aided design (CAD), cybernetics and materials science. AM can also be considered a research field as all AM processes are relatively novel. In 1984, the first patents were filed for systems fabricating three-dimensional (3D) objects by selectively adding material layer by layer. Coincidentally, patents were filed almost simultaneously in the USA, France and Japan [3, ch. 2.9]. The technology has been developed ever since and numerous research institutes and companies have contributed to the field.

The AM field now includes many different process technologies [3, 4]. One of the first successful technologies was stereolithography (SL) where an ultraviolet-curable photopolymer liquid is selectively cured by lasers to form a solid object. Another successful technology is fused deposition modelling (FDM) where a solid filament is heated to a semi-liquid state and deposited as material layers. Several other technologies have been based on ink jet printing where either the material itself or a binding material is deposited onto a substrate via jetting heads. The technology showing the most promise for metallic materials is powder bed fusion (PBF) where powder layers are deposited onto a building platform and selectively sintered or fully melted in order to fuse together a solid object.

The initial market for AM was to produce accurate prototypes rapidly and cheaply for product development, and was formerly known as rapid prototyping (RP) [4, ch. 1]. For this reason, many early AM processes focused on polymers. However, new AM processes enable production of a large variety of materials. PBF processes alone can produce parts from polymers, metals, ceramics and composites [3, ch. 5.2]. Some of these new AM processes can manufacture products with similar or even superior mechanical properties compared to traditional manufacturing [2]. For this reason, AM has received much attention from the media as an industry that could potentially supplant traditional manufacturing [15]. Although the industry itself has settled on the name 'Additive Manufacturing', media have often preferred to use the term '3D printing'.
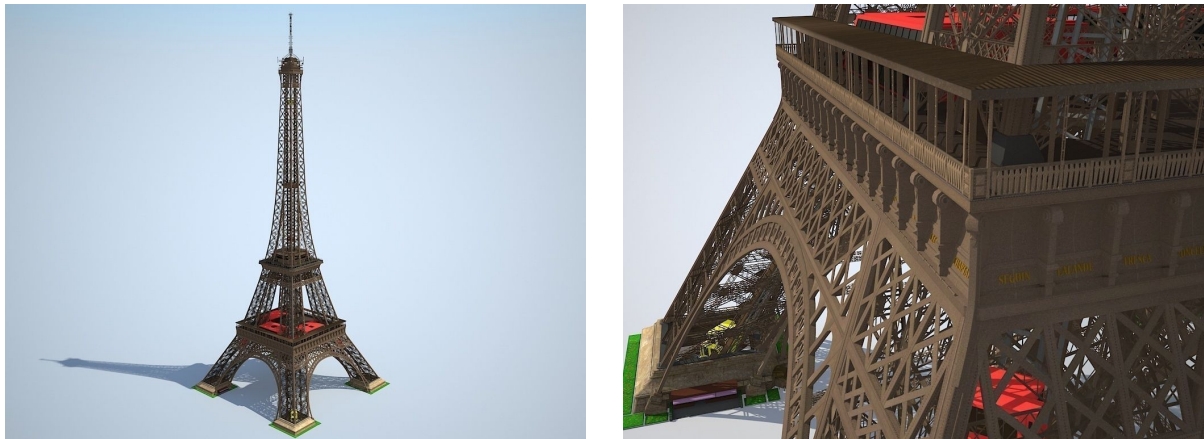
(a) Overview.

(b) Details.

Figure 2.1: CAD model of the Eiffel Tower.

Source: CGTrader [16]

2.1.1 The generic additive process

Although AM is a term describing a wide set of processes, a generic process has been established [3, 4]. A description of a simplified four step generic process is given below. Each step is illustrated using the example of making a model of the Eiffel Tower in plastic using an FDM process.

Step 1: Computer model

Every AM process starts by making a 3D model of the part using CAD. The design may be completely computer-generated or based on physical objects using scanning equipment. CAD models are always vector graphics, meaning such models are infinitely scalable and can include very fine details. Figure 2.1 shows a CAD model of the Eiffel Tower. As can be seen from figure 2.1b, very fine details are included in the model.

Step 2: Pre-production

The second major step in any AM process is to prepare the CAD model for manufacturing. This involves a series of steps and varies depending on the AM process parameters as well as the part. The CAD model is converted to a file type that describes the geometry as a set of closed surfaces, commonly known as a polygon mesh. The model is scaled, oriented and positioned relative to a fabrication platform.

Most AM processes have two limitations to spacial resolution. The first is the layer thickness, meaning the resolution in the direction normal to the fabrication platform. The second is the in-plane resolution which depends on the AM process. There are also limitations to the geometry that can be produced which are related to the material properties. Limitations to wall thickness or curvature are imposed to avoid collapse during manufacturing. Temporary support structures are often added to models of complex geometries. Such support structures are removed during post-processing.
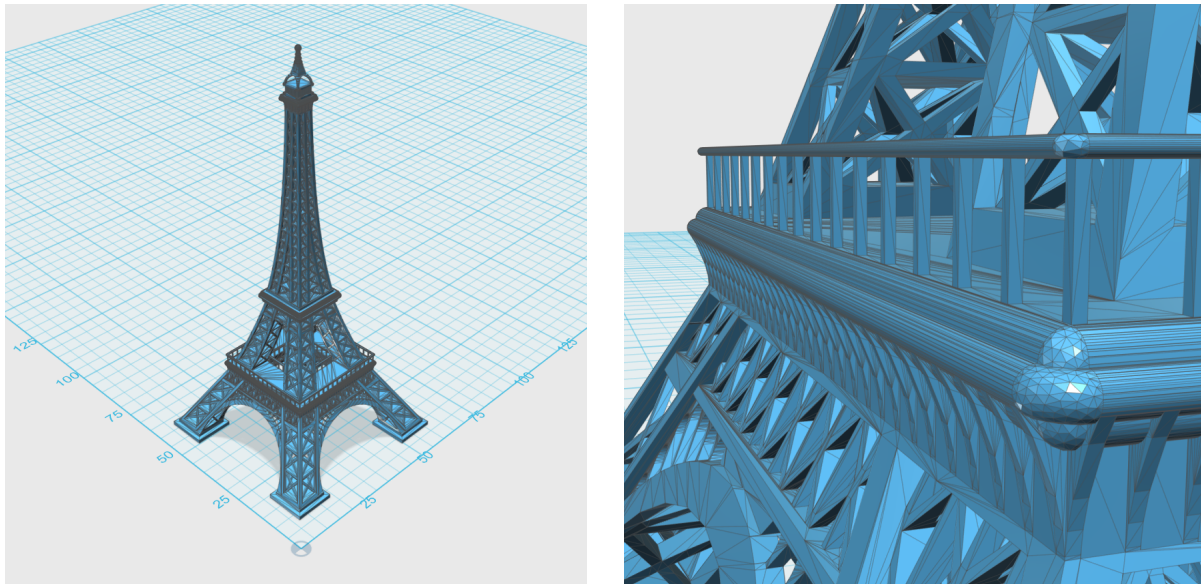
(a) Overview.   (b) Details.

Figure 2.2: Eiffel Tower model during the pre-build step.

Source: Thingiverse [17]

Once modifications are completed, the new model is sliced into two-dimensional (2D) cross-sections parallel to the fabrication platform plane. These cross-sections of uniform thickness constitute the layers that form the object. All the information regarding the layers, stacking order and other required data are contained in a digital file sent to the AM machine ready for production.

Figure 2.2 shows a 3D model of the Eiffel Tower being prepared for AM. Figure 2.2a shows how the model is scaled and oriented relative to a fabrication plane. Notice in figure 2.2b that the model consists of polygons. When comparing figures 2.1 and 2.2, it is clear that some fine details from the CAD model have been omitted to make the production possible.

Step 3: Production

With the layered model data prepared, the next step is to set up the machine chosen for building the part. The settings will depend on the type of machine (and hence AM technology) used, and they are often related to the modifications in the pre-production step. Settings such as material constraints, layer thickness, spacial resolution and timing are set.

All AM machines require input materials. These will of course include the material from which the part can be made, such as plastic filament for FDM processes or photopolymer liquid for SL. Other supplementary materials may also be required, such as an inert gas used to avoid excessive oxidation in PBF processes.

Building the part is to a large degree an automated process, requiring only monitoring of the machine to ensure no errors occur. The building process is for most AM processes very time consuming, particularly for large parts with much bulk material. There is often a trade-off between building time and the resolution of the part. Figure 2.3 shows a model
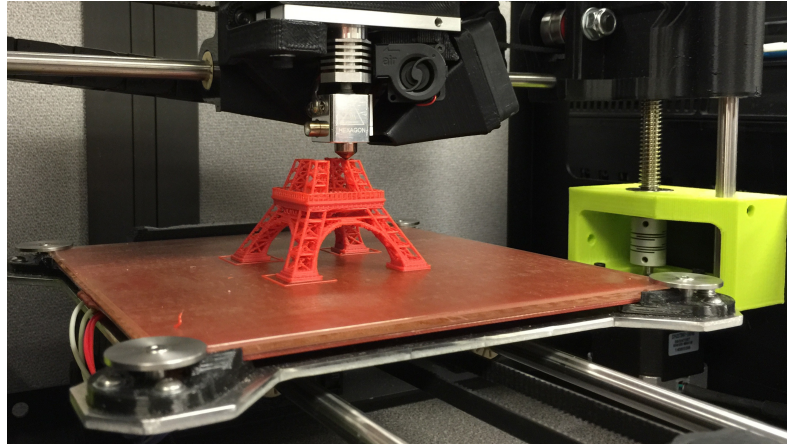
Figure 2.3: FDM building of Eiffel Tower.

Source: Mearian [18]

of the Eiffel Tower being built using a relatively quick FDM process. According to the source article, the 13 cm tall model took 1 hour and 44 minutes to build.

Step 4: Post processing

Nearly all AM processes require some post processing after building the part before it is ready for applications. Most AM processes require manual removal of the part from the machine and the building platform. Liquid-based processes such as SL usually require a rinsing step as well as a curing step. Support structures are usually manually removed after production. Other post processing includes cleaning, sanding, heat treatment, coating and other surface finishing. Figure 2.4 shows the completed Eiffel Tower part removed from the fabrication platform.

Figure 2.4: AM model of the Eiffel Tower.

Source: Thingiverse [17]

Company	Technology name	Country
3D systems	Selective Laser Sintering (SLS)	USA/France
EOS	Micro Laser-Sintering (MLS)	Germany
Optomec	Laser Engineered Net Shaping (LENS)	USA
Arcam	Electron Beam Melting (EBM)	Sweden
ConceptLaser	LaserCUSING	Germany
Renishaw	Metal additive manufacturing	UK
SLM Solutions	Selective Laser Melting (SLM)	Germany
Stratasys	Direct Metal Laser Sintering (DMLS)	USA

Table 2.1: Prominent suppliers of PBF equipment.

Collected from numerous sources: [3, ch. 5.6], [4, ch. 5], [19] and [20]

2.1.2 Powder bed fusion

The first PBF process was commercialized in 1992 [4, pp. 193]. Since then a number of companies have developed their own versions of the process and given them new names. Some of the most prominent suppliers of PBF technology are listed in table 2.1. Despite all the different names, all PBF processes share three characteristics [3, ch. 5.1]:

1. One or more energy sources for fusing the powder.

2. A system to focus and move the energy source in a pattern.

3. A mechanism for adding and smoothing layers of powder.

Process overview

A generic PBF system is described in figure 2.5. In figure 2.5a the initial stage of the process is shown where the fabrication platform is set at its uppermost position. Powder from the powder supply is deposited as a thin and even layer atop the fabrication platform. The figure shows a roller doing this action, but there are several other deposition mechanisms available. The energy source and scanning system are then deployed to fuse together the bottom layer of the part.

(a) Initial stage. (b) Final stage.

Figure 2.5: Powder bed fusion process.

Source: Adapted by author from Chua and Leong [4, figure 5.2]
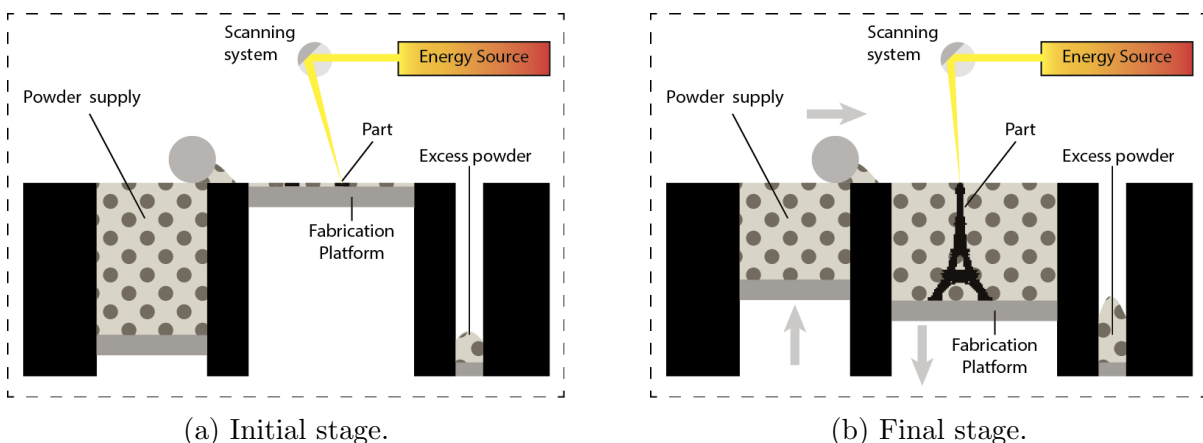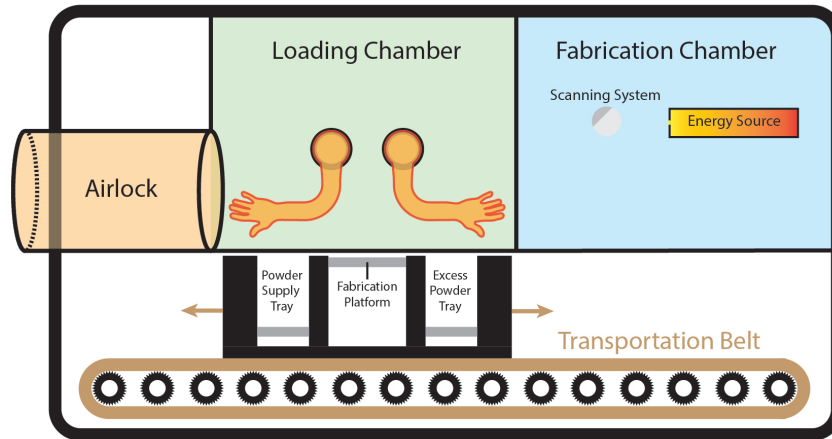
Figure 2.6: Compartments of a PBF machine.

Once the first layer is fused, the platform is lowered a distance equal to the layer thickness. The powder distribution system is again called into action to deposit a new powder layer atop the previous layer. Then the energy source and scanning system are deployed to fuse the second-most bottom layer of the part. The energy is sufficient to fuse both the powder as well as he underlying layer together. This process is repeated for every layer until the part is completed, as can be seen in figure 2.5b. The convention is to use a coordinate system in which the building platform surface is the xy-plane and the part is built in the positive z-direction known as the building direction (BD).

The energy source provides sufficient power to melt the powder. For many materials this is also sufficient power to cause a reaction between powder material and the surrounding atmosphere. The system is therefore enclosed and filled with an inert gas (symbolized by the dashed box in figures 2.5a and 2.5b). The enclosed chamber is usually called the 'building chamber' or 'fabrication chamber' and several PBF machines can adjust the temperature within the chamber during production. Unmelted powder will follow the part downwards during production, reducing the need for support structures. This unmelted powder can be recycled, making PBF processes very efficient with regard to material consumption.

Due to the reactivity of metallic powder materials, PBF machines are usually equipped with three compartments; an airlock, a loading chamber and a fabrication chamber (see figure 2.6). Powders inside sealed containers are placed in the airlock where the atmosphere is changed to an inert gas. Then the containers are moved into the loading chamber where powder is loaded into the powder supply tray. The operator also mounts the fabrication platform using the gloves. Once this is done the powder and fabrication platform are moved to the fabrication chamber where the part is produced. Once finished, the trays are moved back to the loading chamber where unmelted powder is removed to sealed containers again ready for reuse. The part and fabrication platform (now fused together) are placed in the airlock before they can be taken out of the machine for post processing.

Process parameters

Optimal process parameters have proved vital for producing satisfactory materials using PBF systems. There are many such parameters and several are mutually interacting. Nonetheless they may be lumped into four categories [3, ch. 5.4]:

- **Heat source and scanning system:**
  All parameters related to the energy prior to reaching the powder layers. These include heat source power P, spot size d_{spot}, pulse duration etc.

- **Powder and deposition:**
  Parameters concerning the powder and its deposition onto previous layers. These include various material properties, particle shape, average particle size $\bar{d}_{\mathrm{powder}}$, powder bed density and layer thickness $\Delta z_{\mathrm{layer}}$.

- **Scanning:**
  Parameters related to the movement of the heat source as each layer is fused, such as scan speed v, hatching distance Δy_h and scan pattern.

- **Temperature:**
  Parameters related to the temperature at various places during production, including the powder bed, feeder and storage as well as the fabrication chamber T_{FC}.

The quality of PBF systems have been greatly improved in the last decade in part due to the arrival of new heat sources. In particular, industrial yttrium fibre lasers that provide high beam quality at a wavelength well absorbed by metals have been adobted widely [1]. Most PBF systems use such lasers, but also electron beams have been successfully implemented as the energy source [4, ch. 5.5]. The laser can be focused onto the powder (via the scanning system) where the energy is spread according to a Gaussian distribution in the fabrication plane. The 'spot size' is a measure of the size of the area where the heat is applied (the focs diameter), often defined as three times the standard deviation of the energy distribution [21].

The powder geometry affects flow during deposition, which in turn affects layer thickness. The powder size distribution affects the packing factor, as smaller particles can fill voids between larger particles to increase the powder bed density. Powder suppliers therefore make spherical powders of sizes within a specific size range.

Scanning strategies

The manner in which powder is fused together is a complex procedure. It is common to use different sets of process parameters for different sections of the part. Each set of process parameters is called a 'mode' and several modes are used for each layer. The way these modes are applied constitutes the scanning strategy of the building process. The most common modes are contour and fill. Once a powder layer has been deposited, the contour mode is used to fuse the contour of the layer pattern. This will be surface material of the product. Then the inside of the contour is fused using the fill mode (sometimes called 'core'-mode) to form the bulk material. The process parameters of the contour and fill modes are optimized to produce desirable properties of the surface and bulk material respectively.
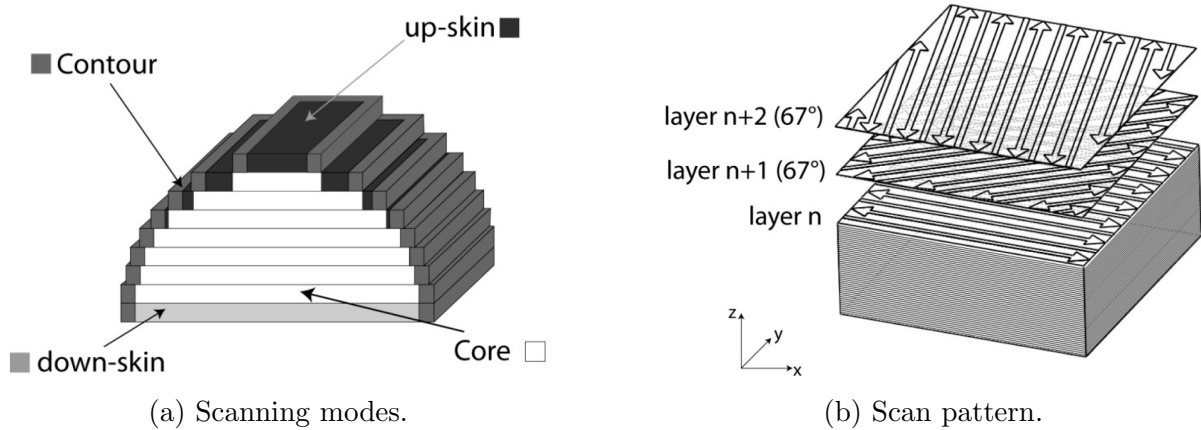
(a) Scanning modes.   (b) Scan pattern.

Figure 2.7: Scanning strategy parameters.

Source: Manfredi et al. [23, figure 1]

Other modes are illustrated by figure 2.7a. The 'up-skin' material is surface material facing upwards (resting on bulk material below). Meanwhile, 'down-skin' material is surface material facing downwards and therefore rests on unmelted powder. Up-skin and down-skin modes are often applied for two or three layers of a part's top and bottom surfaces [22]. Thus the contour mode only applies to surfaces normal to the xy-plane, while up-skin and down-skin are in the xy-plane.

The fill mode is used for most of the production time as there is far more bulk material than surface material in most geometries. This mode also has some additional complexity known as the fill pattern. For this we define two new directions in addition to the already defined building direction (BD). The scanning direction (SD) is the direction in which the heat source is moved through the powder, while the transverse direction (TD) is normal to the scanning direction in the xy-plane. When describing these directions it is common to reorient the coordinate system so that the SD is parallel to the x-direction and the TD is parallel to the y-direction (the building direction remains parallel to the z-direction). The pattern is filled by raster scanning, either unidirectionally or more commonly bidirectionally (back an forth).

The distance in the transverse direction between the centerlines of two scanning lines is known as the hatching distance Δy_h. This hatching distance must be smaller than the fused width of each scanning line to ensure good fusion between parallel lines. For good fusion between layers, the coordinate system is often rotated about the building direction between layers (see figure 2.7b). Given that the fused zone penetrates several layers in the fill mode, this technique of rotating between layers avoids columns of unmelted or poorly fused material in the product.

Another commonly used technique in the scanning pattern is to divide the bulk area of a layer into smaller shapes (usually squares) known as 'islands'. This is illustrated in figure 2.8. Each island is filled separately in a random order, allowing heat from one island disperse into underlying material while the heat source fuses another island. This technique thus avoids accumulation of heat in one area. In addition, the practice of shifting the positioning of the islands for each layer has been adopted to avoid columns of poorly fused material.
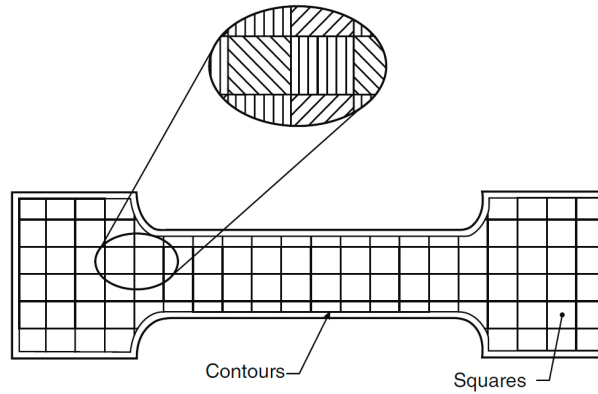
Figure 2.8: Fill technique using islands.

Source: Gibson, Rosen, and Stucker [3, figure 5.7]

2.2 Aluminium alloys

Aluminium is a light metal with a density of 2.70 g/cm^2. It has an fcc unit cell with a lattice parameter of 0.404 nm [24, ch. 3.1]. High purity aluminium has an annealed yield strength (σ_y) of 7-9 MPa and an ultimate tensile strength (σ_{UTS}) of 47 MPa, which is too low for structural applications. Additional elements are therefore added to increase the strength, most commonly Mg, Si, Cu, Mn and Zn. The final properties of an alloy depend on various processing steps as well as the chemical composition [25, ch. 2.1].

Aluminium alloys are often categorized by method of manufacture where one distinguishes between casting alloys and wrought alloys. Casting alloys are cast into their final shape and thus endure only limited mechanical deformation during production. Wrought alloys on the other hand are first cast into ingots and then formed into their final shape by a metal forming process such as forging, extrusion, rolling, etc. By their nature, metal forming processes require heavy deformation of the material. The composition of aluminium alloys is generally optimized for both the forming process as well as the final application. Further details regarding categorization of aluminium alloys can be found in literature [7, 24, 26].

2.2.1 Strengthening mechanisms

Five separate strengthening mechanisms can be applied to aluminium alloys [26, ch. 2]; grain size control, strain hardening, solid solution alloying, second phase formation and precipitation hardening. Grain size control applies to all aluminium alloys as well as pure aluminium. It is based on the general rule that the strength of a metal is reduced as the average grain size (d) increases. The relationship between the yield strength and the average grain diameter is given by the Hall-Petch equation (equation 2.1) where σ_0 and K are constants specific for the metal.

$$\sigma_y = \sigma_0 + K \cdot d^{-1/2} \tag{2.1}$$

The grain size should be controlled during production by discouraging excessive grain growth which would lead to low strength. Once a material has been fabricated it can

Designation	Description
F	As-fabricated (hot-worked, forged, cast, etc).
O	Annealed (in the softest possible condition).
H	Cold-worked.
W	Solution-treated.
T1	Cooled from fabrication temperature and naturally aged.
T2	Cooled from fabrication temperature, cold-worked and naturally aged.
T3	Solution-treated, cold-worked and naturally aged.
T4	Solution-treated and naturally aged.
T5	Cooled from fabrication temperature and artificially aged.
T6	Solution-treated and artificially aged to peak strength.
T7	Solution-treated and stabilized by overaging.

Table 2.2: Selected heat-treatable alloy designations.

Source: Askeland and Phulé [7, table 14-4]

usually be strengthened by deformation, otherwise known as strain hardening or cold-working. This is essentially refining the grain structure by crushing large grains into smaller and finer grains, adding strength as per the Hall-Petch equation.

Alloying elements contribute to strengthening aluminium in different ways. Elements in solid solution with aluminium (usually referred to as the α-phase) strain the crystal structure and thus strengthen the material as dislocation movement becomes more demanding. If the concentration of alloying elements is greater than the limit of solid solubility, secondary phases will form under equilibrium conditions. Phase boundaries also discourage dislocation movement and thus give strength to the material.

Alloys are said to be heat-treatable if the system contains one equilibrium solid phase at elevated temperature but several phases at room temperature. Such alloys may be solution treated to a single phase at elevated temperature, then quenched (rapidly cooled) to room temperature. This treatment does not facilitate equilibrium conditions, but instead all alloying elements are in one supersaturated phase known as supersaturated solid solution SSSS. Over time the alloying elements will precipitate (known as 'aging') towards equilibrium. At room temperature this process is known as 'natural aging' and is often very slow due to low diffusion rates. By instead heat treating the alloy at an elevated temperature below the solvus line, diffusion can be accelerated and the precipitation can be controlled. When precipitates have reached a desirable size, the temperature is quickly dropped giving the material a stable precipitate size. Such heat treatments are known as 'artificial aging'.

Heat-treatable alloys usually contain alloying elements that produce inter-metallic compounds that are very hard. By controlling their precipitation, the soft α-phase contains homogeneously distributed hard precipitates. This gives the material great strength while simultaneously providing high ductility, and is commonly known as 'precipitation hardening'. To describe the state of a heat-treatable alloy, various designations are used. A number of the most commonly used designations are shown in table 2.2.
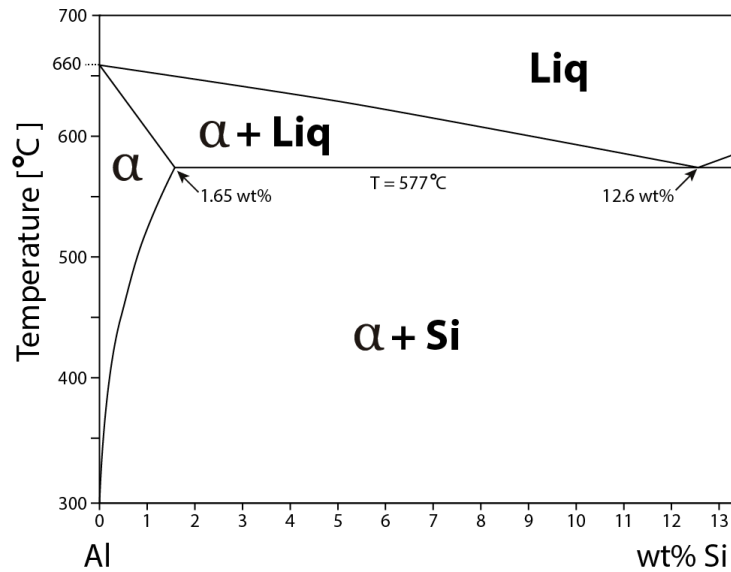
Figure 2.9: Phase diagram for common AlSi alloys.
Source: Adapted by author from Baker et al. [27, section 2.6.82 Al-Si]

2.2.2 AlSi casting alloys

Aluminium-silicon (AlSi) are among the most used aluminium alloys, both as wrought alloys (4xxx-series) and as casting alloys (4xx.x-series) [24, ch. 3.4.4 and 3.5.1]. They contain between 4 and 13% silicon, which is found both in solid solution and as silicon particles. Figure 2.9 shows the phase diagram for this concentration range. The eutectic point is found at 12.6 wt% silicon and the resulting equilibrium microstructure consists of coarse silicon rods in an aluminium matrix. However, the microstructure can be refined by greater undercooling or by small additions of sodium or strontium (about 0.002 wt%). Note that the solubility limit of the α-phase is very low at room temperature.

There are several reasons why AlSi alloys are well suited for casting. The viscosity of the melt is lowered by silicon resulting in good fluidity, and silicon expands during solidification to counteract the shrinkage of aluminium. This gives the alloy good mould filling ability. The lowest viscosity is found for near-eutectic compositions, which also have small solidification intervals. This is important as short dendrite arms do not significantly block the flow of melt. Alloys with large solidification intervals are found to have evenly distributed microporosity caused by long dendrite arms blocking the melt from flowing to cavities.

Silicon increases the corrosion resistance of the alloy in alkaline environments as silicon enters into the protective oxide layer. For this reason, AlSi alloys are often used in marine applications. As silicon is also a light element, such alloys are often used to cast components such as gearboxes and radiators for the automotive industry. Small additions of copper or magnesium are often added to further increase the strength of AlSi casting alloys, designated as the 3xx.x-series. Such alloys are often age-hardenable [7, ch. 14].
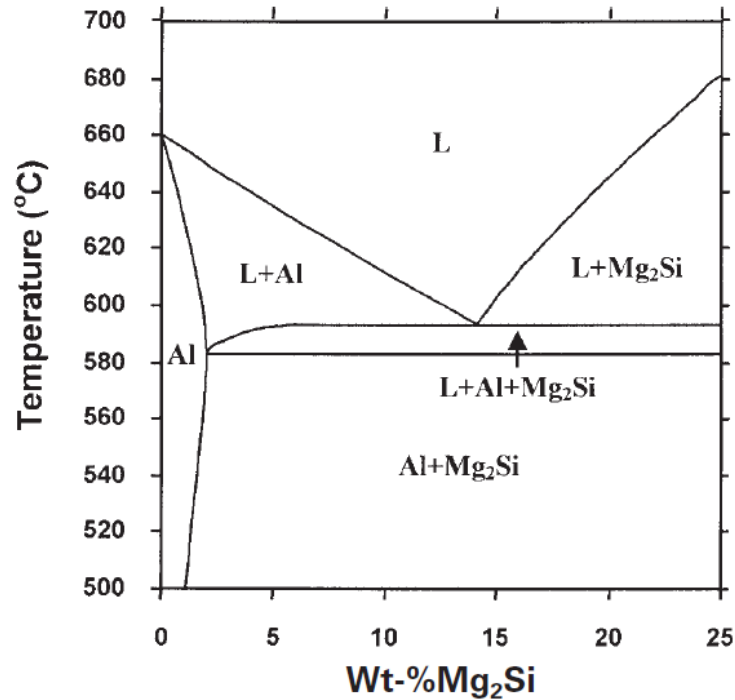
Figure 2.10: Pseudobinary phase diagram for Al-Mg$_2$Si.
Source: Zhang et al. [28, figure 3]

2.2.3 AlMgSi wrought alloys

Aluminium-magnesium-silicon (AlMgSi) alloys are heat treatable alloys containing two major alloying elements; about 0.5-1.3 wt% magnesium and 0.4-1.4 wt% silicon. Manganese and chrome are often added for grain refining, and copper for increased strength [24, section 3.6.3]. Such alloys are commonly known as the 6xxx-series of wrought alloys. About half of all aluminium extruded products are made using AlMgSi alloys. Such alloys are also applied in the automotive and transport industry because of the good strength to weight ratio. At equilibrium, AlMgSi alloys will contain an equilibrium phase β which is the stoichiometric inter-metallic compound Mg$_2$Si. Such an alloy is said to be 'balanced' if equation 2.2 is satisfied. A pseudobinary phase diagram can be constructed for AlMgSi alloys using this equilibrium phase (see figure 2.10). The solubility of Mg$_2$Si in aluminium at 583.5°C is 1.91 wt%.

$$\frac{\text{wt\% Mg}}{\text{wt\% Si}} = 1.73 \qquad \Longleftrightarrow \qquad \frac{\text{at\% Mg}}{\text{at\% Si}} = 2 \qquad (2.2)$$

AlMgSi alloys are heat treatable and not designed to be used at equilibrium. Instead they are heat treated to a metastable state of greatest strength (the T6 condition). The Mg$_2$Si content should be less than the peritectic point in order for heat treatments to be effective. Such heat treatments consist of several steps. The first is solution-treatment at a temperature between the solvus and solidus lines, usually performed at around 530°C for 30 minutes. The solution heat treatment is followed by quenching to room temperature whereby all alloying elements are in the supersaturated α-phase. The second step is artificial aging at a temperature below the solvus line. This most commonly performed in the range 150-190°C where the alloy is held for several hours. This facilitates precipitation
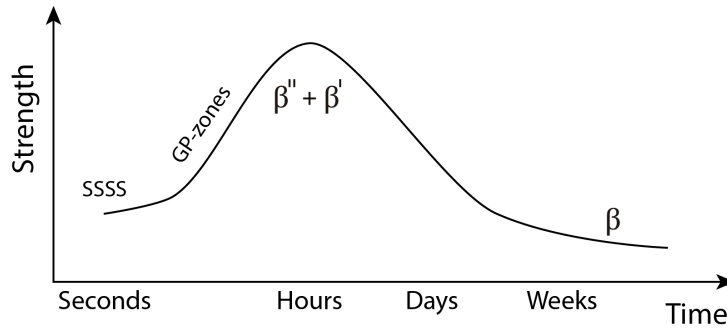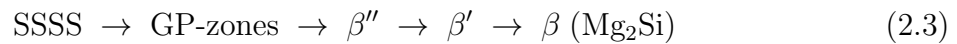
Figure 2.11: AlMgSi alloy strength vs precipitation sequence.

Source: Adapted by author from Blommedal [29, figure 2.2]

of larger metastable phases, which form in a sequence with increasing holding time. The precipitation sequence for a balanced alloy can be described by equation 2.3 [24].

$$\text{SSSS} \ \rightarrow \ \text{GP-zones} \ \rightarrow \ \beta'' \ \rightarrow \ \beta' \ \rightarrow \ \beta \ (\text{Mg}_2\text{Si}) \tag{2.3}$$

Guinier-Preston-zones or GP-zones are thought to be monoclinal and semi-coherent needles along the <100>-directions in aluminium. These are very small, being a few angstroms in diameter and a few nanometers in length. β'' is also a phase of monoclinal semi-coherent needles along the <100>-directions, but larger than GP-zones and thought to have a stoichiometric composition of $\text{Mg}_5\text{Al}_2\text{Si}_4$. β' is a hexagonal phase of semi-coherent rods larger than the β''-needles. The β' phase is thought to have the composition $\text{Mg}_{1.8}\text{Si}$. The final phase in the sequence is the equilibrium phase β of composition Mg_2Si. This phase is cubic and forms incoherent rectangular plates.

Figure 2.11 shows the evolution of AlMgSi alloy strength with the precipitation sequence. Prior to artificial aging, the strength is given as SSSS. As GP-zones precipitate, the strength increases until the peak strength (the T6 condition) is observed as the β'' phase is transformed into β'. The strength then decreases as the equilibrium phase β is precipitated (the overaged condition T7). Note that the strength of the solution treated condition (the W condition) is also greater than the strength of the overaged condition.

2.3   Oxidation of aluminium

$$2 \, Al \, (s) \ + \ 3 \, O_2 \, (g) \ \rightarrow \ Al_2O_3 \, (s) \ + \ 1676 \, kJ \tag{2.4}$$
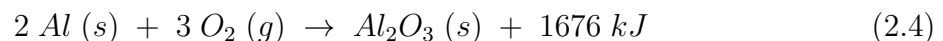
In an atmospheric environment of oxygen gas, aluminium metal will react according to equation 2.4. This reaction is spontaneous ($\Delta G^\circ = $ -1582 kJ/mol [30]) and the oxide product adheres closely to the aluminium surface. A thin film forms which is not easily permeable to ions. The oxide layer will therefore protect the underlying aluminium metal from further corrosion which is the reason why aluminium and its alloys have exceptional corrosion resistance. The oxide film is estimated to be 2-10 nm in thickness for air-exposed aluminium [31, ch. 21].

The reaction described in equation 2.4 is very exothermic. Normally this heat dissipates in the underlying metal or is removed by convection currents above the surface. Because

the oxide film is very thin, the total amount of heat generated by the film formation is insignificant for most aluminium parts. However, this is not the case for fine powders. As powder size decreases, the ratio of surface area to volume increases. When the powder reaches a critical size, the heat from reaction 2.4 is sufficient to heat the inner metal to expand and break the oxide film. This exposes more aluminium metal and causes a chain reaction by which all the aluminium metal will react. The oxidation of aluminium powders produces extraordinary amounts of heat which is why aluminium powders are used in the propellant, explosive and pyrotechic (PEP) industries. The critical size is thought to be around 40 μm, but aluminium powders used in PEP industries are generally much smaller than this [32].

$$2\,Al\,(s)\ +\ 3\,H_2O\,(l) + \frac{3}{2}\,O_2\,(aq)\ \rightarrow\ 2\,Al(OH)_3\,(s)\ +\ 1694\,kJ \qquad (2.5)$$
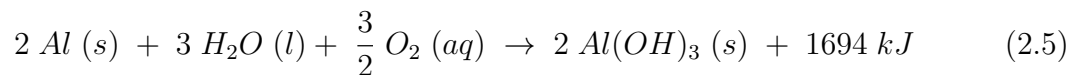
Aluminium will oxidise rapidly in an aqueous environment with dissolved oxygen according to reaction 2.5. This reaction is also highly spontaneous (ΔG° = -1841 kJ/mol [30]). If no continuous protective film is formed around the aluminium, particles may react until there is no more metallic aluminium left.

2.4 Solid-liquid interactions

Consider bonding between a liquid and a solid when they are of closely similar composition. Perfect contact between the two phases is obtained if heat from the liquid partially melts the solid. The original and newly formed liquids will mix and the resulting liquid can solidify along the new phase boundary. This leads to good bonding in the solidified material. If the contact between the phases is not perfect, the bonding will be poor and what is known as 'lack of fusion' occurs during solidification.

Lack of fusion is caused by the lack of a clean and smooth surface to which the liquid may bond. This may be caused by insufficient heat in the liquid to melt the solid material. In such cases the surface will be rough and capillary forces can oppose perfect contact. Another source of lack of fusion is an unclean solid surface. Oxides and other surface films can deter good bonding between the liquid and solid. This is why surfaces are usually cleaned prior to welding [33, ch. 1.4.1].

Every surface between two phases A and B has an associated surface tension γ_{AB} usually expressed as force per unit length or energy per unit area. For crystals, this surface tension
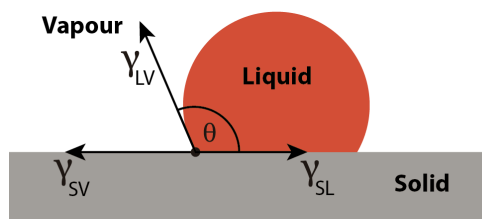

Figure 2.12: Sessile drop.

Source: Adapted by author from Lancaster [33, figure 1.10]

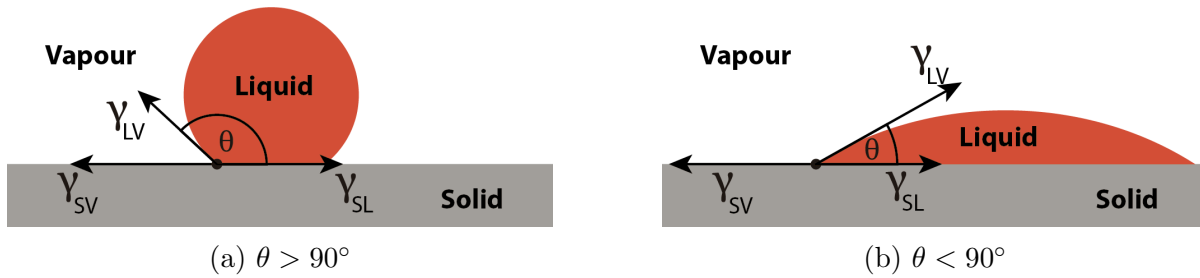(a) $\theta > 90°$ (b) $\theta < 90°$

Figure 2.13: Sessile drops with high and low contact angles.

Source: Adapted by author from Lancaster [33, figures 1.10 and 1.11]

(also known as surface energy) is equated to the work done in separating two adjacent crystallographic planes. This work is usually positive, meaning energy is required to make the surface. High surface tension equates to an unstable surface which a liquid will strive to minimize.

Figure 2.12 shows the case of a liquid drop resting on a plane solid surface, commonly called the sessile drop. The three phases involved are a solid, a liquid and a vapour gas. Between these phases are surfaces of surface tensions γ_{SV}, γ_{SL} and γ_{LV}, where the subscripts denote the first letter of the phases. The figure shows the forces acting on a point where all the surfaces meet. As this system is at rest, an equilibrium of the horizontal forces can be expressed by equation 2.6.

$$\gamma_{SV} = \gamma_{SL} + \gamma_{LV} \cos \theta \tag{2.6}$$

The angle between the solid-liquid surface tension and the liquid-vapour surface tension is known as the contact angle θ [33, ch. 1.4.2]. This is an important parameter as it describes the ability of the liquid to wet the solid. A high contact angle ($\theta > 90°$) means the liquid opposes wetting the solid surface and is only forced to do so by gravity (see figure 2.13a). A low contact angle means the liquid can wet the solid surface well, which is a requirement for good bonding during solidification.

2.5 Fusion welding of aluminium

Welding can be described as the joining of two components by a coalescence of the surfaces in contact with one another. The most common way to achieve this between aluminium parts is by fusion welding. In such processes energy is supplied at the contact boundary of components in order to melt nearby material. Liquid from the two parts mixes and solidifies to generate one continuous material. A principle sketch of the process is shown in figure 2.14.

Several different fusion welding technologies are available for joining aluminium. The most common are arc welding techniques such as metal inert gas (MIG) and tungsten inert gas (TIG)-welding. Such processes generate an electrical arc between an electrode and the part to be welded known as the work piece. This arc provides the energy for local melting. Other fusion welding processes use different heat sources such as jets of electrically ionized gas (plasma), lasers or electron beams. In all fusion welding processes, energy is

(a) Initial setup.   (b) Local melting.   (c) After solidification.
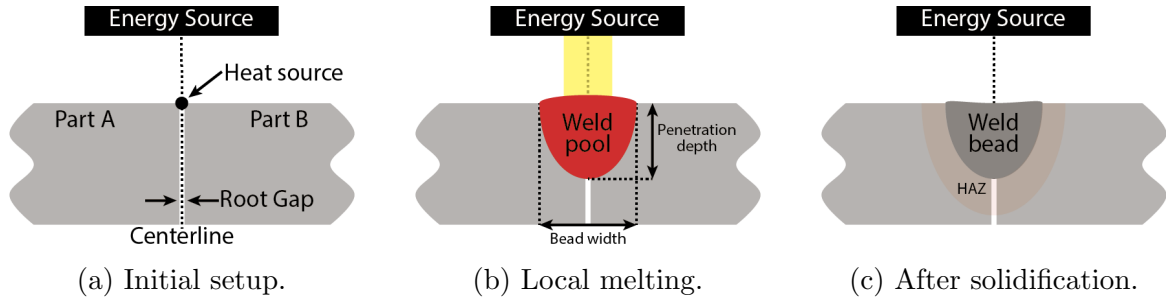
Figure 2.14: Principle sketch of a fusion welding process.

concentrated onto a small part of the work piece surface which allows for controlled local melting.

The nomenclature of welding is extensive and can be found in literature [26, 33, 34]. A short summary of the most essential welding terminology is given here. Figure 2.14a shows a setup called a butt weld where parts A and B are in close contact separated by a root gap. We assume the parts are made of the same material, variably called the base metal, parent metal or work piece. The centerline in the middle of the root gap intersects the workpiece surface at a point known as the heat source. This will be the center of the area where energy is applied.

Local melting will occur around the heat source when energy is applied. In liquid state the melted material is known as the weld pool in an area called the fusion zone. After solidification the weld pool is called the weld bead. The weld pool has a depth and width as shown in figure 2.14b. Heat is conducted away from the weld pool and dissipates into the workpiece. The material near the weld pool where the metallurgical structure is significantly changed due to the heat is known as the heat affected zone (HAZ). The weld bead and HAZ areas combined is known as the weld zone.

Because of the high energy input, oxidation of the weld is a serious concern. To avoid oxidation, fluxes or shielding gases are applied prior to or during welding. Fluxes are mineral compounds to be mixed into the weld pool to react with nonmetallic inclusions. Shielding gas is used to remove oxygen (and other reactive gases) from the weld pool surface while it is most susceptible to oxidation.

If the heat source remains stationary the weld is called a spot weld. However, the heat source is usually moved along a path known as a weld pass. The velocity of this movement is called the welding speed, and this is a very important parameter in welding.

2.5.1   Heat flow

$$\nabla^2 T - \frac{1}{a}\frac{\partial T}{\partial t} = 0 \qquad\qquad a = \frac{\lambda}{\rho c} \qquad\qquad (2.7)$$

Consider first a stationary heat source applied to a butt weld. The root gap is negligible and initially the temperature of work piece is T_0. A simple model of the heat flow of the system can be described by the heat equation given in equation 2.7. T and t denote temperature and time respectively. a denotes the diffusivity of heat, which is equal to the thermal conductivity λ divided by the product of the density ρ and the specific heat c.

Property	λ	a	ρc	T_m	H_m-H_0	ΔH_m
Value	0.230	85	0.0027	660	1.73	0.8
Unit	W/(mm $\cdot$°C)	mm^2/s	J/(mm$^3\cdot$°C)	°C	J/mm^3	J/mm^3

Table 2.3: Physical properties of pure aluminium related to heat flow.

Source: Adapted by author from Grong [35, table 1.1]

Values of relevant physical properties for pure ($> 99\%$) aluminium are found in table 2.3. The values will vary for different aluminium alloys, and may not necessarily be isotropic for processed materials. However, the following will assume isotropic thermal properties of the work piece. Now further assume a quantity of heat Q is applied instantaneously at the heat source. By solving the heat equation with this information, the temperature at time t and distance r from the heat source can be found by equation 2.8.

$$T - T_0 = \frac{Q}{\rho c(4\pi at)^{3/2}} \exp\left(\frac{-r^2}{4at}\right) \tag{2.8}$$
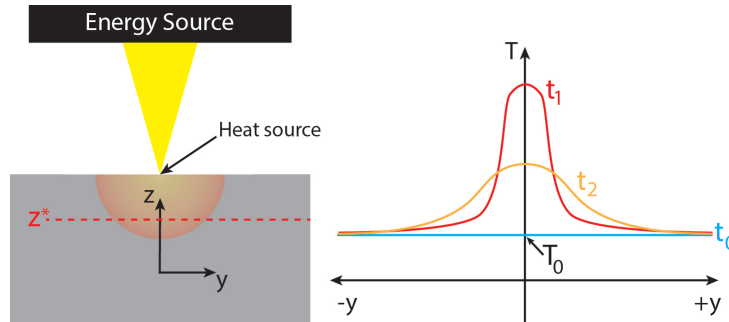

Figure 2.15: Temperature distribution from instantaneous spot weld.

Source: Adapted by author from Grong [35, figure 1.3]

Figure 2.15 shows the temperature distribution at a certain depth z^* at several points in time ($t_2 > t_1 > t_0 = 0$). As can be seen from the figure, the whole work piece holds an initial temperature T_0. A short time after the heat is applied (t_1), areas near the centerline ($y = 0$) become very hot while outer material is only marginally heated. After some more time has passed (t_2), heat near the heat source has flowed into cooler areas of the work piece and the temperature is more evenly distributed. Given sufficient time, the work piece temperature will return to T_0.

A similar setup to that shown in figure 2.15 is shown in figure 2.16. However, this figure focuses on the temperature evolution at the three points P_1, P_2 and P_3. The points are located at distances R_1, R_2 and R_3 respectively from the heat source where $R_3 > R_2 > R_1$. As the figure shows, the maximum temperature is inversely proportional to the distance from the heat source. The time necessary to reach the maximum temperature also varies. Points near the heat source reach their maximum temperature more quickly than points further away. The rate of temperature change also diminishes with distance from the heat source.

The heat source does not remain stationary in most fusion welding processes. Modelling the heat flow for an accelerating heat source can become very complex, but the heat equation can be amended fairly easily to account for a heat source moving at constant
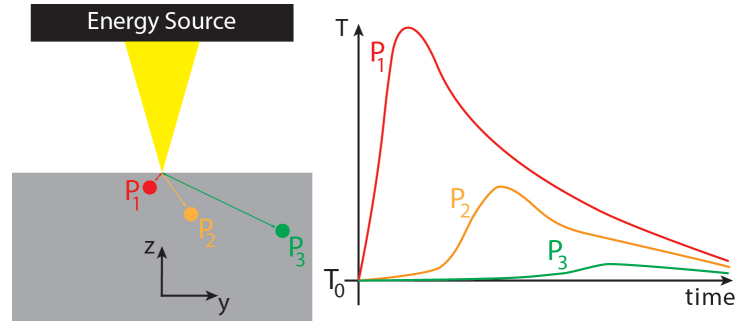
Figure 2.16: Temperature evolution from instantaneous spot weld.

Source: Adapted by author from Lancaster [33, figure 6.10]

speed along a straight line. Such a system is often referred to as a pseudo-steady state or a quasi stationary state. In such cases the net power supply from the energy source is constant which gives the weld a constant width and penetration depth. The heat equation for such a system is described by equation 2.9, where v is the constant velocity of the heat source known as the welding speed. The convention is to use a coordinate system in which the heat source moves along the x-axis. Energy is applied at a constant rate from the heat source as power P.

$$\nabla^2 T - \frac{v}{a}\frac{\partial T}{\partial t} = 0 \tag{2.9}$$

The solution to the amended heat equation is given in equation 2.10. Note that because this is a pseudo-steady state situation, there is no time variable in the solution. However, there is a variable x which denotes the distance in the x-direction from the heat source to the point in question.

$$T - T_0 = \frac{P}{2\pi\lambda r}\exp\left(\frac{-v(r-x)}{2a}\right) \tag{2.10}$$
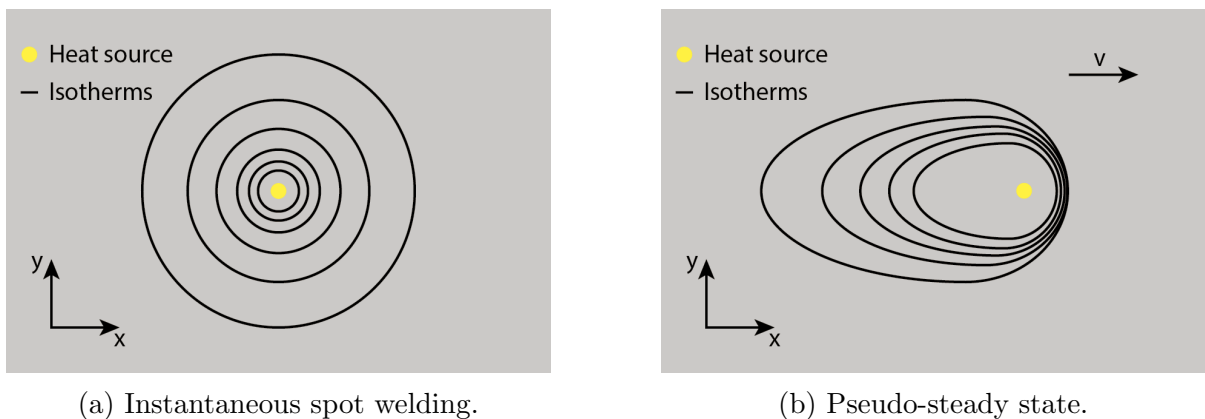
(a) Instantaneous spot welding.

(b) Pseudo-steady state.

Figure 2.17: Isotherms from heat equation.

Figure 2.17 shows isotherms for both the instantaneous and the pseudo-steady state case. For the instantaneous case (2.17a), an arbitrary time shortly after energy is applied is chosen. The important point to note is that the isotherms are circular around the heat source. In the pseudo-steady state (2.17b), the isotherms have only one plane of symmetry

(the path of the weld pass). The isotherms are compressed closely together in front of the heat source while they spread out behind it. In both the instantaneous and pseudo-steady state cases, the most important isotherm is that which corresponds to the melting temperature of the material. This isotherm will define the boundary between the weld pool and the HAZ.

$$n_3 = \frac{Pv}{4\pi a^2(H_m - H_0)} \tag{2.11}$$

The geometry of the weld pool (and the other isotherms) depends on many factors, often combined into a dimensionless operating parameter n_3 defined in equation 2.11. The denominator of this definition is determined by the physical properties of the alloy, while the numerator is determined by the process parameters power P and welding speed v. Low n_3-values are associated with elliptical weld pools, while high n_3-values change the weld pool geometry to tear-shaped (with the heat source moving away from the 'tail' of the tear).

2.5.2 Weld pool solidification

Once the fusion zone has reached its maximum size, the weld pool will quickly start to solidify. Crystals are nucleated on the liquid-solid boundary and the solidification front moves toward the heat source. Given a clean and smooth phase boundary, there will be good bonding in the weld. Each grain forms as a continuation of underlying unmelted grains, known in welding literature as epitaxial growth. As grains continue to grow, there will be competition between grains for superior orientation. However, grains in close proximity to one another will have only minor differences in orientation. This means there is no 'chill zone' of randomly oriented grains as is common in casting processes.
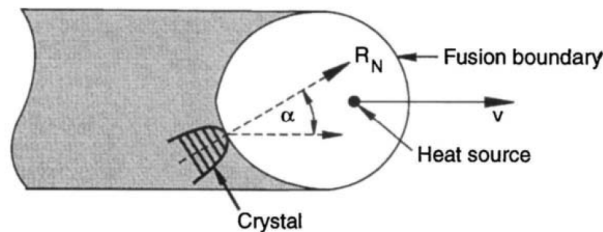

Figure 2.18: Definition of the nominal crystal growth rate.
Source: Grong [35, figure 3.12]

Figure 2.18 shows a pseudo-steady state situation. The nominal crystal growth rate R_N can be related to the welding speed v by the angle α between the grain orientation and the welding direction by equation 2.12. It is evident that the growth rate R_N is zero at the weld edge ($\alpha = 90$) and approaches the welding speed v when directly behind the heat source.

$$R_N = v\cos\alpha \tag{2.12}$$

Another important parameter is the temperature gradient at the rear of the fusion zone

boundary G. Numerically this is given by equation 2.13, where T_m is the melting point and x_1 is the distance between the heat source and the rear of the weld pool.

$$G = \frac{1}{v}\frac{\partial T}{\partial t} = \frac{T_m}{x_1} \tag{2.13}$$

The two parameters R_N and G are often combined as an important solidification parameter G/R. This new parameter in combination with nominal solute content controls the growth mode. Figure 2.19 shows which growth mode is expected for different parameters.
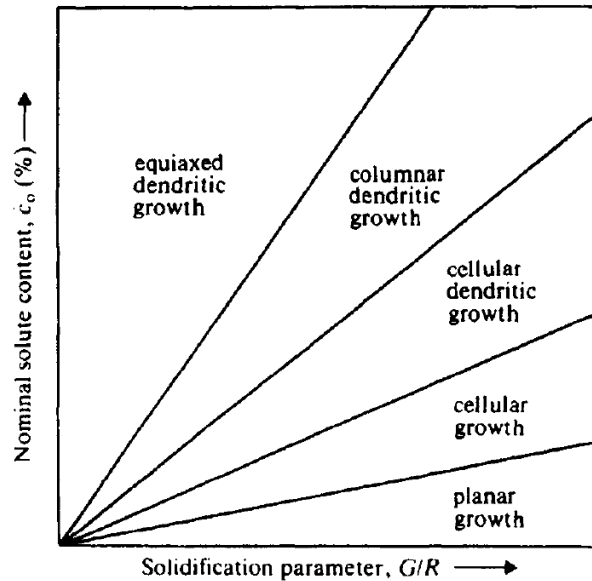

Figure 2.19: Factors controlling the growth mode during solidification.

Source: Lancaster [33, figure 7.18]

As can be seen from figure 2.19, a very high solidification parameter combined with very low solute content provides the conditions for planar growth. This is when new crystals are nucleated onto an unmelted grain and simply extend the grain into the fused zone. Increasing the solute content or decreasing the solidification parameter will encourage microsegregation and thus other growth modes. These are shown in figure 2.20.

| (a) Planar. | (b) Cellular. | (c) Cellular-dendrittic. | (d) Columnar-dendrittic. |
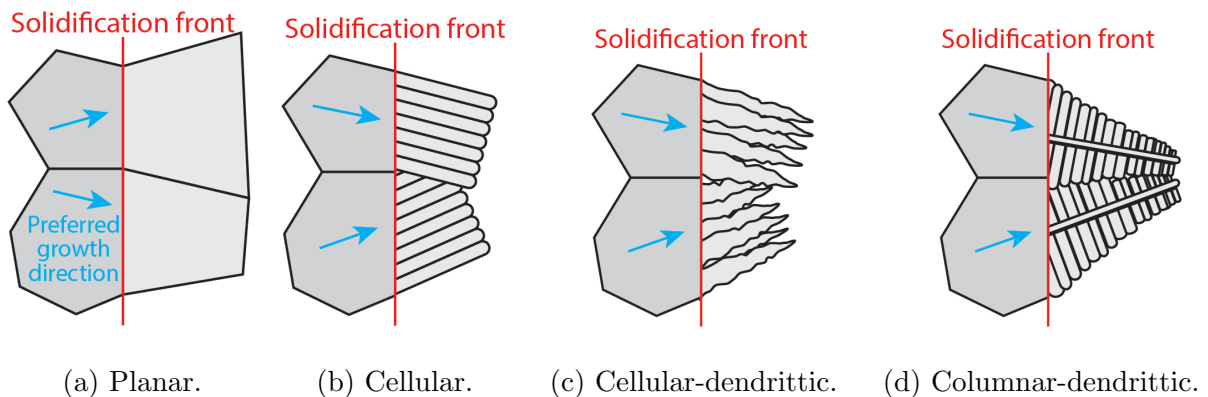
Figure 2.20: Various growth modes.

Source: Adapted by author from Lancaster [33, figure 7.19]

2.5.3   Weld defects

The welded joints are often the weakest points in structures. There are a number of features and defects that make welded aluminium parts particularly vulnerable. Despite being liquid for only a short amount of time, the weld pool can absorb and dissolve significant amounts of gases. Because the solubility of gases is much higher in the liquid state than the solid state, gas porosity can occur. The high solidification rates during welding ensure that gases are entrapped in the solid phase. Microscopic bubbles of nearly spherical geometry form as the gas pressure is the same in all directions. Figure 2.21 shows a TIG plate butt weld of 6 mm thickness with considerable gas porosity. Note the fine distribution as well as the geometry of the pores.
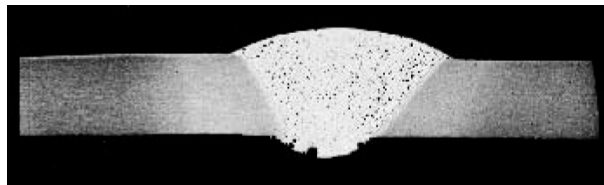
Figure 2.21: Finely distributed gas porosity in a TIG plate butt weld.

Source: Mathers [26, figure 2.7]

Oxygen gas may be entrapped in the weld pool and cause metallurgical porosity. However oxygen is more likely to react with aluminium according to equation 2.4 and form either Al_2O_3 particles or an oxide film, both considered oxide inclusions. This is detrimental to the joint because liquid aluminium does not wet oxide films (contact angle greater than $90°$). Although the oxide film may adhere well to metal with which it reacted, the bonding to metal on the other side will be poor.
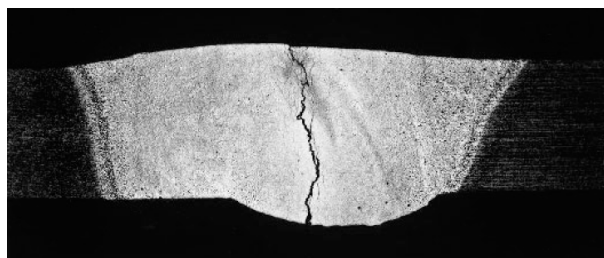

Figure 2.22: Hot cracking in a TIG plate butt weld.

Source: Mathers [26, figure 2.12]

Hot cracking is a defect caused by solidification shrinkage, most commonly found in alloys with large solidification intervals. As solid particles grow, they are enveloped by liquid. As the solidus temperature is approached, only small pockets of liquid remain. When this remaining liquid solidifies, it shrinks during the phase transformation. Because the volume of the solid is less than that of the liquid, there will be a void formed. If the liquid solidifies on several surfaces, the liquid will be 'torn' between the sides. Because this occurs at elevated temperature (the solidus temperature), the phenomenon is sometimes called 'hot tearing'. Figure 2.22 shows hot cracking in a 3mm thick AlMgSi plate TIG weld. The crack is near the centerline of the weld as this is the last material to solidify and therefore most vulnerable to hot cracking.

In addition to the volumetric change caused by the phase transformation from liquid to solid, aluminium also expands in both liquid and solid phase with increasing temperature. Volumetric changes in the liquid phase is rarely a problem because the liquid geometry will adapt to nullify internal stresses. This is not possible in the solid phase, which poses a problem. Solid shrinkage causes internal stresses as a weld cools from the solidus to room temperature. Such stresses in combination with defects such as gas pores, oxide inclusions or hot tearing may facilitate crack growth during cooling of the weld.

During fusion welding the fusion zone and HAZ are heated sufficiently to facilitate microstructural changes. This is undesirable because the resulting material is weaker than the work piece material was prior to welding. In the fusion zone, alloying elements are dissolved in the weld pool. The rapid cooling usually leaves the weld bead material as supersaturated with alloying elements. However, the HAZ is the weakest part of a welded aluminium joint. The heat facilitates grain growth which decreases the strength. For heat-treatable alloys, the problem is exacerbated because the welding is effectively a second heat treatment that overages the material as precipitate growth is facilitated.
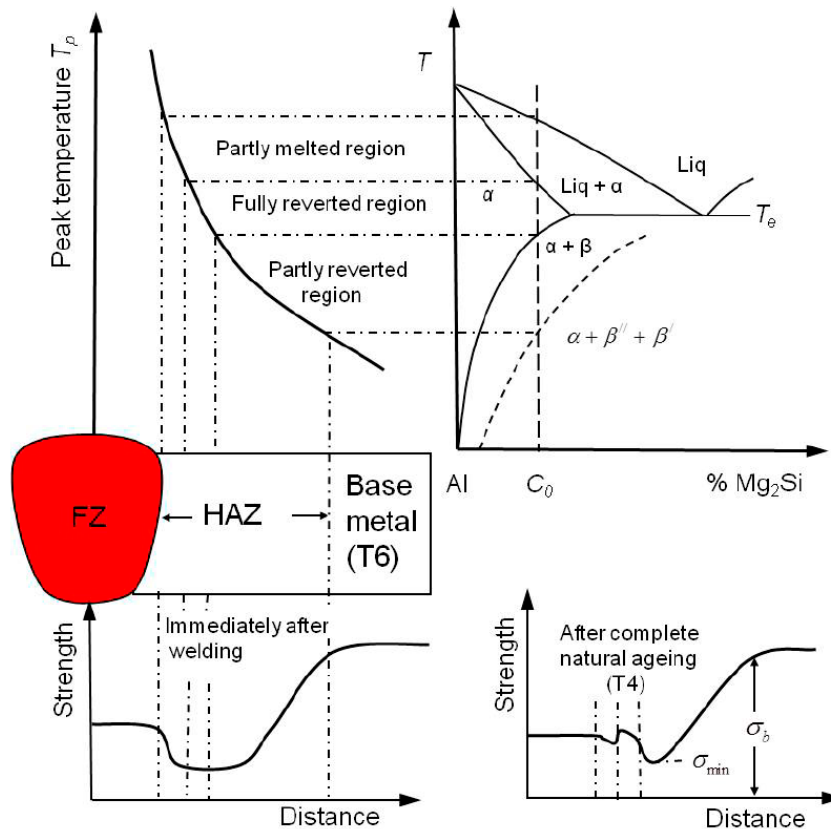
Figure 2.23: Microstructure and strength in an AlMgSi weld.

Source: Blommedal [29, figure 2.5]

Figure 2.23 illustrates the microstructure in an AlMgSi fusion weld, showing that the fusion zone contains the material with a peak temperature T_p greater than the liquidus temperature. Next to the fusion boundary are three subregions in the HAZ; the partially melted, fully reverted and partly reverted regions. The fully reverted region where the peak temperature is in the single α-phase region shows the lowest strength. Note that the highest strength is in the base metal.

## 2.6 Additive manufacturing of aluminium

Research regarding AM aluminium has surged in recent years. A breakeven analysis performed by Atzeni and Salmi [6] compared production of a component by high-pressure die casting (HPDC) and an AM SLS process. The study found that AM of aluminium may have been cost effective for low production volumes as early as 2012. Nonetheless, AM production processes have not yet been widely adopted by industry despite much interest. The industry desires good methods of assessing the quality of AM parts, both to compare various AM processes with each other as well as traditional processes. Such methods are currently under development [36].

2.6.1 Alloys and powders

Despite the recent surge of research, only a few aluminium alloys have been studied in depth. In particular, the alloy known as AlSi10Mg containing 10 wt% silicon and 0.35 wt% magnesium has received considerably more attention than any other alloy [2, 10, 11, 22, 23, 37–39]. Other studied alloys include AlSi alloys such as AlSi12 [8, 9], wrought alloys such as 6061 [8, 21] and other experimental alloys [40].

The powder is often characterized in experimental research studies. This usually involves microscopy of the powder in a scanning electron microscope SEM to evaluate the geometry and size distribution of the powder. Alternatively, laser diffraction [11] and laser granulometry [23] have been utilized to measure the size distribution more accurately. Figure 2.24 shows a typical SEM image and size distribution of a powder used for AM. The composition of the powder is often measured using X-ray spectroscopy [11] or an inductively coupled plasma (ICP) test [23].

The powder geometry is checked to ensure good flowability, which is important for deposition of powder layers. The size distribution is important for the packing factor. Powder evaluation is particularly important for recycled powders as they may have been deformed in previous production cycles. Checking recycled powder composition is also important as small amounts of impurities (especially oxygen) can be detrimental to the product's properties.
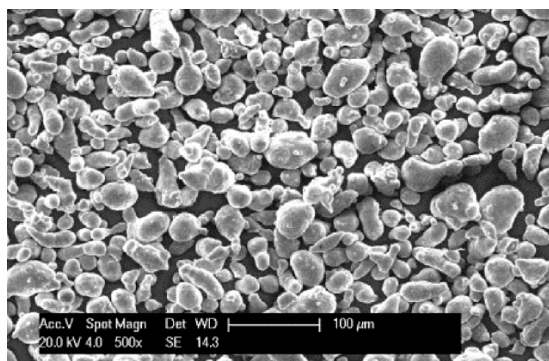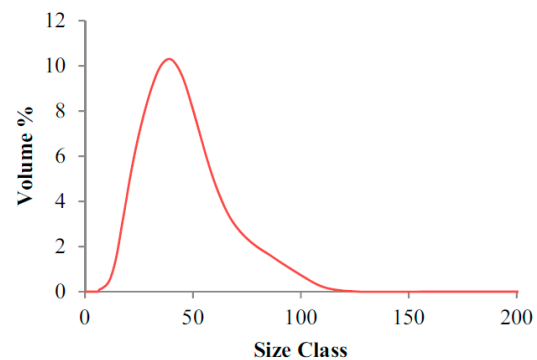
(a) SEM image.   (b) Size distribution.

Figure 2.24: AM powder characterization.

Source: Aboulkhair et al. [11, figures 2 and 3]

Parameter	Value range	Typical value
Laser power	50 - 1000 W	200 W
Scanning speed	70 - 1500 mm/s	750 mm/s
Spot size	80 - 200 μm	100 μm
Layer thickness	20 - 50 μm	50 μm
Hatching distance	50 - 300 μm	0.7 · spot size
Chamber temperature	25 - 300°C	25°C

Table 2.4: Typical values of process parameters.
Data collected from various sources [2–4, 8–12, 21–23, 37–39]

2.6.2 Product design and production

Authors of recent research articles regarding AM aluminium have taken a practical approach to the product design. Studies focusing on characterization have often made simple cubes of the material to be studied [8, 22]. Studies on mechanical properties have produced tensile test specimen directly from the PBF process as to require only minimal surface treatment before mechanical testing [9, 23, 38, 39]. A minority of studies have produced parts of complex geometries to study the effect of different designs [10].

Variations in process parameters has recently been a topic of great interest and many studies investigate their effect on the product material. The most important process parameters and typical values are given in table 2.4. The laser power used is high compared to AM of other materials, despite the low melting temperature of aluminium. The reason for this is the high reflectivity of aluminium, which according to Louvis, Fox, and Sutcliffe [8] is 91%.

Buchbinder et al. [12] state that the interaction time between the laser radiation and the powder is approximately between $4 \cdot 10^{-4}$ and $4 \cdot 10^{-3}$ seconds and the cooling rate is about $7 \cdot 10^{6}$ K/s. These values will depend on the process parameters used, but they clearly state that the process operates far from equilibrium conditions. Buchbinder et al. [12] also suggest that the process parameters can be augmented to generate different solidification conditions and therefore different product microstructures.

Argon gas is commonly used to avoid oxidation during production, although both helium and nitrogen gas have also been used successfully. The gas is circulated through a filtering system to remove fine metallic particles produced during production. Also note that the building chamber is never completely free of oxygen. Instead, the oxygen level is reduced to a level of about 0.1-0.3%. Due to the reactivity of aluminium powders, the loading and unloading of powders into the machine must be done with care. The operator should wear protective work clothing, gloves, tight-fitting goggles and a respiratory mask when handling aluminium powders [41]. In addition, antistatic protective equipment is advisable as only a very small electrostatic discharge is required to ignite a dust/air mixture. Such dust is created during the PBF process from evaporation of melt pools. Therefore these health and safety (HSE) precautions must be followed both during loading and unloading of powders and parts.

After process completion, the product is removed from the machine. This involves recycling unmelted powder around the part. The majority of the powder can be removed using a spade followed by final removal using a special vacuum cleaner (using an inert

gas). For productions at elevated temperature, some unmelted powder may have been slightly sintered, limiting the recyclability of the powders. A consequence of the PBF process is that the part is fused with the fabrication platform. Generally a few layers of hollowed material (support structure) are added below the part at the pre-build stage to level the fabrication platform as well as to make removal easier. The part is often separated from the fabrication platform by electrical discharge machining (EDM).

A post processing heat treatment often used for AlSi10Mg alloys is to anneal the part at 300°C for two hours [2, 10, 23]. This is commonly referred to as a 'stress relief heat treatment' meant to relieve the product of residual stresses from the production process. The heat treatment can be conducted before or after the part has been removed from the fabrication platform.

2.6.3 Porosity

An important parameter to describe quality of AM products is density. If a material contains no porosity, it is said to be 'fully dense', but all AM products contain some porosity as a result of the production process. Therefore the parameter 'relative density' has become useful to describe the quality of a product (see equation 2.14). The relative density is usually expressed as a percentage.

$$\text{Relative density} = \frac{\text{Density of product material}}{\text{Density of fully dense reference material}} \tag{2.14}$$

Several methods of determining the relative density of AM materials have been developed and compared by Spierings, Schneider, and Eggenberger [36]. The most common is the Archimedes method (submerging the product in a fluid). This non-destructive testing (NDT) method provides an accurate density value. It is however limited to only measure the density. Microscopy of cross-sections is often used to investigate the porosity in greater detail.

Porosity in AM aluminium has been studied in several papers [8, 11, 12, 22, 23, 37, 38]. Both the relative density of the produced material and the characteristics of the porosity are strongly correlated with the process parameters used during production. AlSi10Mg products have been produced with relative densities in the range of 94.3-99.8 % depending
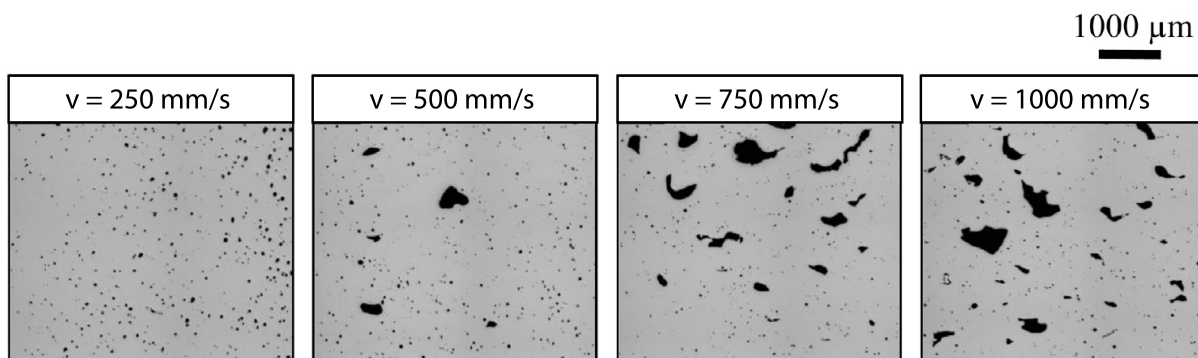
Figure 2.25: Metallurgical and keyhole pores at various scanning speeds.

Source: Aboulkhair et al. [11, figure 5]
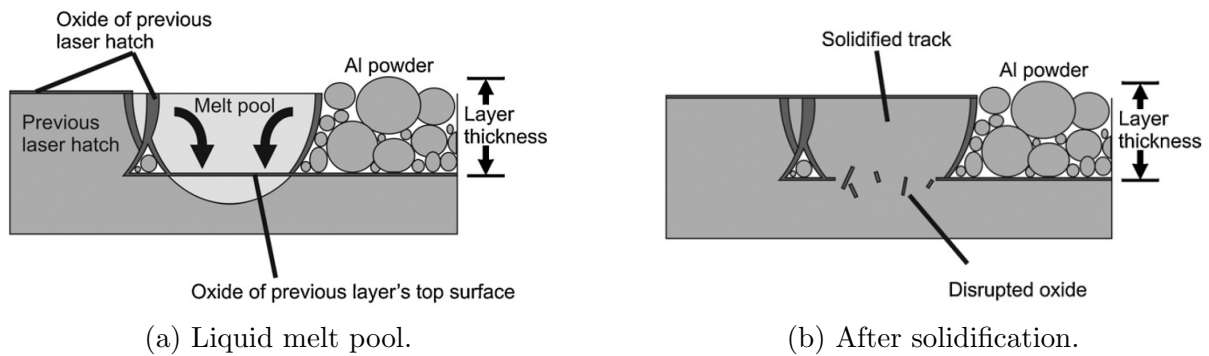
(a) Liquid melt pool.

(b) After solidification.

Figure 2.26: Formation of oxide pores.

Source: Louvis, Fox, and Sutcliffe [8, figure 19]

on the process parameters. The laser power, scanning speed and scanning strategy appear to be particularly influential. An AlMgSi wrought alloy of 6061 specification [13] was produced at realtive densities of 80-89 % [8].

The porosity found in AM aluminium alloys consists of different types that closely resemble defects of fusion welding. Aboulkhair et al. [11] describes metallurgical pores and keyhole pores. Metallurgical pores are small, evenly distributed spherical pores that resemble gas porosity in fusion welding. Keyhole pores are uneven pores attributed to rapid solidification of the liquid without complete filling of gaps (similar to hot cracking). Aboulkhair et al. [11] found that metallurgical pores are more prevalent for low scanning speeds, while keyhole pores become dominant at higher scanning speeds (see figure 2.25).

Louvis, Fox, and Sutcliffe [8] argue that some pores arise due to oxide films formed during production. Such oxide films can form at oxygen levels far below the usual 0.1-0.3% at elevated temperature, and the wetting angle of liquid aluminium on an oxide film is very high. As a result, the liquid will neither produce good bonding with the substrate nor flow freely when oxides are present. Such pores may share many similarities with oxide inclusions in fusion welding. Figure 2.26 shows a principle sketch of this type of pore forming. This hypothesis is supported by recent findings of large and irregular pores that clearly contain unmelted powder particles (see figure 2.27).
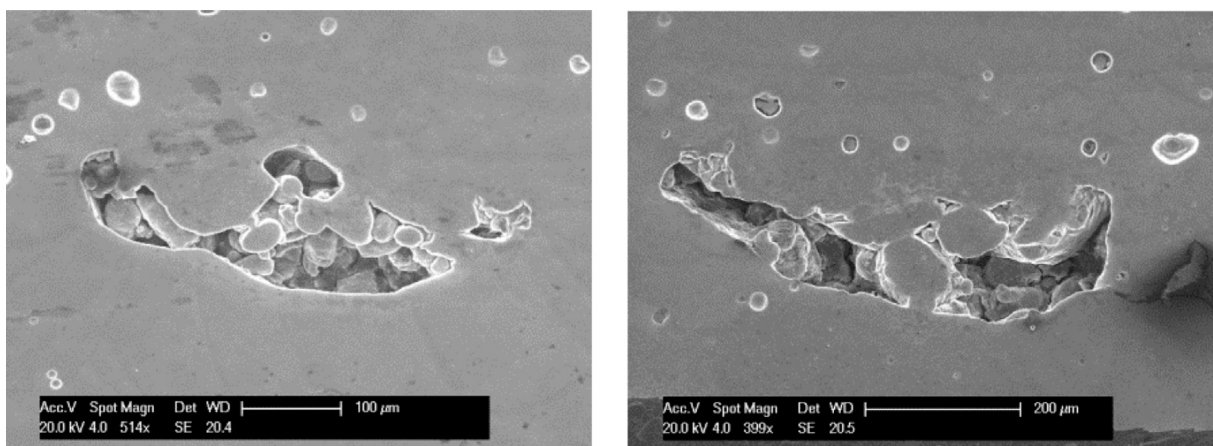
Figure 2.27: Oxide pores containing unmelted powder.

Source: Aboulkhair et al. [11, figure 10]

Size	Features
$> 100~\mu$m	Oxide pores and keyhole pores
$\sim 250~\mu$m	Melt pools
$< 50~\mu$m	Metallurgical pores
$\sim 10~\mu$m	Melt pool contours
$< 0.5~\mu$m	Grain structure of material and microsegregations

Table 2.5: Typical size of features material structure in AM aluminium.

Data collected from various sources [11, 12, 22, 23, 37, 38]

2.6.4 Material structure

The many features of AM aluminium are of different size scales as shown in table 2.5. At the largest scale, oxide and keyhole porosity dominate (see figure 2.25). Features more directly related to the PBF process are found on a smaller scale. A 'melt pool' refers to the molten material during the process, similar to a weld pool in fusion welding. Each melt pool is similar to a weld pass, but while weld passes constitute only a small a part of a welded structure, the weld pools make up the entire AM part. A schematic diagram of the generation of melt pools and relevant terminology is shown in figure 2.28.
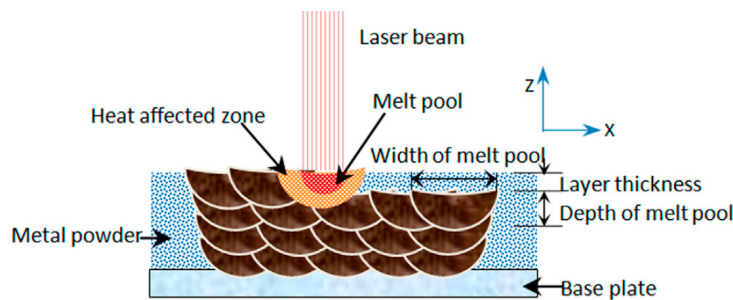
Figure 2.28: Generation of melt pools in PBF processes.

Source: Yan et al. [10, figure 4]

Traces of the fusion boundaries of melt pools found in the solidified material are called 'scan tracks'. Cross-section specimens must be prepared to observe the scan tracks, usually in two orientations in the material. The first is a plane parallel to the fabrication plane (the xy-plane) looking 'down' at a layer from above. The second orientation is usually perpendicular to the first, viewing the layers horizontally (xz-plane). Two such planes are recorded by Yan et al. [10] using an optical microscope (OM), as shown in figure 2.29. Specimens for such analyses require significant preparation for adequate results. Polished surfaces can be used to evaluate porosity, but due to the high reflectivity of aluminium there is poor contrast between grains. Specimen are therefore often etched to increase contrast when studying scan tracks and microstructure. The most commonly used etchants are Keller's reagent [42] and Weck's reagent [43].

Optical micrographs of scan tracks have revealed that the penetration depth of the melt pools is many times greater than the layer thickness, meaning each point in the AM material is melted several times. The lines of the scan tracks as sometimes called 'melt pool contours' as they represent the fusion boundary of the melt pools. Figure 2.31 shows the cellular microstructure of an AlSi10Mg alloy, revealing that it is coarse at the
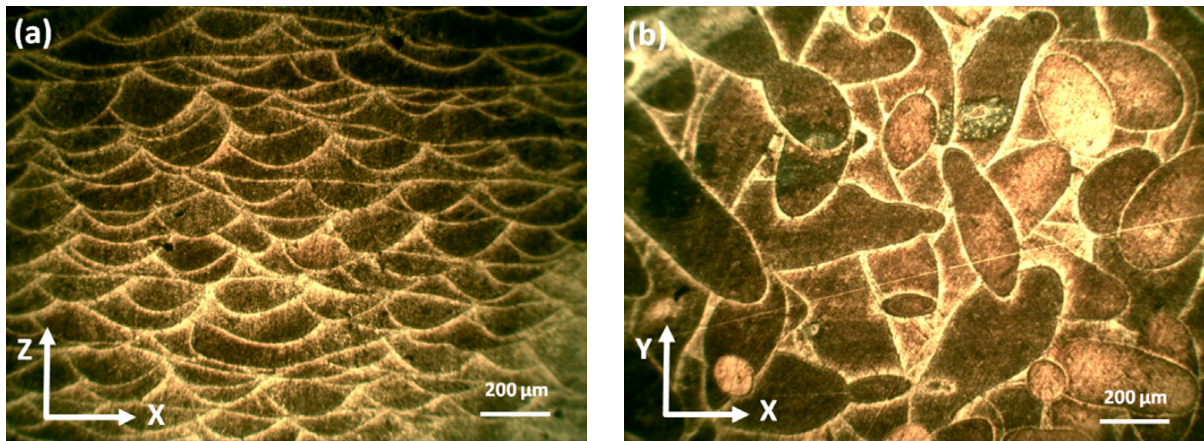
(a) Side view. (b) Above view.

Figure 2.29: Scan tracks of an AlSi10Mg part.

Source: Yan et al. [10, figure 3]

boundary compared to the inner melt pool. This same result has been found in other studies on AM aluminium [11, 23, 37], as well as on laser deposited aluminium [44].

The features at the very smallest scale are microsegregations in the structure. By using an energy-dispersive spectroscopy (EDS)-equipped transmission electron microscope (TEM), these can be mapped. Figure 2.30 shows such a mapping of an AlSi10Mg part, showing how aluminium constitutes the bulk of the cells while silicon has precipitated to the boundaries. Magnesium remains fairly evenly distributed, but slightly more concentrated with silicon on the boundaries.
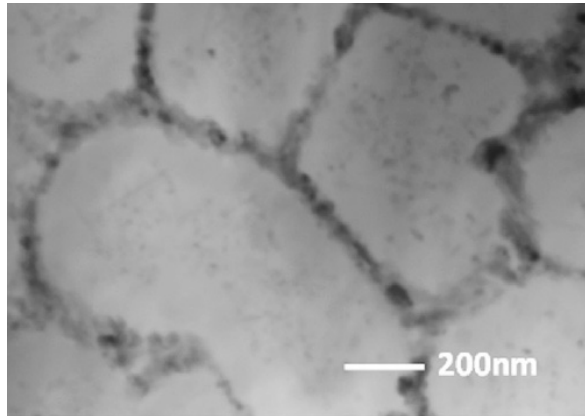
(a) Bright field image.
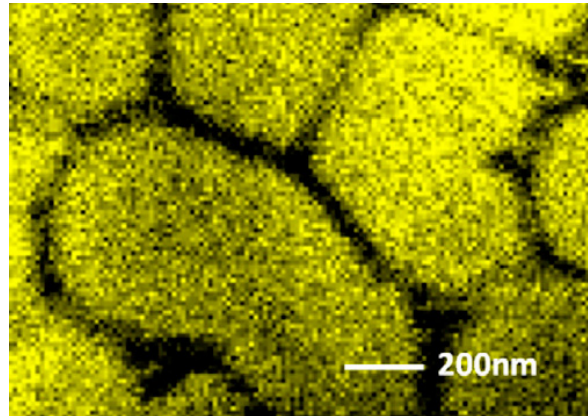
(b) EDS map of aluminium.
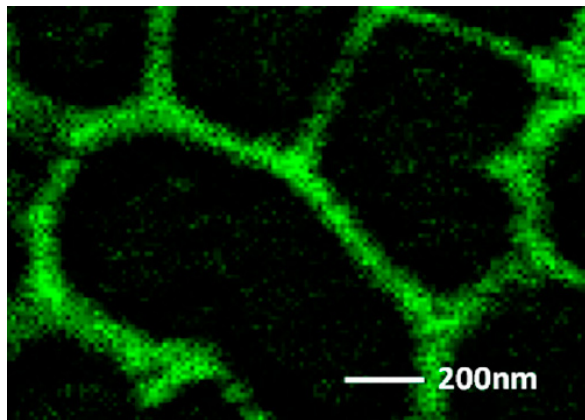
(c) EDS map of silicon.
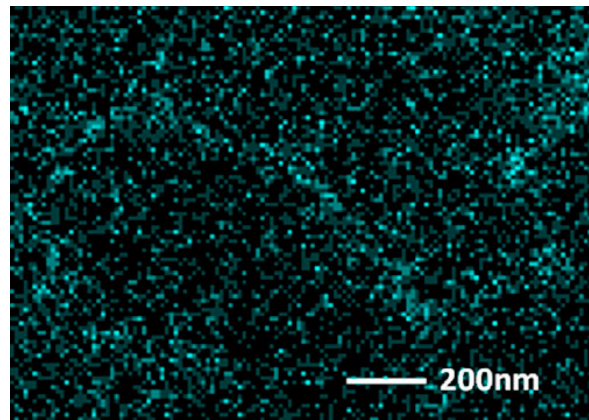
(d) EDS map of magnesium.

Figure 2.30: TEM-EDS analysis of AlSi10Mg AM material.

Source: Yan et al. [10, figure 7]
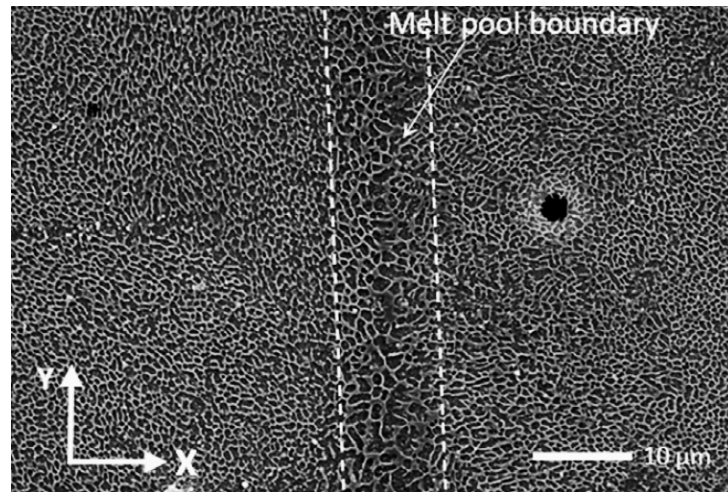
(a) Overview.
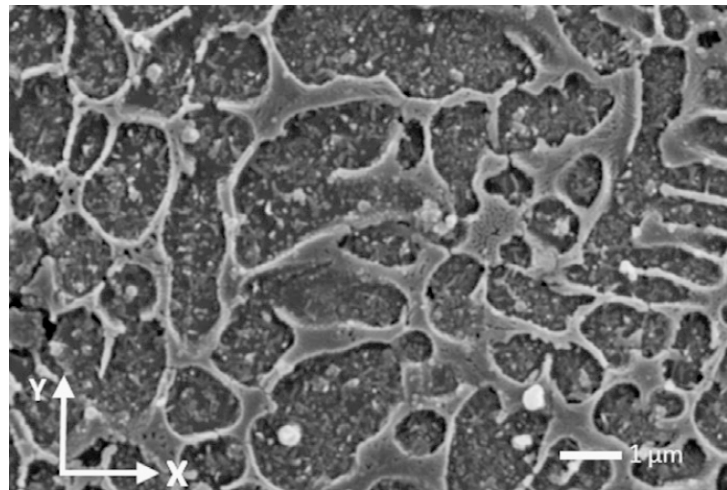
(b) Melt pool contour.
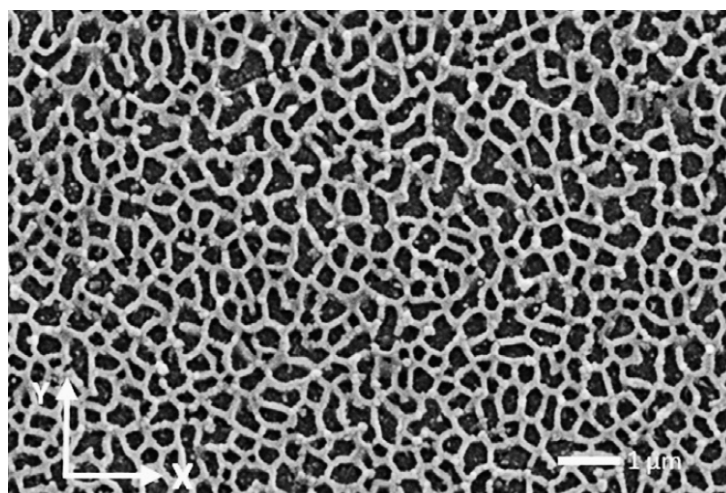
(c) Inner melt pool.

Figure 2.31: Microstructure of an AlSi10Mg part.

Source: Yan et al. [10, figure 5]

Alloy	Si	Mg	Fe	Mn	Cu	Zn	Ti	Reference
AlSi10Mg	9-11	0.2-0.45	0-0.55	0-0.45	0-0.10	0-0.10	0-0.15	[45]
AlSi10Mg	9.5	0.33	0.15	0.01	0.001	0.002	0.004	[2]
AlSi10Mg	10.08	0.35	0.16	0.002	0.001	0.002	0.01	[23]
356.0	6.5-7.5	0.2-0.45	0.6	0.35	0.25	0.35	0.25	[46]
357.0	6.5-7.5	0.45-0.6	0.15	0.03	0.05	0.05	0.20	[46]
359.0	8.5-9.5	0.5-0.7	0.20	0.10	0.20	0.10	0.20	[46]

Table 2.6: Chemical compositions of AlSi10Mg and similar alloys.

2.6.5 Mechanical properties

The mechanical properties of AM aluminium has been investigated in detail recently. However, such invesigations have been limited to AlSi alloys, with AlSi10Mg receiving the bulk of the attention.

The AlSi10Mg alloy is specifically designed for AM and does not satisfy any standard designation. However, there are several AlSi casting alloys of similar composition, as shown in table 2.6. An overview of the mechanical properties of AlSi10Mg and similar alloys is given in table 2.7. Note that there are two tempers for AlSi10Mg; 'AM-F' refers to materials with no post processing heat treatment, while 'AM-O' refers to specimens that underwent stress relief heat treatment (300°C for two hours).

The data in table 2.7 shows that the ultimate tensile strength (σ_{UTS}) and elongation are high for AM AlSi10Mg relative to comparable casting alloys. This suggests that the unique microstructure that arises from the PBF process can strengthen AM materials in a way that traditional manufacturing cannot. Nonetheless, the yield strength (σ_y) and Young's modulus (E) are quite similar to comparable casting alloys. The data also shows that AM materials are anisotropic, particularly after stress-relief heat treatment when the strength in the building direction (z-direction) is considerably lower than in the building plane (the xy-plane).

Alloy	Temper	σ_y [MPa]		σ_{UTS} [MPa]		E [GPa]		Elongation [%]		Reference
		z	xy	z	xy	z	xy	z	xy	
AlSi10Mg	AM-F	-	-	396	391	68	68	3.5	5.6	[39]
AlSi10Mg	AM-O	172	227	289	358	75.4	65.5	2.6	3.9	[2]
AlSi10Mg	AM-O	231	243	329	330	72	72	4.1	6.2	[23]
356.0	F	70	-	145	-	-	-	3	-	[46]
356.0	T6	160	-	230	-	72.4	-	3	-	[46]
356.0	T7	-	-	170	-	-	-	3	-	[46]
357.0	T6	230	-	295	-	-	-	3	-	[46]
359.0	T6	205	-	275	-	-	-	3	-	[46]

Table 2.7: Mechanical properties of AlSi10Mg and similar alloys.
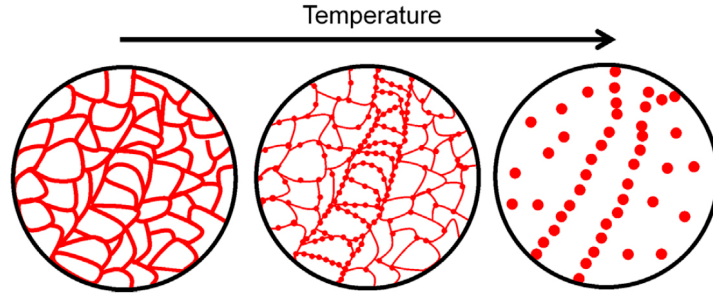
Figure 2.32: Microstructure evolution during annealing.
Source: Prashanth et al. [9, figure 9]

2.6.6 Other research areas

Recent research on AM aluminium has studied the process from various perspectives. Several studies have investigated the effect of process parameters [2, 8, 11, 22, 37]. It is clear that using suitable process parameters is absolutely necessary to produce a material without excessive porosity. Prashanth et al. [9] have studied the effect of post processing heat treatments on the microstructure of the material, finding that the cellular structure can be changed to a particulate structure (see figure 2.32).

The process parameters are important for the productivity of AM as well as the material properties. Buchbinder et al. [12] studied how to increase the build rate $\dot{V}$, or volume of material produced per unit time. It was assumed that 80% of the production time is spent scanning each layer while the remaining 20% was allocated to depositing new power layers. Therefore the build rate can be approximated by equation 2.15.

$$\dot{V} = \Delta z_{\text{layer}} \cdot v \cdot \Delta y_h \tag{2.15}$$

where Δz_{layer} is the layer thickness, v is the scanning speed and Δy_h is the hatching distance. The goal is to maximize the build rate while retaining excellent material properties. If the layer thickness and hatching distance are to remain small for good resolution, the scanning speed and laser power have to be increased for higher build rate. However, increasing these parameters make the melt pool unstable and can cause difficulties similar to spattering encountered during welding. Nonetheless, increasing the build rate is a presumed requirement for wide adoption of AM [1, 5, 6].
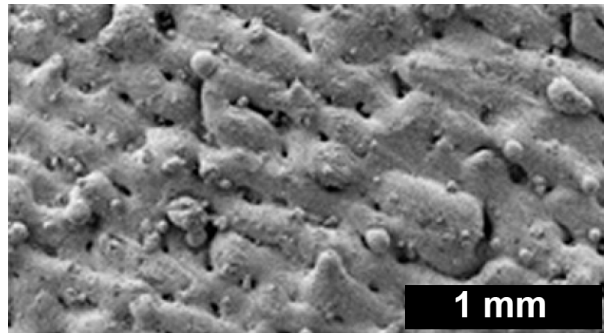
Figure 2.33: SEM micrograph of an AlSi10Mg part's surface.
Source: Atzeni et al. [47, figure 5(d)]
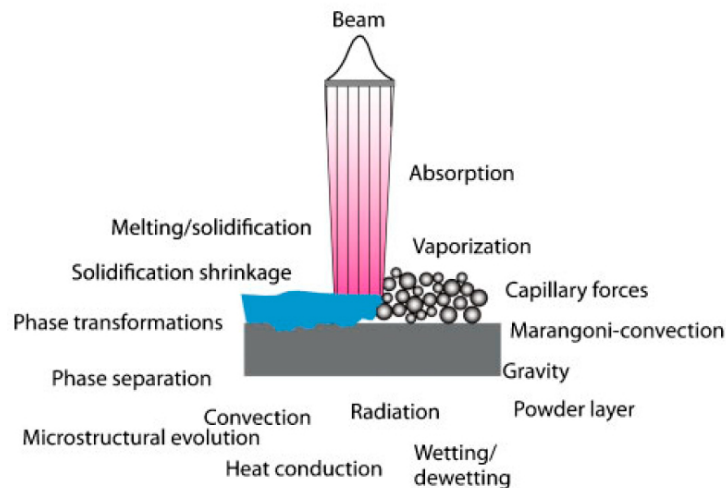
Figure 2.34: Physical phenomena happening during PBF processes.

Source: King et al. [48, figure 2]

One of the benefits of AM is the ability to produce complex geometries. Such geometries often make surface treatment impractical if not impossible. However, PBF processes produce rough surfaces (see figure 2.33). This is a consequence of the resolution being limited by the penetration depth, layer thickness, spot size and hatch distance. Surface layers are not remelted in the same way that bulk materials are, and the surface roughness will depend on the orientation of the surface relative to the building direction. The surface material is therefore increasingly being investigated and new surface treatment methods are being developed [47].

Development of computer models has been an important part of AM research [21, 48, 49]. The models try to simulate the PBF process to accurately predict the effect of varying process parameters or even predict the final material properties. For such models to be accurate, they must incorporate a large number of physical phenomena (see figure 2.34). Models are continuously improved, but they remain too limited for practical application.

3   Experimental

3.1   Raw material powders

Powders of two different aluminium alloys were used for experimental work in this thesis. The first was a product of the German company ConceptLaser GmbH named CL 31AL. It is an AlSi10Mg alloy designed to be used for PBF and will henceforth be called 'AlSi10Mg' in this thesis. The second powder was the product LPW 6061 made by the British company LPW Technology Ltd. This powder, designed for PBF or laser metal deposition applications, is of 6061 specification [13, 50], and will henceforth be called 'AA6061'. Both powders were produced by gas atomization.

The chemical composition of the powders is given in table 3.1 (all values in wt%). For AlSi10Mg, only the composition range was given [45]. The supplier conducted a chemical analysis of the AA6061 powder for a precise composition. This, along with the standard specification for 6061 are given in the table.

	AlSi10Mg	AA6061	
Element	Specification	Specification	Analysis
Al	Balance	Balance	Balance
Mg	0.20 - 0.45	0.8 - 1.2	1.00
Si	9.0 - 11.0	0.4 - 0.8	0.65
Fe	0 - 0.55	0 - 0.70	0.07
Cu	0 - 0.10	0.15 - 0.40	0.22
Cr	-	0.04 - 0.35	0.26
Mn	0 - 0.45	0 - 0.15	0.10
Ti	0 - 0.15	0 - 0.15	< 0.01
Zn	0 - 0.10	0 - 0.25	0.01
C	0 - 0.05	-	-
Ni	0 - 0.05	-	-
Pb	0 - 0.05	-	-
Sn	0 - 0.05	-	-
Other	-	0 - 0.15	< 0.15

Table 3.1: Given compositions of AlSi10Mg and AA6061 powders.

The size range for the powders AlSi10Mg and AA6061 were 25-53 μm and 20-63 μm respectively. The AlSi10Mg powder was provided by the Department of Production and Quality Engineering (IPK) at the Norwegian University of Science and Technology (NTNU) where it had been stored for two years. The AA6061 powder was received from the supplier on November 30th 2015.

3.2 Production of components

3.2.1 Component design

One of the objectives of this thesis was to design a component suitable for material characterization of AM parts. The design is shown in figure 3.1 consisting of a massive 'base' with extended cylinders (see figure 3.1a). The design was created based on three criteria:

1. **Material characterization:**
   The base is massive and can be cut into various cross-sections and studied using traditional metallographic techniques. The cylinders may be removed and machined into mechanical test specimen to evaluate mechanical properties, including anisotropy as the cylinders extend in different directions.

2. **Symmetry:**
   The symmetry of the design allows each test specimen to be duplicated. This may be useful to reproduce results, compare two different treatments or to have an extra specimen in case of unintended damage.

3. **Demonstration model:**
   The inspiration of the component design was a generic juncture in a structural application, such as a bridge construction. The uncut part can be used to present features of the PBF process such as surface roughness and spacial resolution.

The component was designed by the author using Autodesk AutoCAD software [51]. The base was created using simple 2D geometric shapes as shown in figure 3.1a, then extruded 15 units. Finally, cylinders were extruded from the surfaces to create the final 3D design shown in figure 3.1b. The cylinders are oriented at angles of 45° relative to one another. The total volume of the model is 42 840 units cubed, while the model can be contained within a box of dimensions 115x15x55 units.
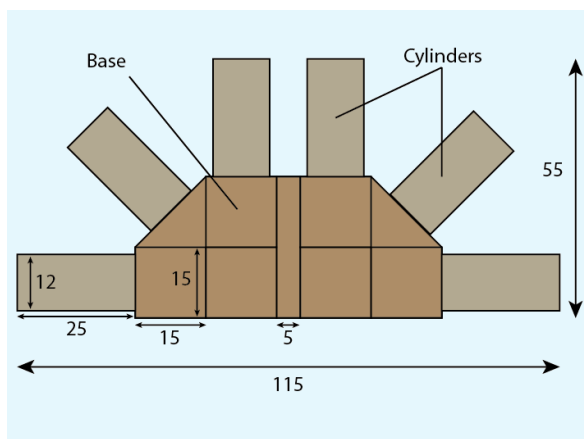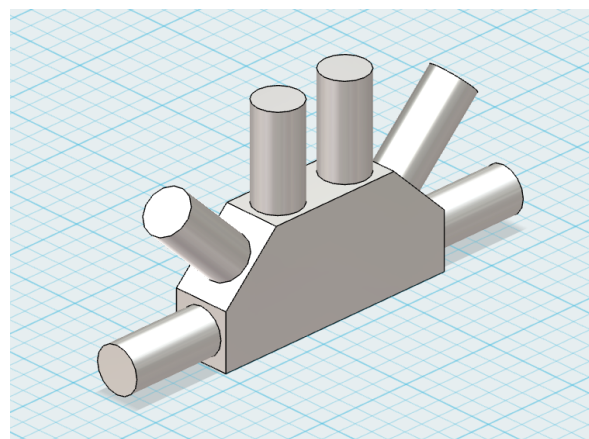
<table>
<tr><td align="center">(a) 2D design.</td><td align="center">(b) 3D design.</td></tr>
</table>

Figure 3.1: CAD model of component.

Parameter	Symbol	Value
Laser Power	P	200 W
Scanning speed	v	800 mm/s
Spot size	d_{spot}	150 μm
Layer thickness	Δz_{layer}	30 μm
Hatching Distance	Δy_h	105 μm
Fabrication chamber temperature	T_{FC}	25°C
Shielding gas	-	Nitrogen

Table 3.2: Process parameters for production of components.

3.2.2 Pre-build modifications and fitting

The scale for the physical model was set to 1 unit = 1 mm and the orientation set so the fabrication platform is the grid shown in figure 3.1b. In this way three pairs of cylinders have length directions oriented at 0°, 45° and 90° angles relative to the building direction. This orientation also minimized the required support structure, which consisted of 2 mm hollowed material as measured from the bottom of the base.

3.2.3 Build

One component of each material was produced by an M2 Cusing machine supplied by ConceptLaser GmbH and equipped with a 200 watt Ytterbium fiber laser. The production took place at the facilities of IPK. The process parameters used for both components can be found in table 3.2.

The hatching distance was set to 70% of the spot size, which was defined as the diameter within which 99% of the laser effect was concentrated. Production occurred at room temperature and nitrogen was used as the shielding gas. The fabrication platform was made of aluminium alloy 6082. Figure 3.2 illustrates the scanning strategy used, implementing islands that were both rotated and shifted between layers. The same process parameters were used for all modes (contour, fill, up-skin and down-skin). The total production time for each component was just under 16 hours, half of which was time spent fusing powders.
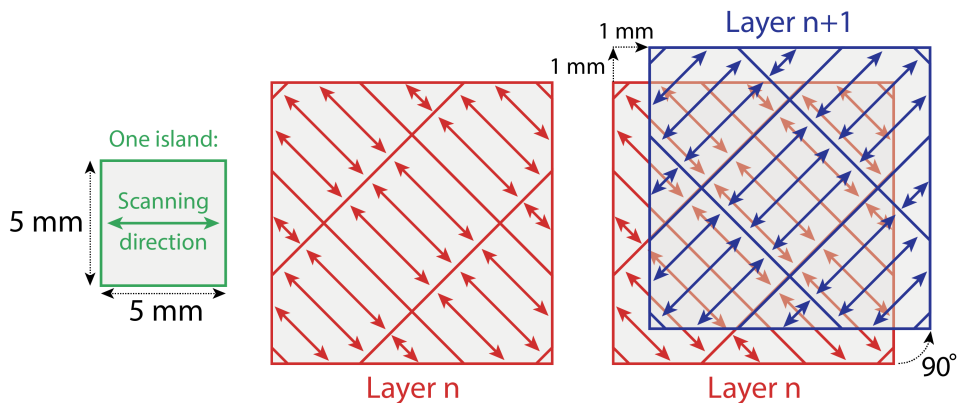
Figure 3.2: Scanning strategy for production.

3.2.4 Post processing

The parts were removed from the fabrication platform using a hammer and chisel. Each model was then cut into smaller bits to prepare for characterization. Initially only half the piece was cut, so the other half could be used as a demonstration model. The cutting lines and bit labels are shown in figure 3.3. The cylinders were cut off and labelled C_0, C_{45} and C_{90}, where the subscript refers to the angle between the building direction and the length direction of the cylinder. These were to be machined into compression test specimens to evaluate the flow stress of the material (the stress to which the stress-strain relationship converges to at large compressive strains, σ_{fl}).

The bits of the bulk were cut to show a particular surface of interest. The B_{above} bit would be further cut horizontally into thin plates showing the fabrication surface (the xy-plane). When viewed in the microscope, this view will be called the 'above view'. Likewise, the B_{side} bit would be cut vertically to show the yz-plane. This view, called the 'side view', presents the layers horizontally. The B_{45} and B_{bulk} bits would serve as extra material if required. Finally the B_{rest} bit would serve as a demonstration model. The cutting of these bits was done in the workshop of the technical section at the Faculty of Natural Sciences and Technology at NTNU.
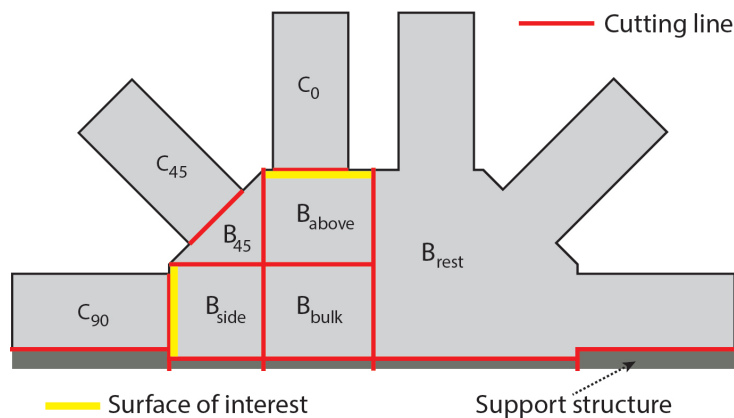
Figure 3.3: Initial cuts of the components.

3.3 Characterization of powders

In an attempt to understand the material more fully, samples of the raw powder materials were characterized. About 50 mL of sample powder of each material was moved to sealed containers using a glove box filled with nitrogen gas at IPK. Thus each of the containers were filled with nitrogen gas in addition to the powder. This procedure was done to avoid excessive oxidation of the powders, which would both decrease the value of powder analyses as well as pose safety risk because the explosivity of the powders was unknown.

3.3.1 Sample preparation

Each powder was cast in epoxy to make samples for optical microscopy. A two-part epoxy called Epofix [52] with a curing time of 8 hours was used. To avoid oxidation as well as
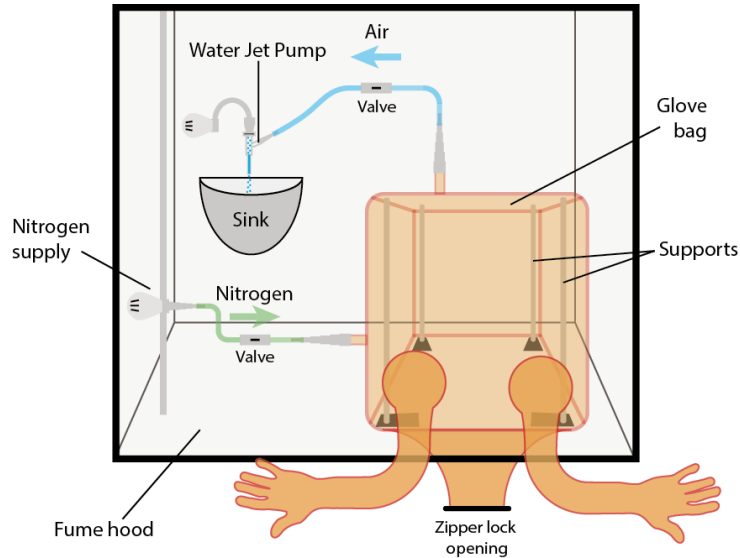
Figure 3.4: Glove bag setup.

health risks, the casting process was completed in a glove bag provided by Sigma-Aldrich [53]. The glove bag was placed in a fume hood and connected to a supply of nitrogen gas. A water jet pump was used to evacuate the bag. Two plastic ball valves were connected in series to the gas lines, allowing the system to be closed. The setup is shown in figure 3.4.

Plastic casting forms of 30 mm diameter were used to cast the powders. For practical reasons the resin and hardener parts were weighed outside the glovebag. 75 grams of resin and 9 grams of hardener were needed to fill four casting forms. The unmixed parts along with the sealed container of powder were placed in the glovebag. Then the air was evacuated by the water jet pump and the bag was filled with nitrogen gas. Variations of the casting in each form is described in table 3.3. The wetting ability of the mixed epoxy on the powder was unknown, so a thin layer of epoxy was first placed in the form's bottom. Then powder was added before the forms were filled with more epoxy. This was done to be certain that the powder was surrounded by epoxy on all sides. Roughly 1 mL of powder was added to forms 1 and 2 (the 'small' amount of powder), while about 3 mL was added to forms 3 and 4 (the 'large' amount).

The castings were allowed to harden in the nitrogen-filled glove bag for 12 hours before the samples were removed from the forms. After casting the samples were sanded to reveal particles on a flat surface. Waterproof SiC grinding papers were used with increasing grit in the following sequence; P500, P800, P1200, P2400 and finally P4000. After grinding, the samples were polished using 3 μm and then 1 μm polishing disks. The samples were rinsed in soap water and ethanol between each polishing step. Final polishing was done using OP-S standard colloidal silica suspension of size 0.04 μm [54]. The samples were then rinsed in an ultrasound bath of water to remove any silica particles.

	Non-stirred	Stirred
Small amount of powder	Form 1	Form 2
Large amount of powder	Form 3	Form 4

Table 3.3: Variations in castings of OM samples.
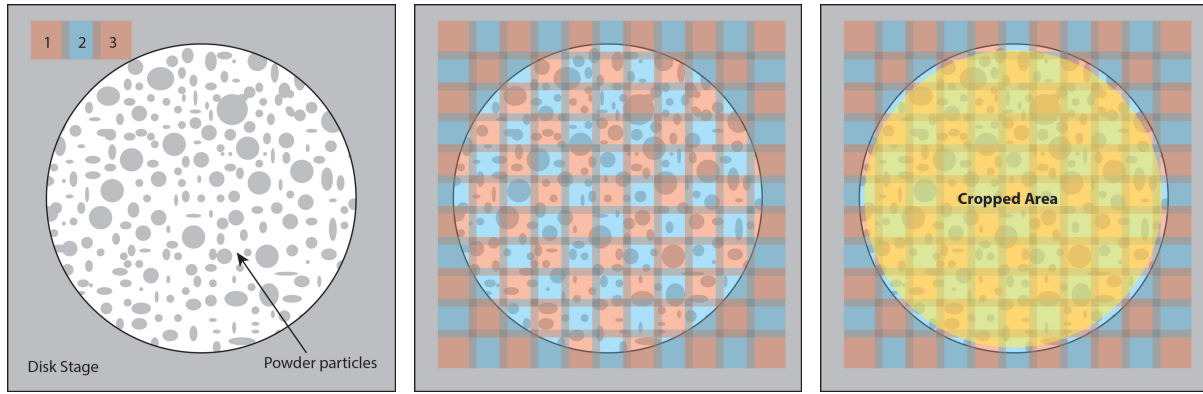
| (a) First three images. | (b) Completed raster. | (c) Cropped area. |

Figure 3.5: Sequence of overlapping micrographs of cast powder samples.

3.3.2 Optical microscopy

The sample with the best polished finish of each powder was selected for microscopy. Micrographs were recorded using a Leica MeF4 optical microscope equipped with a Jenoptik Laser Optik System camera of type ProgRes C10 plus. The samples were placed onto a disk stage with an orifice smaller than the sample surface to avoid noise. No filters were utilized and the aperture was kept open to maximize the resolution. An objective lens of 5X magnification was used along with an ocular lens of 10X magnification for a total magnification of 50X.

A raster of overlapping images were recorded as shown in figure 3.5. The first image taken was in the upper left corner. Then the stage was moved to the right a distance roughly 70% of the first image's width where a second image was recorded. This procedure was continued to the other edge, when a second row of images was begun. The final raster is shown in figure 3.5b. All the images of each sample were then imported into Adobe Photoshop CC [55] image manipulation software and stitched together using the 'Photomerge' function, producing a single image of high resolution. The contrast was then adjusted before the image was cropped to an area inside the orifice of the disk stage (see figure 3.5c). In addition, higher magnification images were recorded separately with various objective lenses to examine details in the samples.

The cropped images were imported into the image analysis software program ImageJ [56]. A suitable threshold was set to accurately depict each particle, before converting to a binary image (black particles on a white background). The following measurements were then recorded for each particle; area A, maximum feret distance $d_{\max}$, minimum feret distance $d_{\min}$ and perimeter length P.

For each particle the average diameter $\bar{d}_{\mathrm{powder}}$ was computed by equation 3.1. The factor $\frac{4}{\pi}$ is to compensate for the fact that the polished surface is a random cross-section of each powder particle. The average diameter of a random cross-section is $\frac{\pi}{4}$ times the diameter of the sphere. Therefore the average diameter calculated from the ImageJ analysis data must be multiplied by the multiplicative inverse $\left(\frac{4}{\pi}\right)$.

$$\bar{d}_p = \frac{4}{\pi} \cdot \frac{1}{3}\left(d_{\max} + d_{\min} + \sqrt{\frac{4A}{\pi}}\right) \tag{3.1}$$
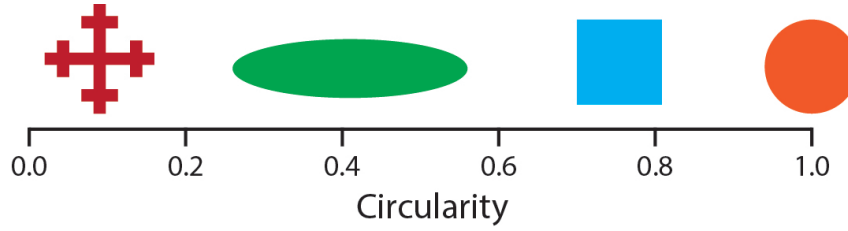
Figure 3.6: Circularity of various geometries.

To evaluate the geometry of the particles, the circularity parameter C was calculated for each particle according to equation 3.2. The circularity of a circle is 1, which is the minimum perimeter to contain the area. Other geometries have larger perimeters and therefore a smaller circularity. The circularity is zero for an infinitely long line as the perimeter is infinite. The circularity of various geometries is shown in figure 3.6.

$$C = 4\pi \frac{A}{P^2} \tag{3.2}$$

3.3.3 Scanning electron microscopy

A small sample of powder was transferred from the sealed powder container onto a sheet of aluminium foil. The foil was then disrupted to spread the sample powder to a fine layer. From this layer a small amount of sample was transferred onto copper tape and mounted onto the sample holder.

Parameter	Value
Accelerating Voltage	15 kV
Working distance	10 mm
Aperture radius	30 μm
Magnification	50-500X
Acquisition time	~20 s

Table 3.4: Operating parameters for SEM analysis of powder samples.

The powders were investigated in a Zeiss Supra 55 VP low vacuum field emission SEM, in which images of the powder were recorded using the secondary electron detector (SED). The operating parameters used in the investigations are given in table 3.4. Images of the powders were recorded using Zeiss SmartSEM software to reveal the geometry of the powder particles as well as the surface.
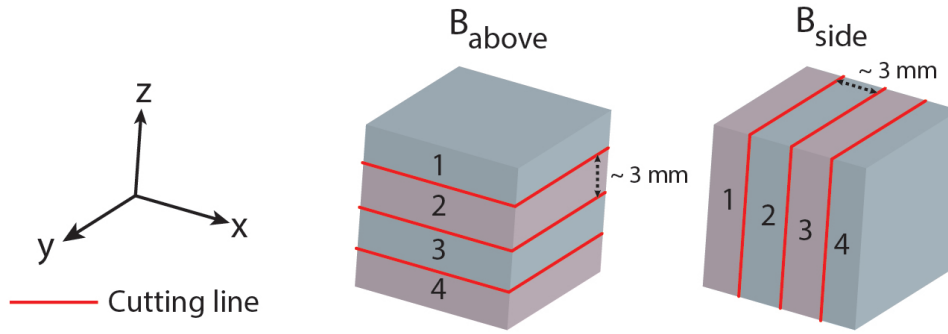
Figure 3.7: Cutting of B_{above} and B_{side} into microscopy samples.

3.4 Characterization of produced material

3.4.1 Specimen preparation

The cutting described in section 3.2.4 produced the bits used for material characterization. The two bits B_{above} and B_{side} were chosen for metallographic investigations. These bits were cut into four plates of roughly 3 mm thickness, as shown in figure 3.7. The samples from B_{above} provide the above view (xy-plane) while the B_{side} samples show the side view (yz-plane). The cutting was done using a Struers Accutom-5 machine with a SiC blade (10S15 by Struers). The rotation speed was set to 3000 rpm and the feed rate set to 0.05 mm/s.

After cutting, all the samples were grinded and polished in a similar fashion to the powder samples described in section 3.3.1. Waterproof SiC grinding papers were again used in the same sequence; P500, P800, P1200, P2400 and finally P4000. Samples were then polished using a Struers TegraForce-5 machine. Samples were first polished with 3 μm polishing disks for 5 minutes followed by 10 minutes of polishing with 1 μm polishing disk. All samples were rinsed in soap water an ethanol between each grinding and polishing step. Final polishing was done using OP-S standard colloidal silica suspension of size 0.04 μm for 9 minutes using the polishing machine, followed by rinsing in an ultrasound bath of water for 3 minutes to remove any silica particles.

Keller's etch		Weck's reagent	
HF	2 mL	$KMnO_4$	4 g
HCl	3 mL	NaOH	1 g
HNO_3	5 mL	H_2O	100 mL
H_2O	190 mL		
Immersion time	15 s	Immersion time	10 s

Table 3.5: Constituents of Keller's etch and Weck's reagent.

Polishing was the final sample preparation step for two of the four samples. These will henceforth be called the 'polished' samples. The remaining samples were etched in Keller's etch and Weck's reagent. The chemical composition of the two etchants is given in table 3.5. Immediately after etching, the samples were rinsed in water before being rinsed in ethanol. These samples will from now on be referred to as 'Keller' and 'Weck'.
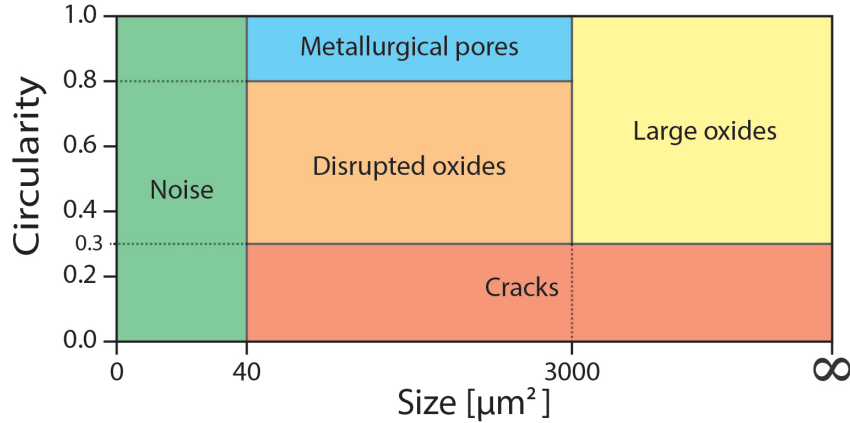
Figure 3.8: Categorization of porosity types.

3.4.2 Optical microscopy

Both the polished and etched samples were investigated using the same Leica MeF4 optical microscope described in section 3.3.2. Micrographs of the polished samples were recorded at low magnification in a raster similar to the investigation of the cast powder samples. These images were stitched together to study the porosity of the materials. The etched samples were studied at higher magnification to investigate the scan track structure.

Macrostructure and porosity

The polished samples were placed onto a stage disk of a small orifice so the sample completely covered the orifice. Using a total magnification of 50X, a raster of images was recorded to cover the entire orifice (see figure 3.5). These images were stitched together using the 'Photomerge' function in Adobe Photoshop CC. Unlike the powder samples, a square cropped area within the orifice was selected for analysis. After adjusting the contrast, the image was imported into ImageJ. A suitable threshold was chosen to select the porosity in the sample. The image was converted to a binary image showing the porosity as black on a white material background.

Using the 'Analyze particles' fuction in ImageJ, particles were filtered into categories based on their area size and circularity. The five such categories are illustrated in figure 3.8. Pores smaller than than 40 μm^2 were categorized as noise in the image. The category 'Metallurgical pores' was limited to nearly spherical pores (C>0.8) up to the size of $3000\mu m^2$. Pores of very low circularity (C<0.3) were considered to be cracks, while pores with intermediate circularity were categorized as disrupted oxides as described by Louvis, Fox, and Sutcliffe [8]. Meanwhile, pores of area greater than 3000 μm^2 and circularity parameter greater than 0.3 were considered 'large oxide pores'. The limit of 3000 μm^2 was chosen because the required area of a triangle to contain three particles of diameter of $30\mu m$ is approximately 3024 μm^2 (see figure 3.9). Therefore, this limit was set to distinguish between pores that could possibly contain unmelted powder particles and smaller disrupted oxide pores.

The pores were sorted into five separate binary image files, each containing one category of pores. The image analysis was then conducted on each file. For each pore, the center
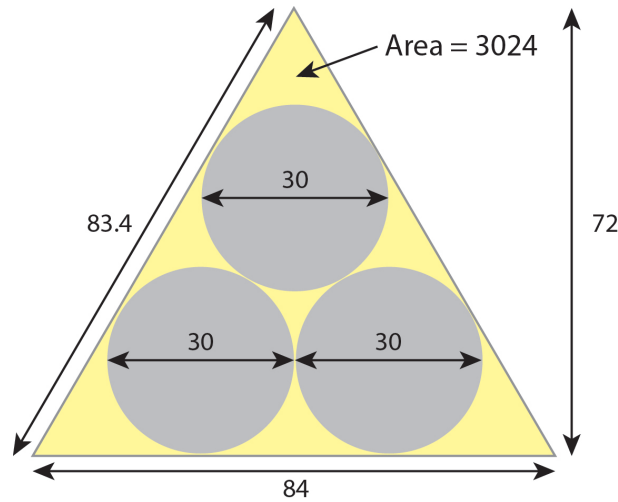
Figure 3.9: Minimum area for large oxide pores.

of area was recorded and using the 'Nearest neighbour distance' plugin [57]. Then the distance between the centers of mass of two neighbouring particles could be measured. In addition, a bounding rectangle was drawn. Thus the following parameters were recorded for each particle; the area, perimeter length, bounding rectangle width, bounding rectangle height, maximum feret diameter, minimum feret diameter and nearest neighbour distance (NND). Two polished samples for each orientation and each powder were evaluated in this way to enlarge the sample size.

Microstructure and melt pools

Etched samples were analysed using the same Leica MeF4 optical microscope used in sections 3.3.2 and 3.4.2. This investigation had two separate purposes. First, the scan tracks of the materials were imaged to study their structure. The second purpose was to evaluate and compare the suitability of the etchants for these alloys. Two materials times two orientations times two etchants resulted in eight samples were investigated. Variations of microscope settings were considered for each sample to produce the best possible images.

3.4.3   Scanning electron microscopy

All three sample preparation types (polished, Keller and Weck) were studied using the same SEM as for the powder investigation described in section 3.3.3. Immediately prior to the investigation the samples were rinsed in an ultrasound bath for three minutes to remove any contaminants from the surface.

Similar to the optical microscopy, the purpose of the investigation was both to evaluate the material as well as the etchants. Features of particular interest were various types of porosity as well as the microstructure at melt pool contours and in the center of melt pools. Various operating parameters were evaluated for imaging.

3.5 Mechanical testing

The produced material was subjected to both tensile and compressive testing to evaluate the mechanical properties of the materials. Test specimen were prepared from three differently oriented sections of the components to evaluate the anisotropy of the materials. The machining of test specimen was done by the workshop of the technical section at the Faculty of Natural Sciences and Technology at NTNU. Due to lack of material in each component, only one compression specimen and one tensile specimen was made for each material and orientation. The specimen had to be unusually small for the same reason. Thus the data collected was intended to give an indication of the compressive and tensile strengths, as opposed to a definitive value.

3.5.1 Compression testing

The three cylinders C_0, C_{45} and C_{90} that were cut off the base during post processing (see figure 3.3) were further machined into compression specimens. The cut off cylinders had a diameter of 12 mm and a length of 25 mm. The cylinders were then machined into smaller cylinder compression specimens of 15.00 mm height (h_0) and 10.00 mm diameter (d_0). The machining was done to ensure all specimen were exactly same dimensions and with smooth surfaces. The newly machined specimen were named the same as the cylinders from which they were made.

Compression tests were conducted using an MTS 880 machine which applies a force from an upper die onto the specimen tested (see figure 3.11a). The upper die moved at a constant velocity v_{die} of 1 mm/min towards the specimen placed on a stationary lower die. This sheets of Teflon were placed on the top and bottom of the specimen to act as a solid lubricant. Force-stroke data were collected at a rate of 20 Hz until one of four criteria was breached:

1. Height criterion: Test stopped if specimen height falls below 8 mm.

2. Load criterion: Test stopped if load exceeds machine capability

3. Fracture criterion: Test stopped if sample fractures

4. Time criterion: Stop test if load is converging and strain rate is very low.

After testing the data was imported into Microsoft Excel for analysis. The force F and stroke s, along with the initial volume V_0 were used to compute the height h, cross-sectional area A, stress σ and strain ε from formula provided by Valberg [58, ch. 7.5]:

$$h = h_0 - s \tag{3.3}$$

$$A = \frac{V_0}{h} \tag{3.4}$$

$$\sigma = \frac{F}{A} \tag{3.5}$$

$$\varepsilon = \frac{v}{h} \tag{3.6}$$
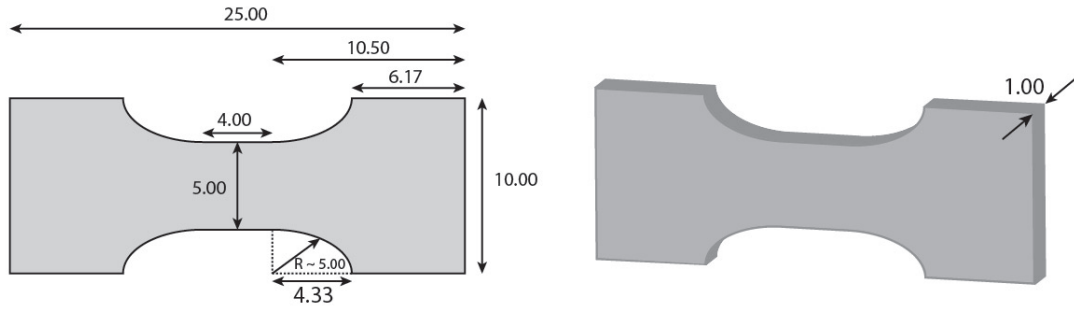
Figure 3.10: Dimensions for tensile test specimen.

3.5.2 Tensile testing

The remaining cylinders attached to the part B_{rest} were cut off to be machined into tensile specimen, named TT_0, TT_{45} and TT_{90} in the same manner as the comporession specimen. The cylinders were machined into specimen of the shape and dimensions shown in figure 3.10 (all values in mm).

The specimen were tested using a Zwick laserXtens Compact machine, in which an upper die pulls the specimen upwards until sufficient stress that fracture occurs (see figure 3.11b). Force F and strain ε data were recorded. A maximum loading criterion was set to 2.5 kN and a laser video extensometer was used to measure the strain.
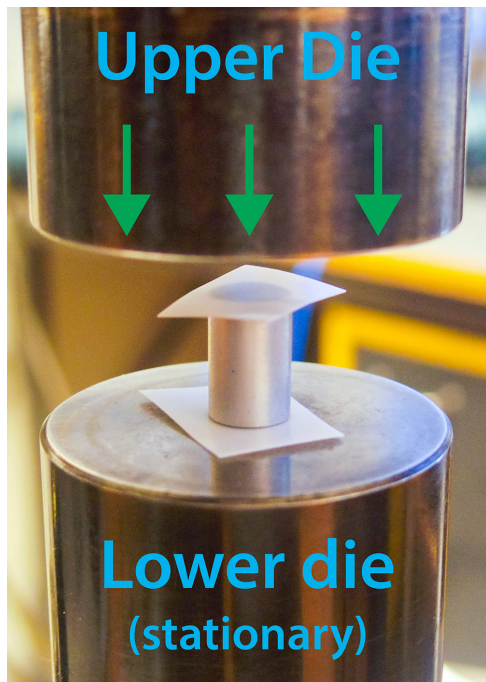
(a) Compression test.
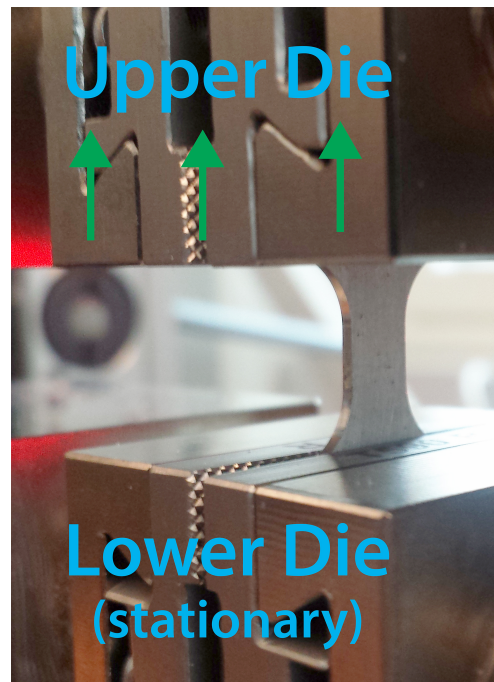
(b) Tensile test.

Figure 3.11: Mechanical testing of specimen.

4 Results

4.1 Powders

4.1.1 Observations from specimen preparation

In the early stages of sample preparation for optical microscopy, the powders were cast in epoxy using a glove bag placed in a fume hood. As powder was transferred from the container to the casting forms, there was a little spillage. This spilled powder was collected in a paper cup and kept in the glove bag while the epoxy hardened. As the glove bag was opened to collect the cast samples, the paper cup containing the powder was carefully removed from the glove bag, but kept in the fume hood. Because of this practical circumstance, the reactivity of the powder was investigated briefly.

There were no clearly observable signs of reaction in the cup. No fumes, heat or smell could be noticed, and the powder looked identical to that in the container and castings. The cup was first gently then firmly rattled, but this failed to encourage a noticeable reaction. Finally water was added to the cup using a pipette. Small droplets at first, then a larger quantity of water. Again, no noticeable signs of reaction were observed. Figure 4.1 shows images of the AlSi10Mg powder in the paper cup. When the experiment was repeated for AA6061, a little powder was placed in a paper cup. Again, no noticable signs of reaction were observed when the powder was taken out of the glove bag into non-inert surroundings.
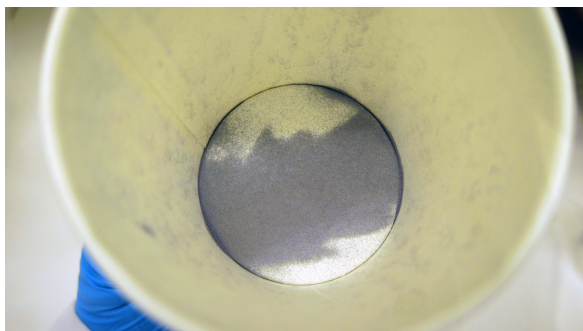
(a) Atmospheric surroundings.   (b) Aquatic surroundings.

Figure 4.1: AlSi10Mg powder in non-inert surroundings.

As for the castings, the powder was found to sink through the epoxy very quickly. For the non-stirred samples, the powder sunk to form a small mound on the bottom of the form within a second. For the stirred samples, the powder was distributed to form a
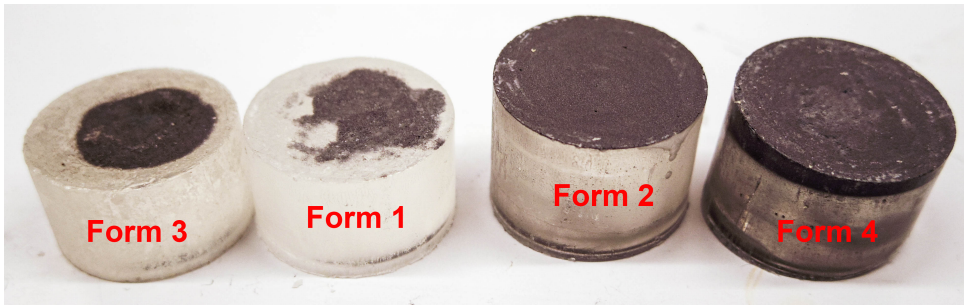
Figure 4.2: Castings of the AA6061 powder.

layer of even thickness at the bottom of the form. Again, the contents of the forms were motionless within seconds. Figure 4.2 shows the castings of the AA6061 powder after hardening.

During grinding and polishing the powders were found to adhere well to the epoxy. Once the samples were polished smooth, only very few craters could be found where powder particles had been ripped from the mounting. Especially during grinding it became evident that the samples with a small amount of powder were difficult to prepare. All the powder was grinded off several samples by mistake. The stirred castings were also found to be less transparent than the non-stirred ones, as is evident from figure 4.2 (forms 2 and 4 are less transparent than forms 1 and 3).
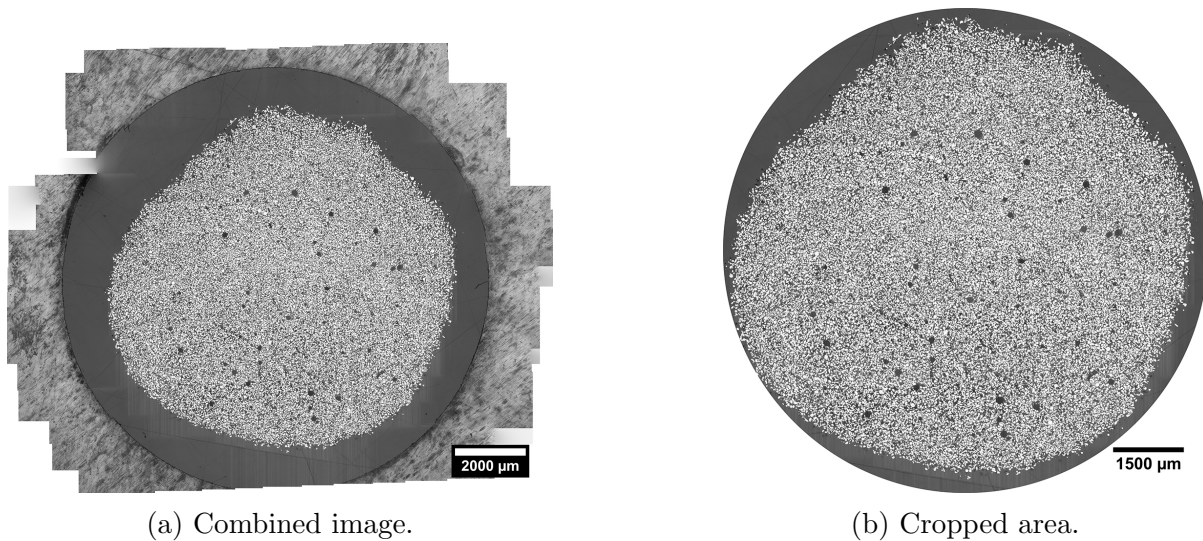
(a) Combined image.

(b) Cropped area.

Figure 4.3: Combined micrographs of AlSi10Mg powder.

4.1.2 Optical microscopy

A total of 195 micrographs were recorded to produce a combined image of the polished sample surface shown in figure 4.3. As can be seen from figure 4.3a, this sample was grounded slightly too much as the powder particles do not extent beyond the orifice. Nonetheless, there is still a sufficient number of particles within the sample to accurately describe the size and shape of the particles. Figure 4.4a depicts an enlarged part of figure 4.3b, showing that the size and geometry of each powder particle is imaged well. The binary representation of these particles are shown in figure 4.4b, which is overlayed onto
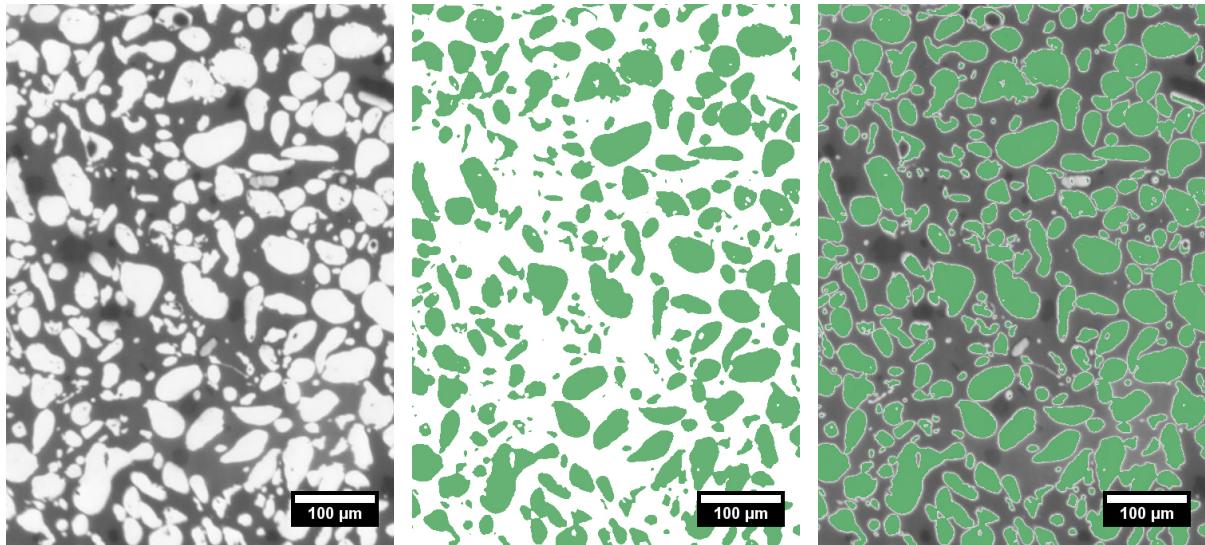
(a) Micrograph.　　　　(b) Binary image.　　　　(c) Overlay image.

Figure 4.4: Detailed and binary image of AlSi10Mg powder.

the micrograph in figure 4.4c. From figure 4.4 it is clear that the binary representation captures the geometry of the powder particles well. Figure 4.5 shows a higher magnification image of the AlSi10Mg powder, from which it is clear that the particles contain multiple phases as well as inherent pores.
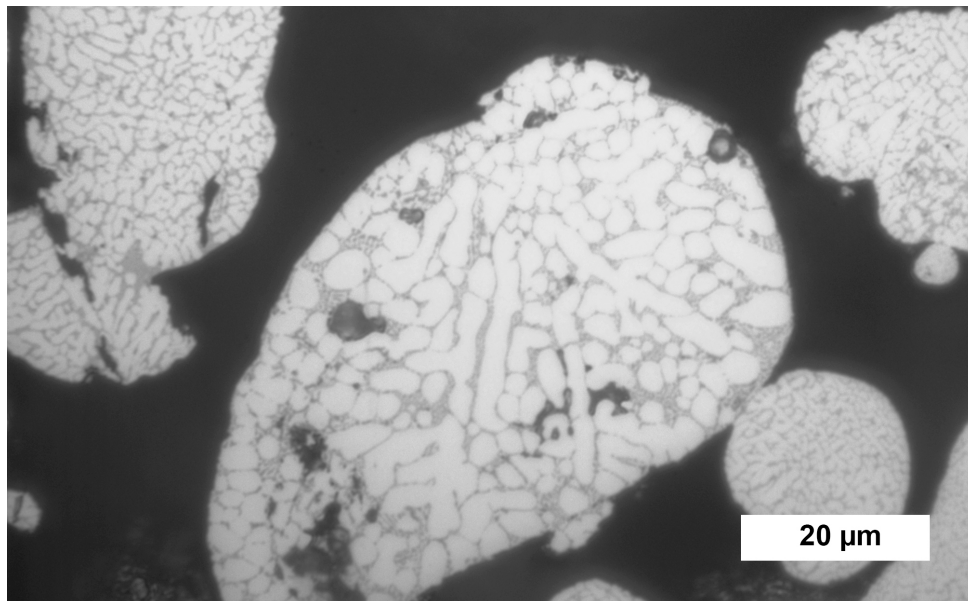
Figure 4.5: High magnification OM image of AlSi10Mg powder.

A combined image made from 290 micrographs of the AA6061 powder is shown in figure 4.6. Figure 4.7 shows an enlarged part along with the binary image, similar to what is shown in figure 4.4. Again the binary image shows good correlation with the detailed image.

(a) Combined image.
(b) Cropped area.
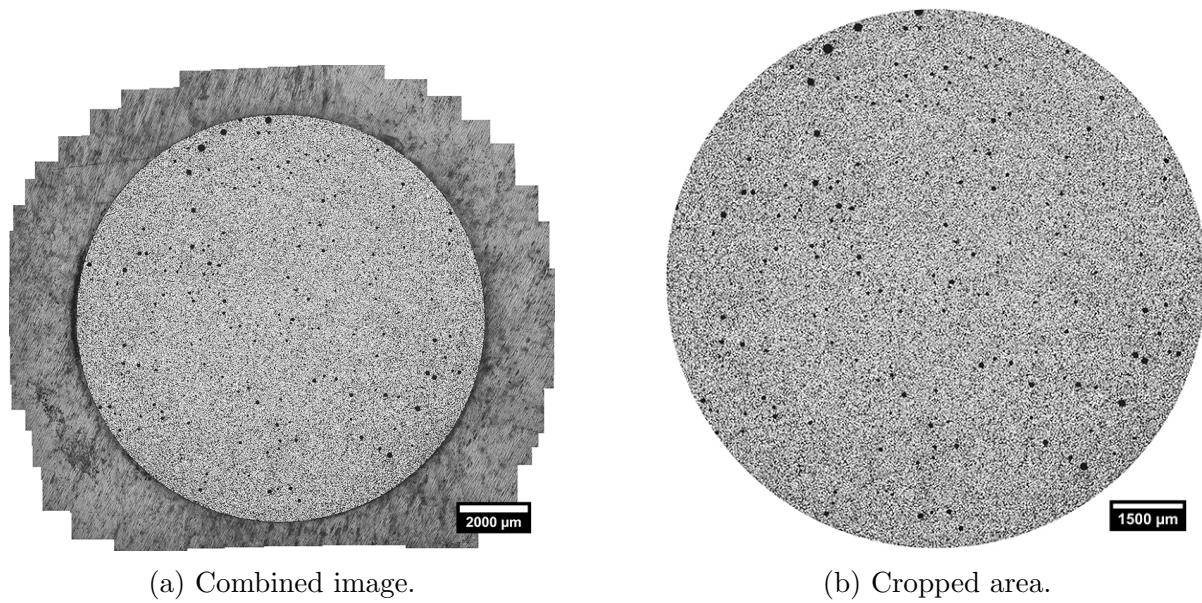
Figure 4.6: Combined micrographs of AA6061 powder.

(a) Micrograph.
(b) Binary image.
(c) Overlay image.
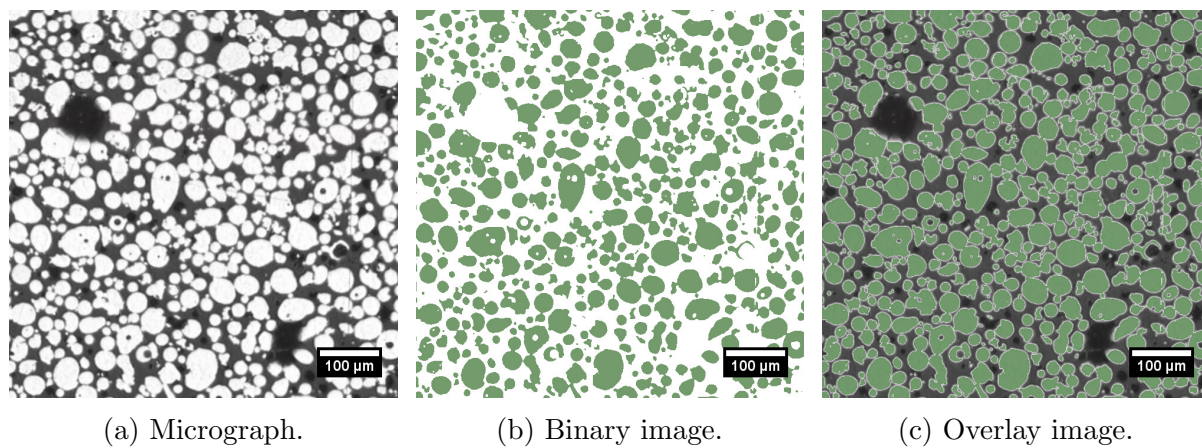
Figure 4.7: Detailed and binary image of AA6061 powder.
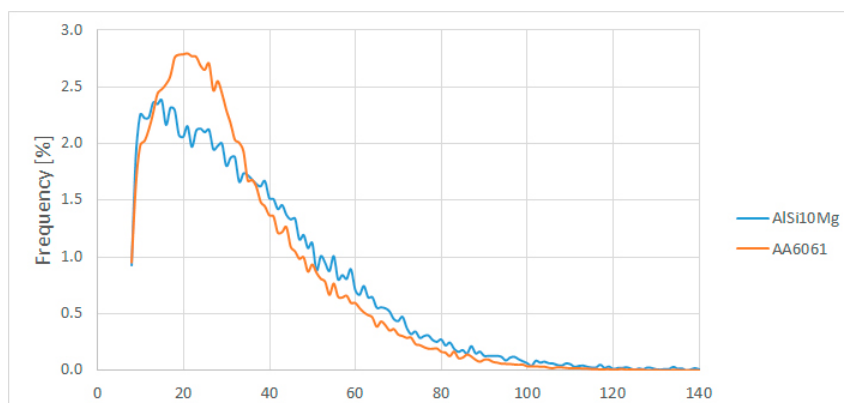
Figure 4.8: Size distribution of the powder particles.

4.1.3 Particle size and geometry distribution

.

Powder	Number of particles			
	Total recorded		Included in dataset	
AlSi10Mg	44 435		37 291	
AA6061	92 794		77 739	
	Size			
	Average	Median	Peak frequency	Standard deviation
AlSi10Mg	36.4 μm	31.7 μm	15 μm	22.2 μm
AA6061	32.8 μm	28.2 μm	21 μm	19.0 μm
	Circularity			
	Average	Median	Peak frequency	Standard deviation
AlSi10Mg	0.67	0.70	0.83	0.20
AA6061	0.73	0.81	0.91	0.21

Table 4.1: Average size and circularity of powder particles.

The data collected from the micrographs included some noise which was removed by filtering out particles of areas smaller than 25 μm^2. The average size and circularity of the dataset is given in table 4.1. Figure 4.8 shows frequency plots of the powders' size within classes of ± 0.5 μm. The frequency is all but negligible for sizes greater than 100 μm. AA6061 has a slightly higher peak than AlSi10Mg which accounts for the slightly smaller standard deviation found in table 4.1. Both powders show a rapid decline in the frequency of powders smaller than about 10 μm, but this coincides with the data filtered out as noise. Unfortunately the peak of AlSi10Mg is within this size range, so the average size in table 4.1 may be overestimated. Neither size distribution is particularly symmetrical and in both cases the average size is considerably greater than both the median and especially the peak frequency.
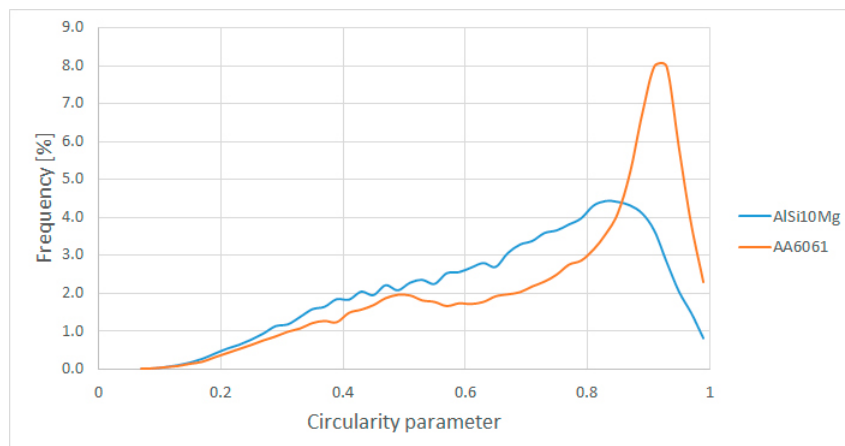
Figure 4.9: Circularity distributions of the powder particles.

The frequency of the circularity of the powders within classes of ± 0.01 have bee plotted in figure 4.9. For both powders the frequency of circularities less than 0.2 are negligible, and the frequency increases for greater circularity. The peak of AA6061 is both higher and closer to 1 than AlSi10Mg. As shown in table 4.1, the average and median circularity of AA6061 is greater than that of AlSi10Mg. Thus the AA6061 powder is more spherical.

4.1.4 Scanning electron microscopy

The SEM micrographs in figure 4.10 agree with the findings of the OM analysis that AlSi10Mg is less spherical than AA6061. Both powders show many instances of smaller particles attached to larger ones (commonly known as 'satellites'). The size of the particles is consistent with the data found from the OM samples.

(a) AlSi10Mg low magnification.
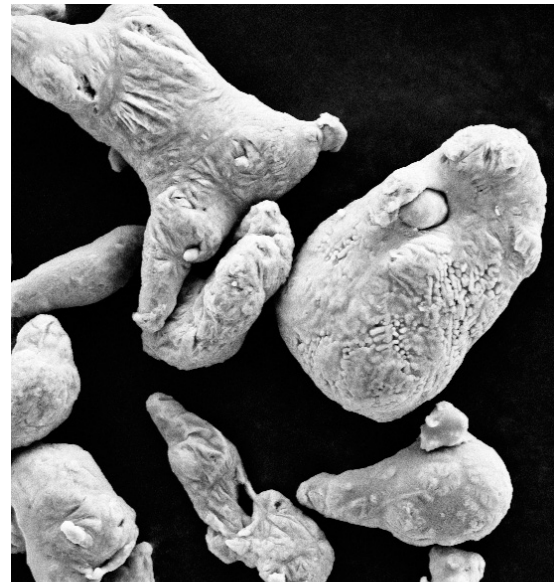
(b) AlSi10Mg high magnification.
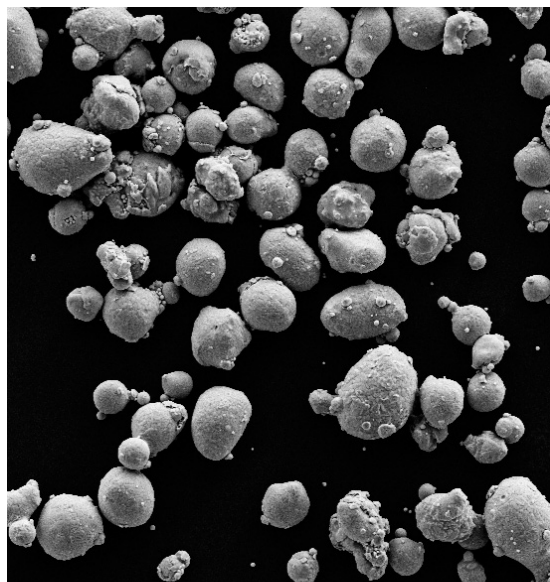
(c) AA6061 low magnification.
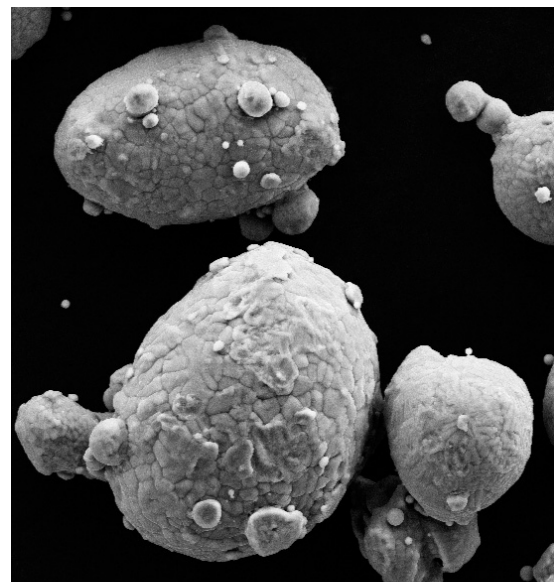
(d) AA6061 high magnification.

Figure 4.10: SEM images of powders.

4.2 Porosity

4.2.1 Images of polished samples

The combined optical micrographs of the polished samples are shown in figure 4.11. The most striking difference between the two materials is the large amounts of cracks present in AA6061 that do not appear in AlSi10Mg. In both materials large oxide pores are present in a variety of sizes. Figure 4.12 shows magnified images of the same samples shown in figure 4.11. Smaller pores are visible in both materials, but it is difficult to distinguish between small disrupted oxide porosity and metallurgical porosity. Nonetheless, the AlSi10Mg pores look more spherical in shape than the most AA6061 pores.
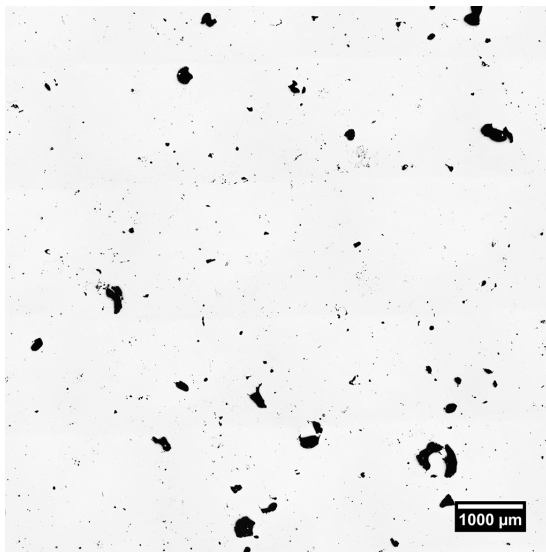
(a) AlSi10Mg above view.
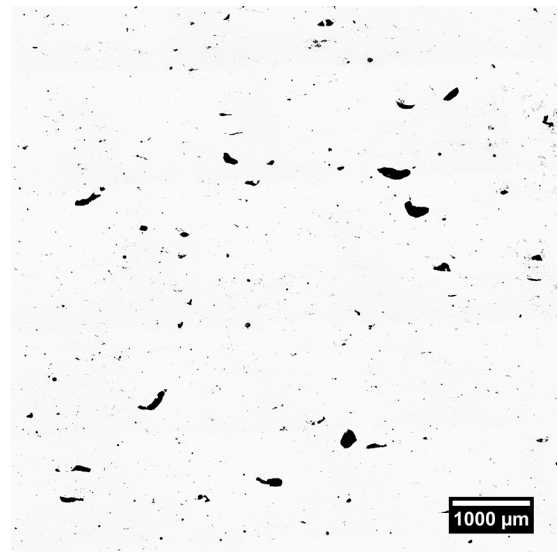
(b) AlSi10Mg side view.
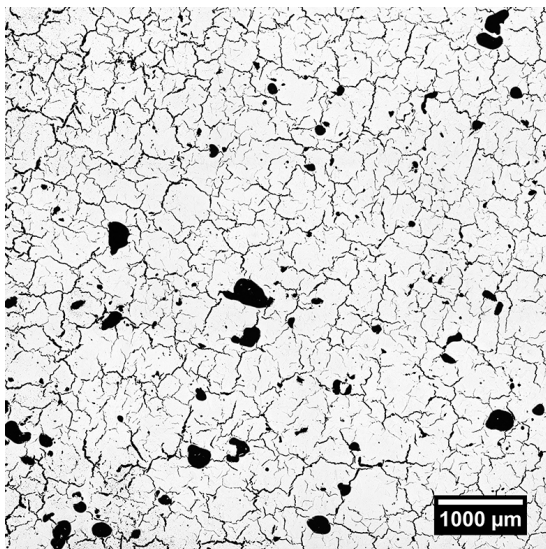
(c) AA6061 above view.
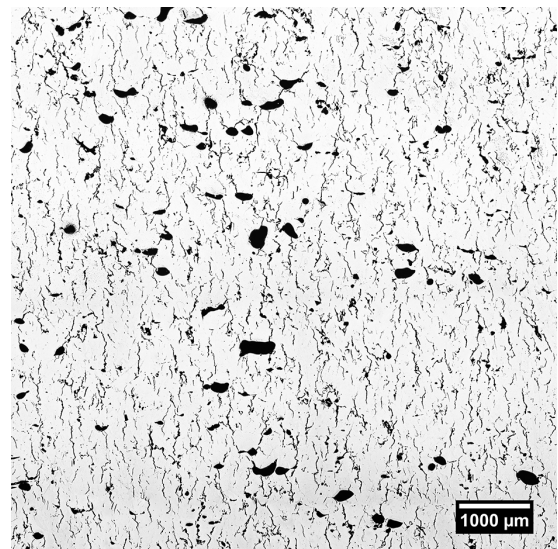
(d) AA6061 side view.

Figure 4.11: Overview images of polished specimens.

(a) AlSi10Mg above view.

(b) AlSi10Mg side view.

(c) AA6061 above view.
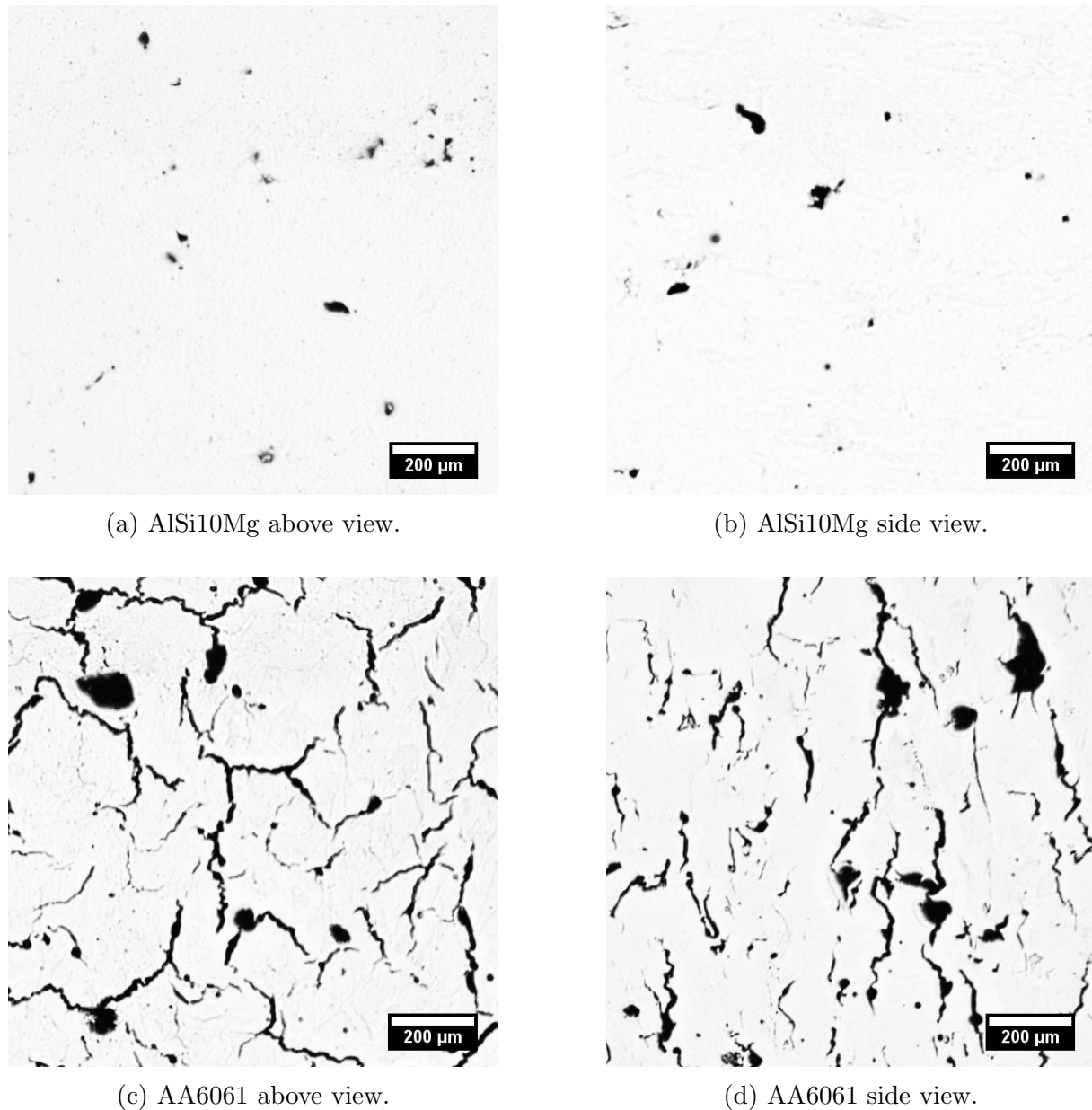
(d) AA6061 side view.

Figure 4.12: Magnified images of polished specimen.

Figure 4.12 clearly shows that the cracks in AA6061 samples are oriented vertically in the side view, while they appear randomly oriented in the above view. No clear correlation can be observed between the crack direction and the presence of other types of porosity. Cracks variably stop at, go through or narrowly avoid other pores.

4.2.2 Binary images

Figures 4.13 to 4.16 show the resulting images of the binary investigation for the two powders in two orientations. These images have been magnified to make the smaller details visible, and thus only show part of the surface examined. The micrograph is included, as well as the separate binary images and finally an overlay image showing the correspondence between the micrograph and the binary images.
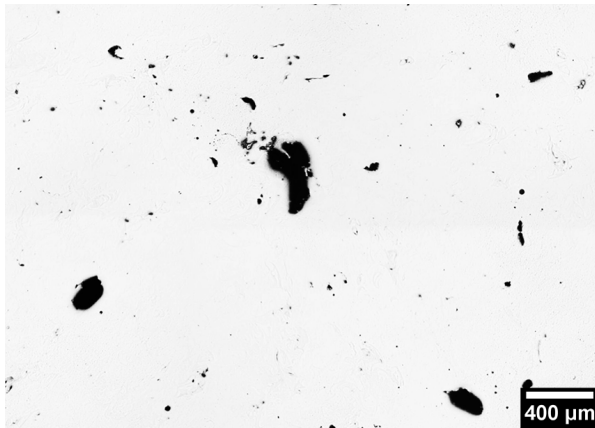
(a) Micrograph.

(b) Metallurgical pores.
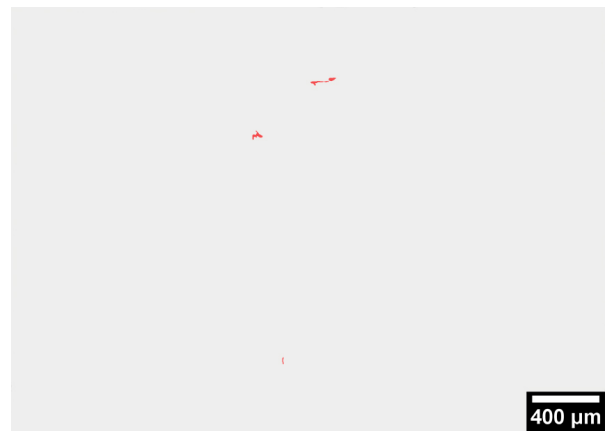
(c) Disrupted oxides.

(d) Cracks.
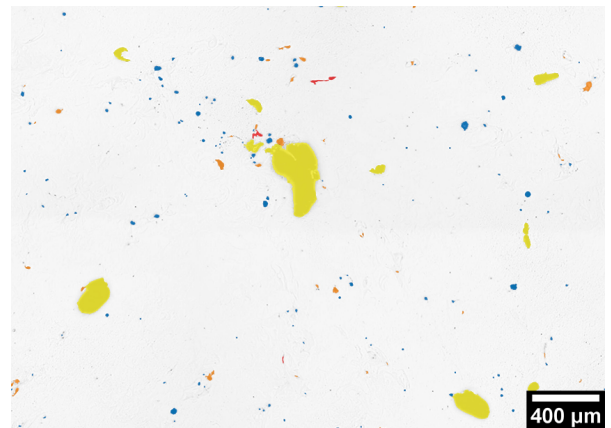
(e) Large oxides.

(f) Overlay image.

Figure 4.13: Binary images of AlSi10Mg above view.
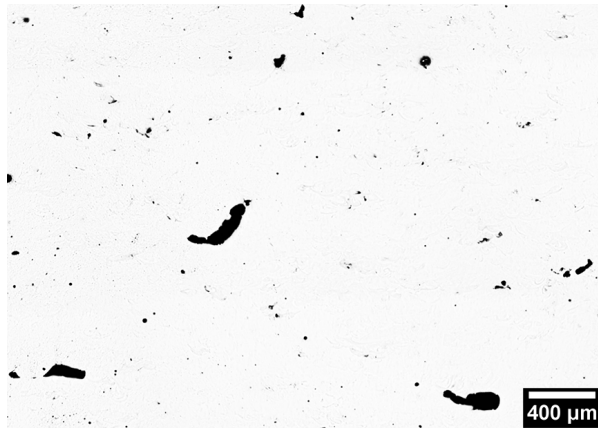
(a) Micrograph.

(b) Metallurgical pores.

(c) Disrupted oxides.

(d) Cracks.
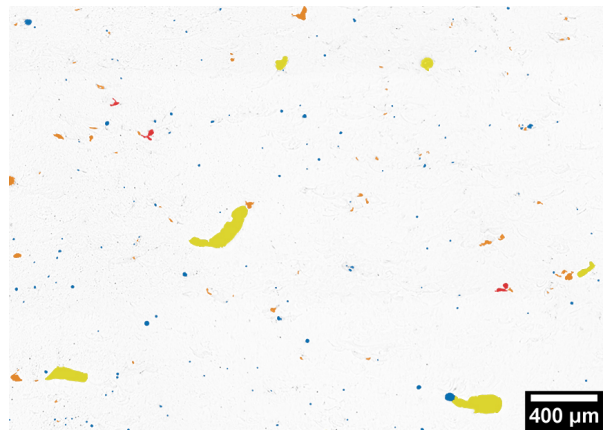
(e) Large oxides.

(f) Overlay image.

Figure 4.14: Binary images of AlSi10Mg side view.
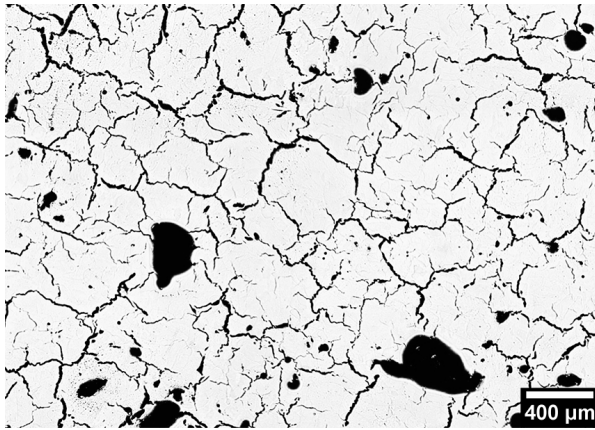
(a) Micrograph.
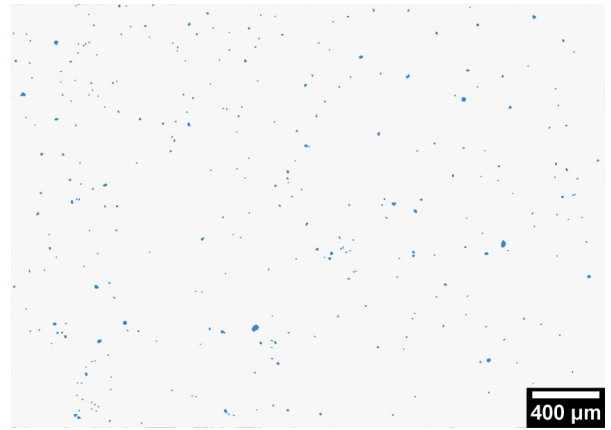
(b) Metallurgical pores.
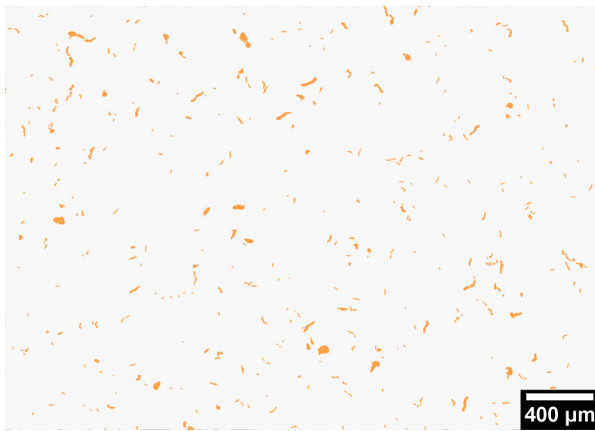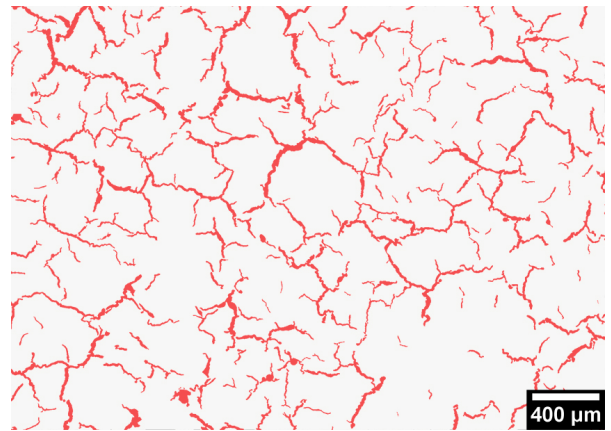
(c) Disrupted oxides.

(d) Cracks.
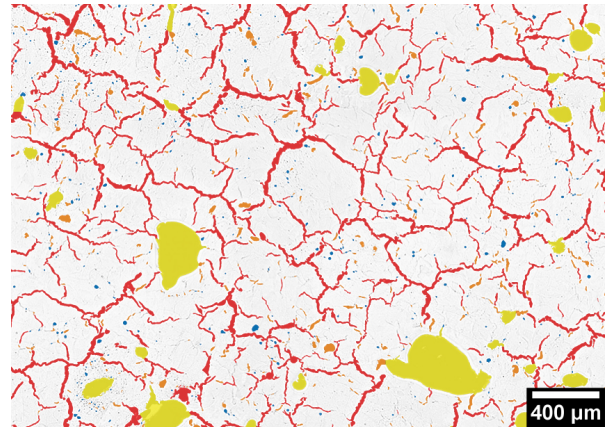
(e) Large oxides.

(f) Overlay image.

Figure 4.15: Binary images of AA6061 above view.
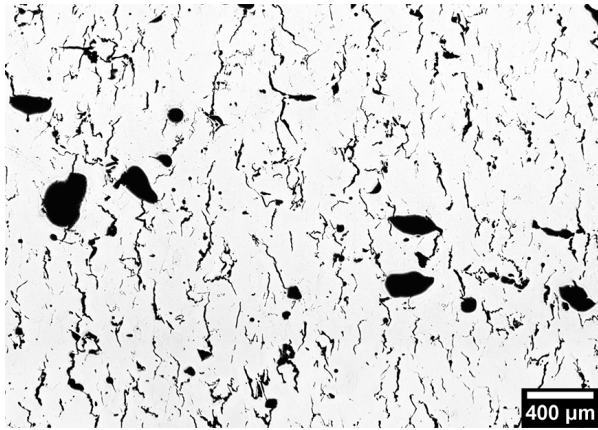
(a) Micrograph.
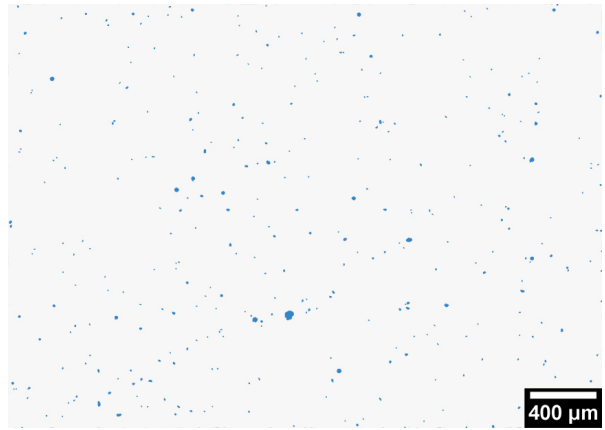
(b) Metallurgical pores.
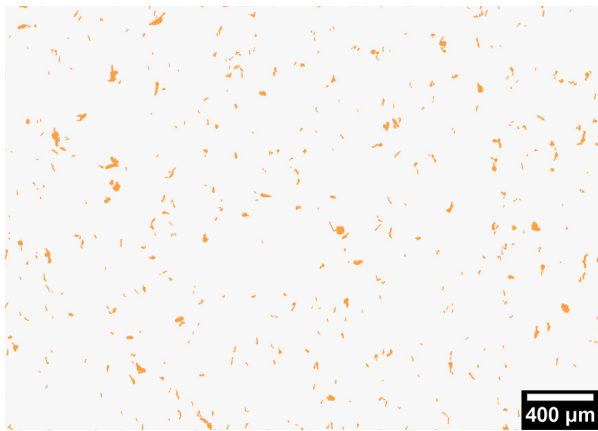
(c) Disrupted oxides.
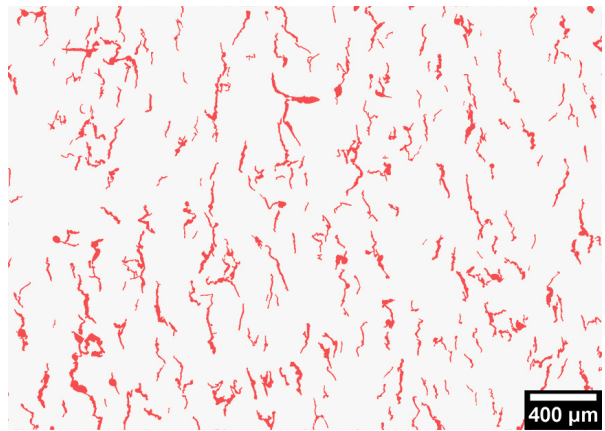
(d) Cracks.

(e) Large oxides.
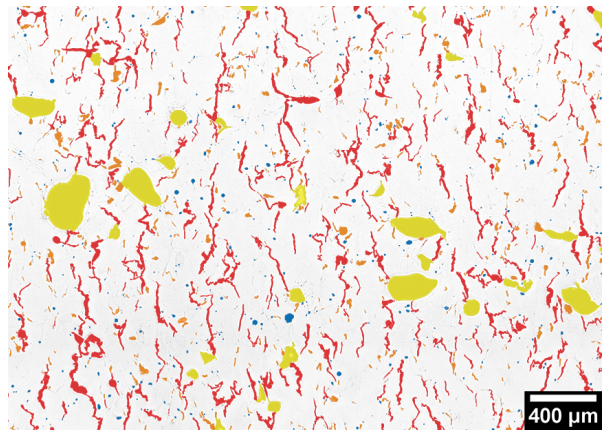
(f) Overlay image.

Figure 4.16: Binary images of AA6061 side view.

	AlSi10Mg			AA6061		
	Above	Side	Average	Above	Side	Average
Total area examined	130.7 mm^2	120.9 mm^2	-	98.6 mm^2	129.5 mm^2	-
Metallurgical pores	0.25%	0.24%	0.24%	0.43%	0.51%	0.47%
Cracks	0.04%	0.04%	0.04%	7.64%	6.22%	6.93%
Disrupted oxides	0.23%	0.27%	0.25%	1.18%	1.70%	1.44%
Large oxides	1.98%	1.14%	1.56%	3.68%	3.65%	3.67%
Total porosity	2.50%	1.68%	2.09%	12.92%	12.08%	12.50%
Relative density	97.50%	98.32%	97.91%	87.08%	87.92%	87.50%

Table 4.2: Area fraction of different types of pores.

4.2.3 Analysis of binary images

Data regarding the size and shape of each individual pore was recorded for the surfaces investigated. As the area of the surface was recorded as well, the area fraction of each type of pore could be computed. The results of these calculates are given in table 4.2. Due to the large surface areas investigated, it is assumed that the area fraction is a good indication for the relative density of the material. As the table shows, the relative density of the AlSi10Mg and AA6061 components are 97.9% and 87.5% respectively. The data from the table also shows that it is not just the cracks alone that cause the density of the AA6061 material to be low. The area fraction of all types of pores are greater for AA6061 than for AlSi10Mg.

One of the parameters collected for each pore was the nearest neighbour distance (NND). As each category of pore were placed in a separate binary image, the NND to another pore of the same type could be computed. Figure 4.17 shows the NND distribution for cracks in the AA6061 specimen. Despite the different orientations of cracks in the above view and side view, the nearest neighbour distance distributions are nearly identical.
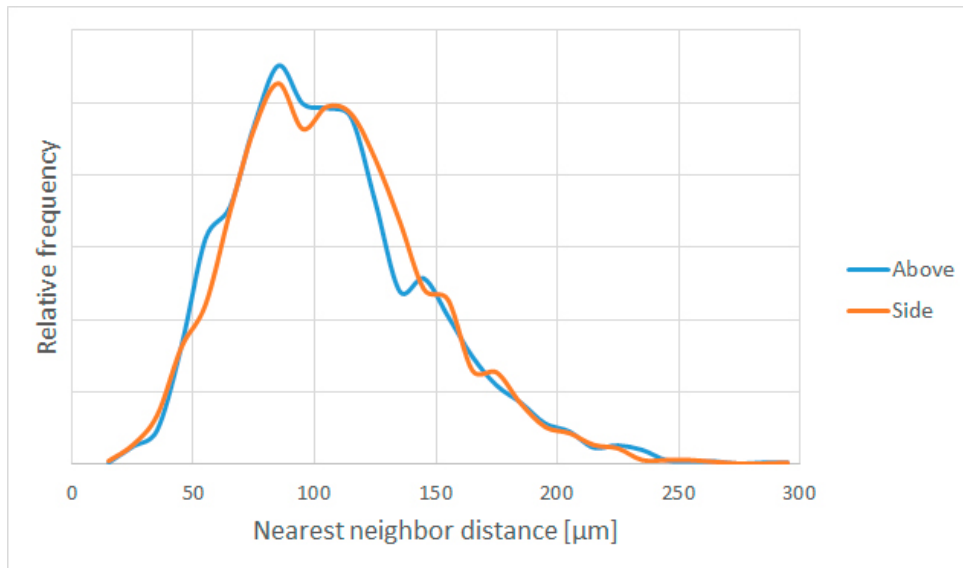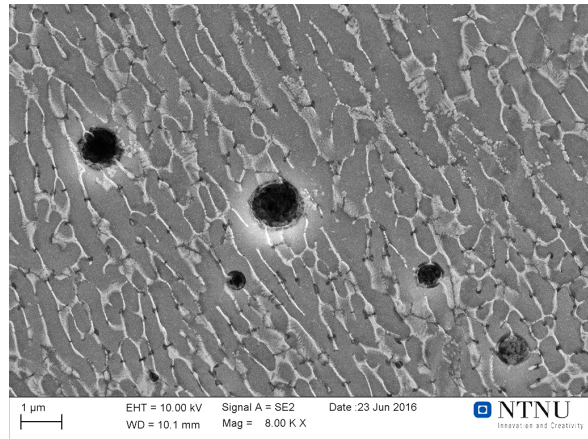

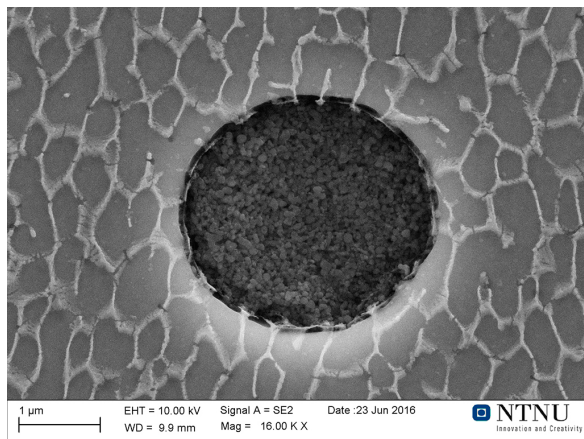Figure 4.17: NND distribution for cracks in AA6061 specimen.

4.2.4   SEM images

Figure 4.18 shows images of various metallurgical pores found in AlSi10Mg samples. These pores were found to have diameters ranging from 0.1 to 3 μm, and the shape was found to deviate to various degrees from a perfect spherical shape.
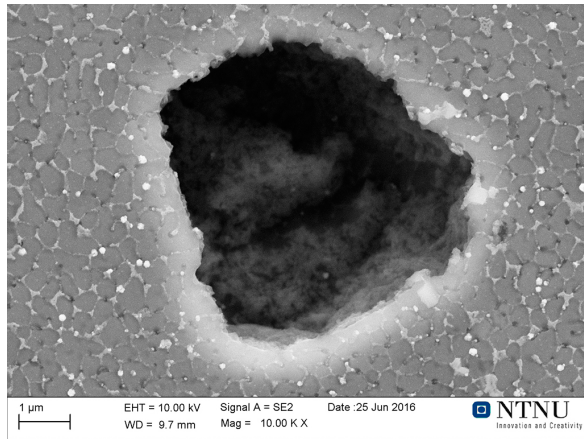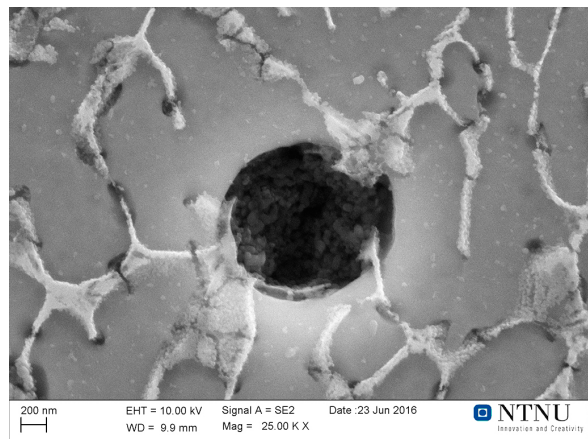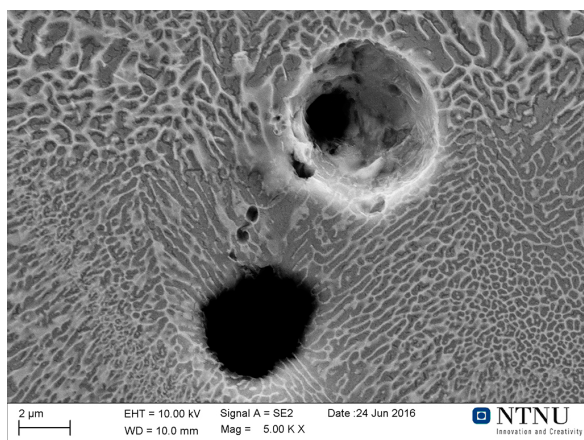

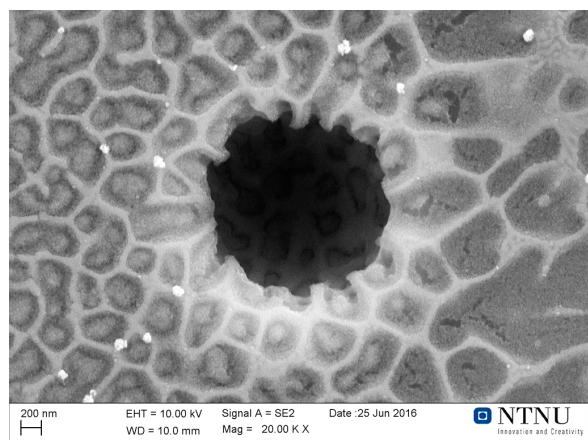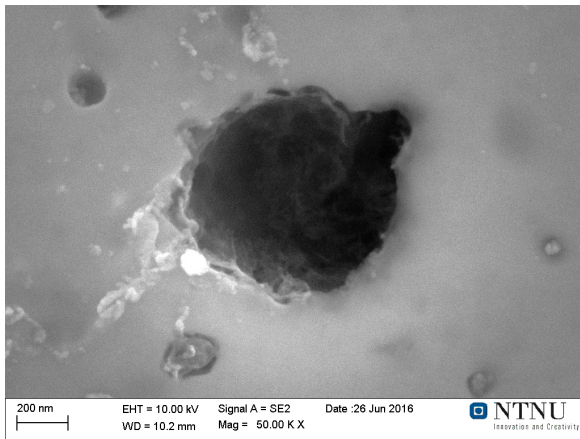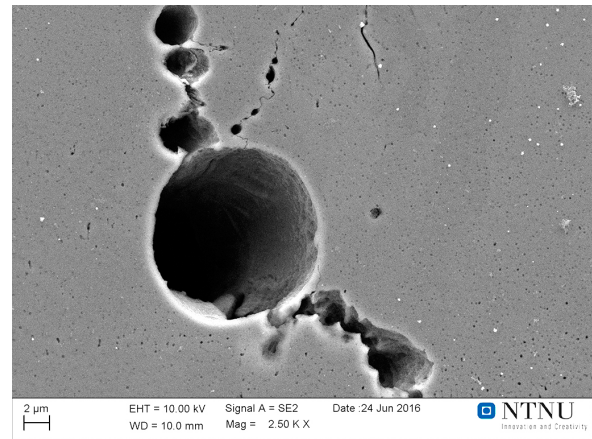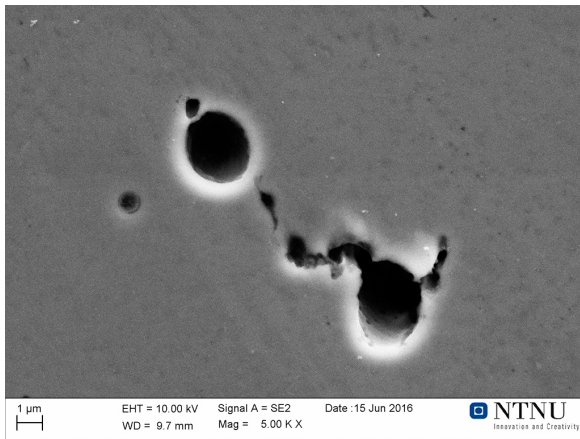Figure 4.18: SEM images of metallurgical pores in AlSi10Mg samples.

Figure 4.19 shows images of various metallurgical pores found in AA6061 samples. These vary more in size than the pores found in AlSi10Mg, as have diameters exceeding 10 μm. Note from figure 4.19d how some cracks seem to pass through metallurgical pores.
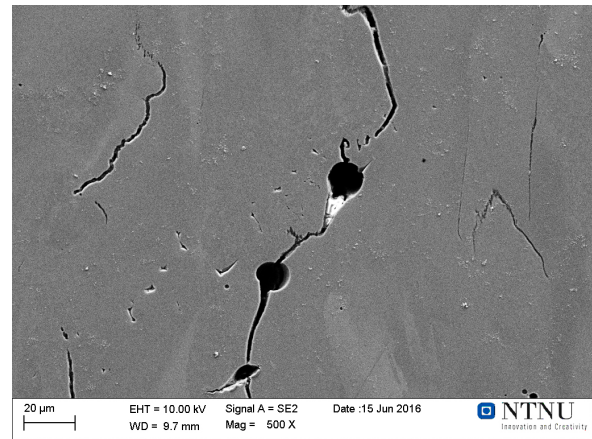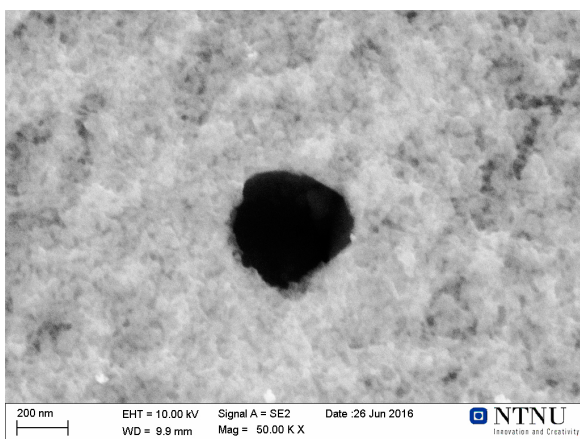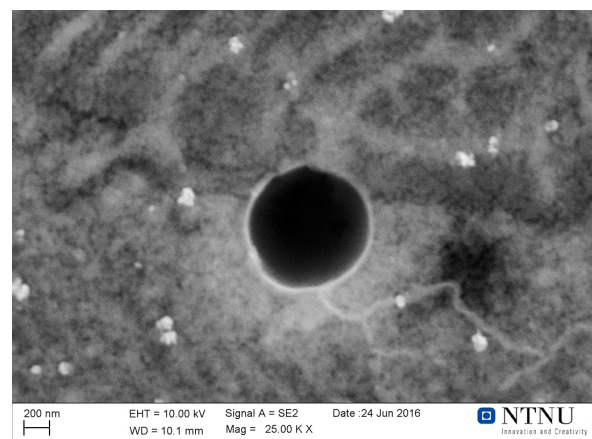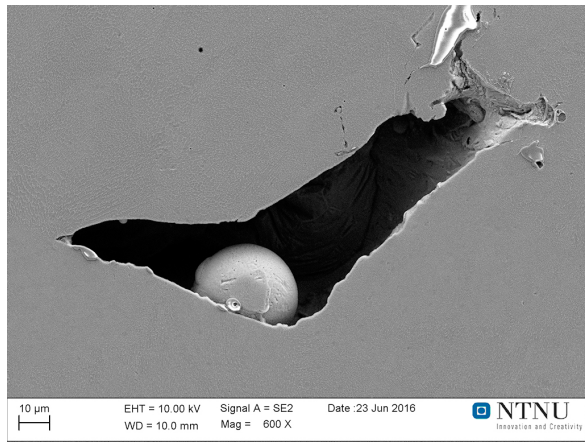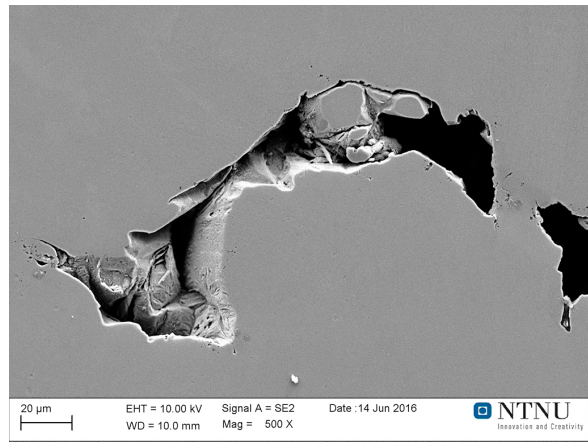

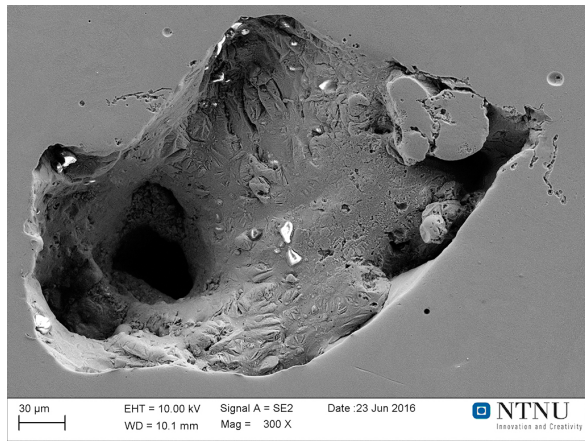Figure 4.19: SEM images of metallurgical pores in AA6061 samples.

Images of various oxide pores in AlSi10Mg samples are shown in in figure 4.20. The size ranges from roughly 20 μm (4.20e) to 300 μm (4.20c). Some of these pores clearly contain unmelted powder particles. The shape and orientation of the pores varies considerably.
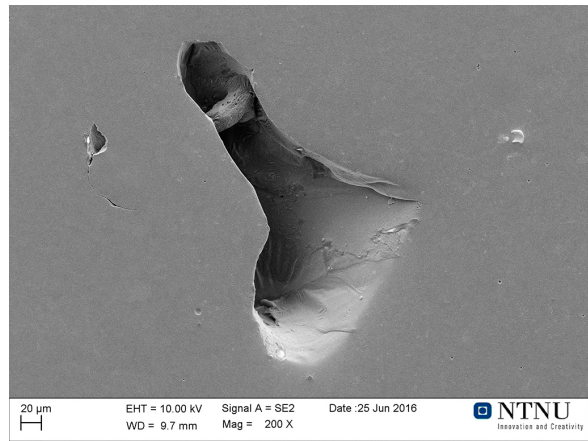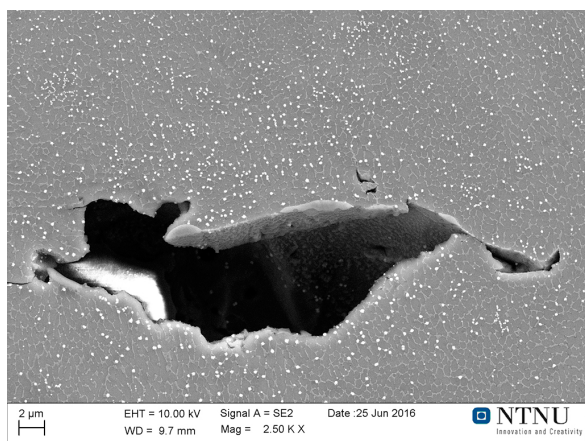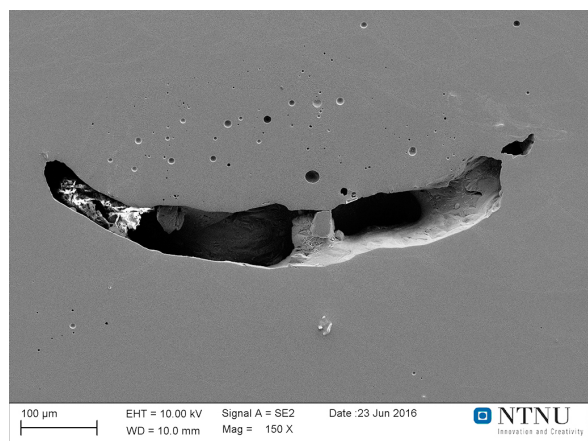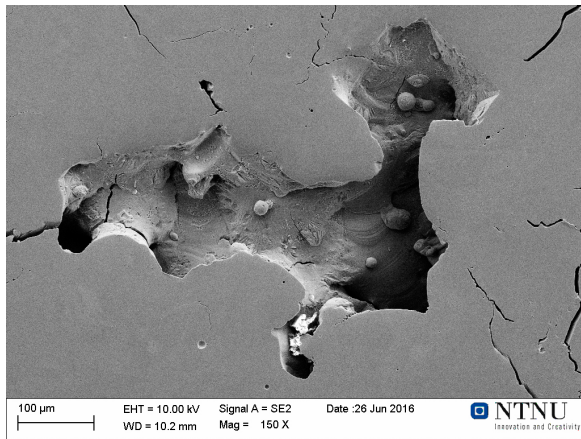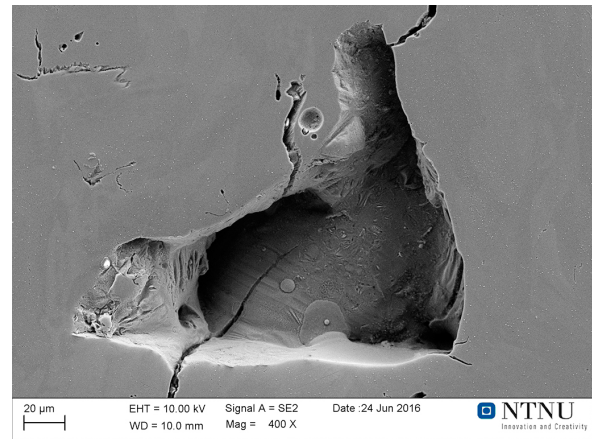

(a)

(b)

(c)

(d)

(e)

(f)

Figure 4.20: SEM images of oxide pores in AlSi10Mg samples.

Figure 4.21 shows various oxide pores in AA6061 samples. The size and shape range of these pores are very similar to the pores found in AlSi10Mg. Another similarity is that several pores contain unmelted powders in both materials.
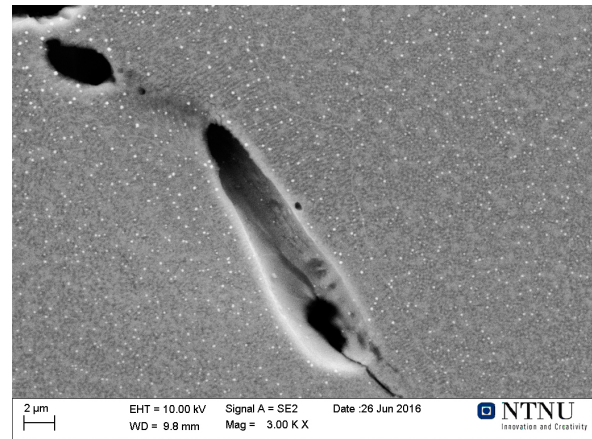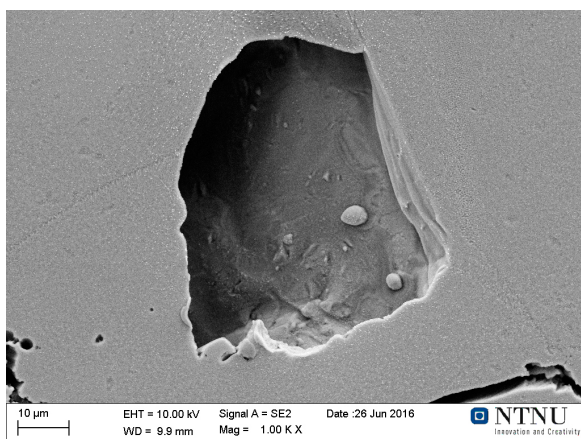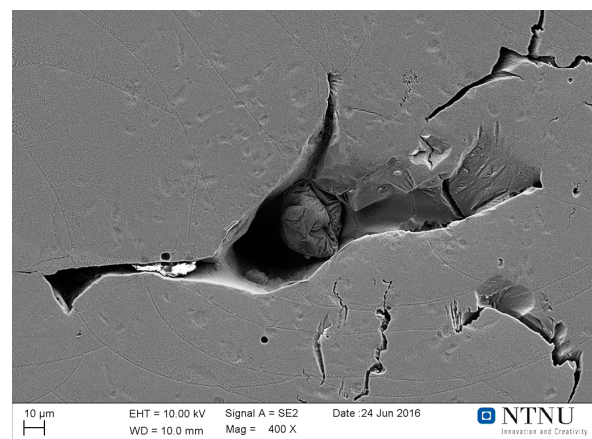
Figure 4.21: SEM images of oxide pores in AA6061 samples.

SEM images of cracks in AA6061 samples are shown in figure 4.22. In short, there is great variety in the cracks. Their lengths vary from less than 10 to several hundred micron. The width of most cracks is less than 2 μm, but some expand to much greater widths. The edges of the cracks also vary, as some are smooth while others change directions often and abruptly.

(a)

(b)

(c)

(d)

(e)

(f)
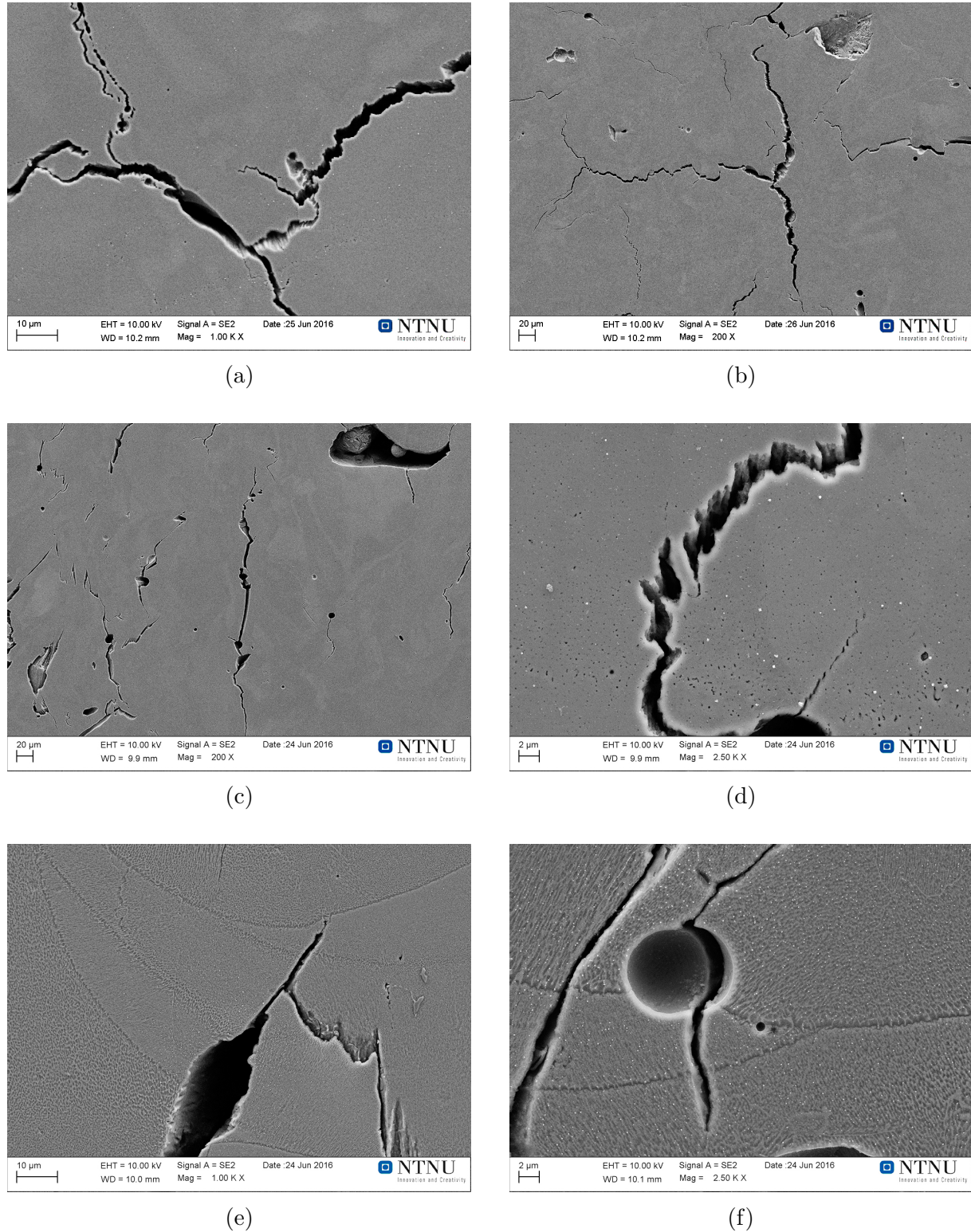
Figure 4.22: SEM images of cracks in AA6061 samples.

4.3 Etchants

Figures 4.23 and 4.24 show OM micrographs of specimens with various surface prepara-
tions. These are followed by figures 4.25 and 4.26 that show similar SEM micrographs.
The images are grouped in this manner to compare the effect of the preparations easily.
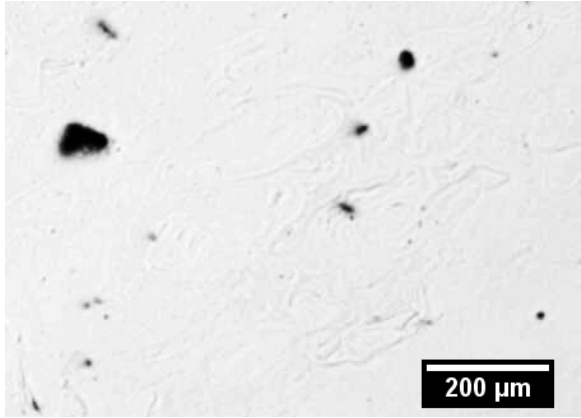
(a) Polished above view.
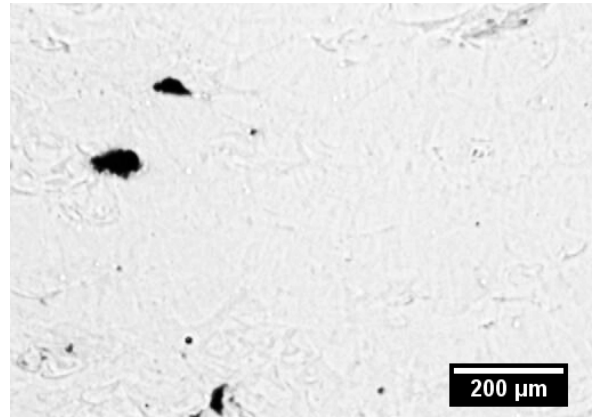
(b) Polished sided view.
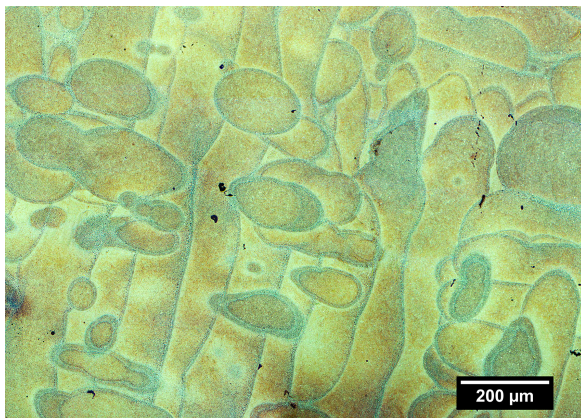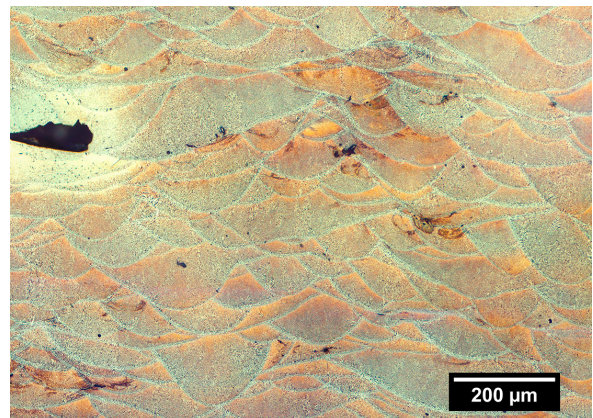
(c) Keller above view.
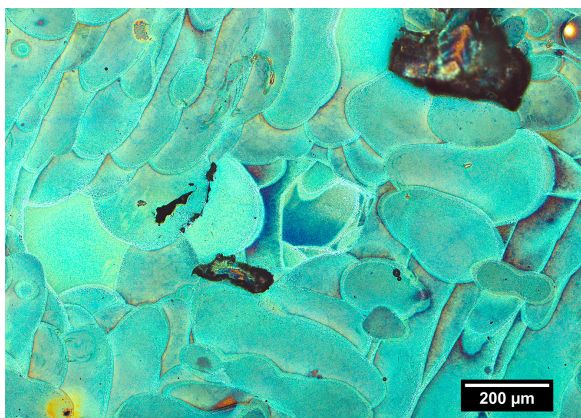
(d) Keller side view.
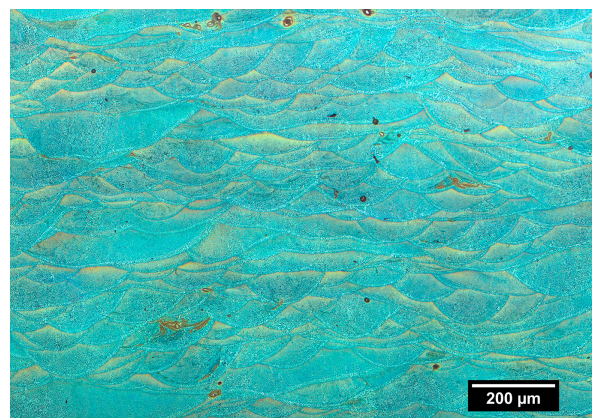
(e) Weck above view.

(f) Weck side view.

Figure 4.23: OM images of AlSi10Mg specimen with various surface preparations.
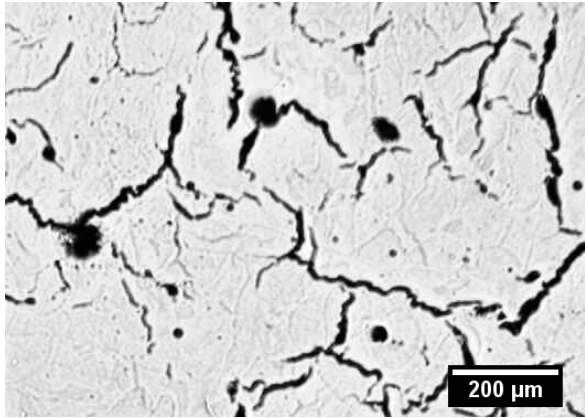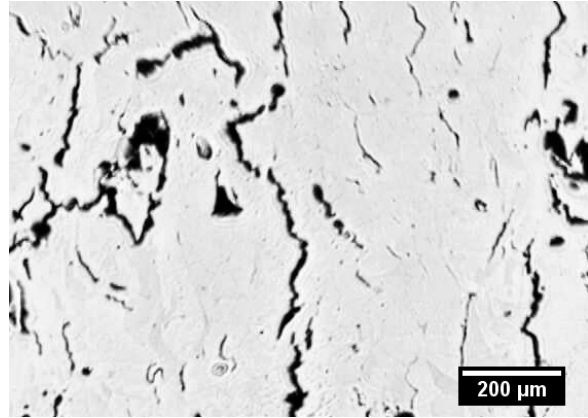
(a) Polished above view.

(b) Polished sided view.
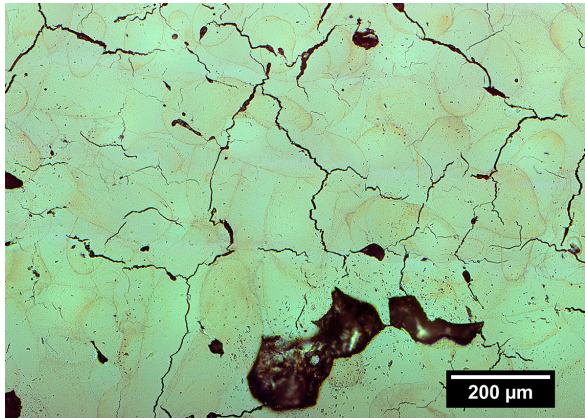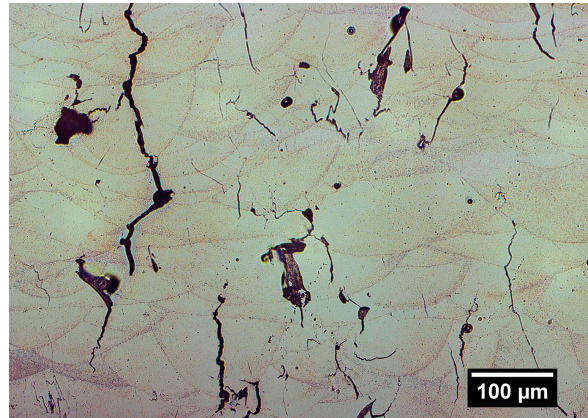
(c) Keller above view.
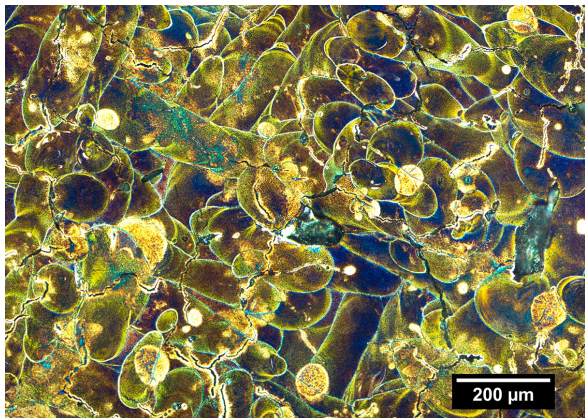
(d) Keller side view.
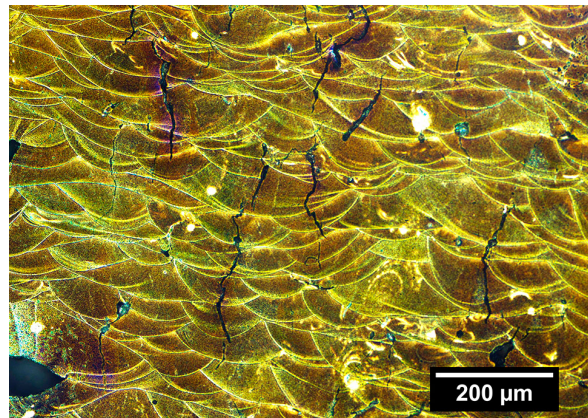
(e) Weck above view.

(f) Weck side view.

Figure 4.24: OM images of AA6061 specimen with various surface preparations.
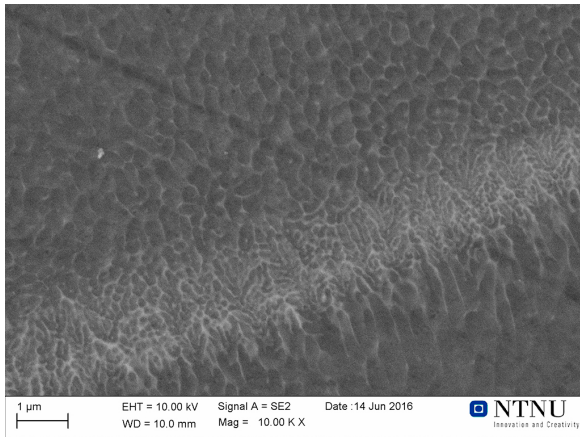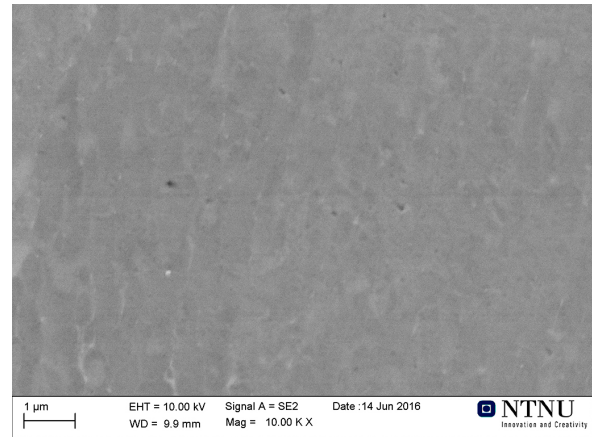
(a) Polished above view.

(b) Polished sided view.
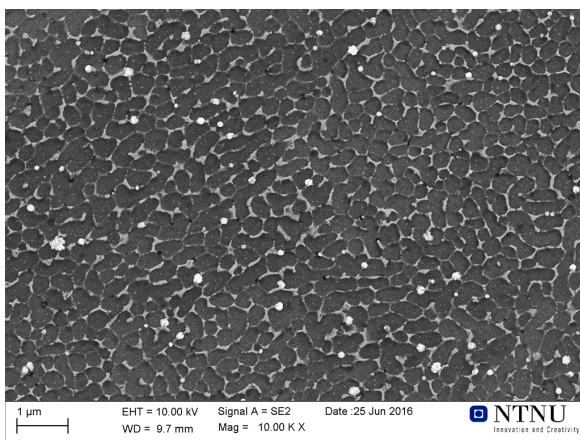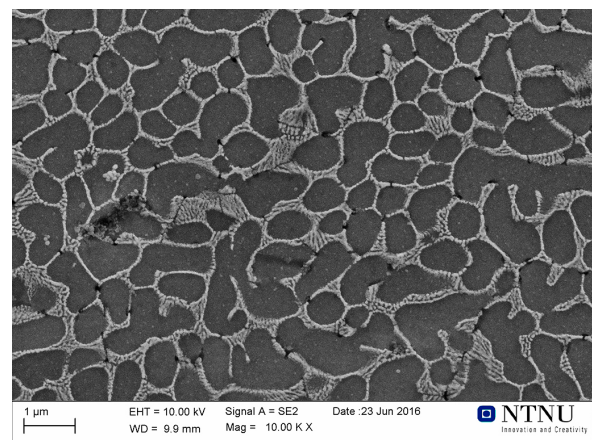
(c) Keller above view.
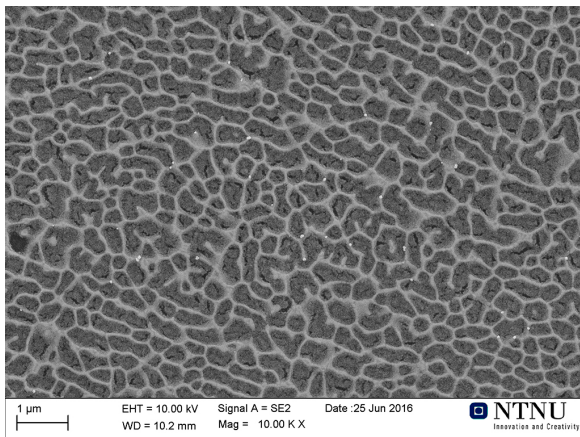
(d) Keller side view.
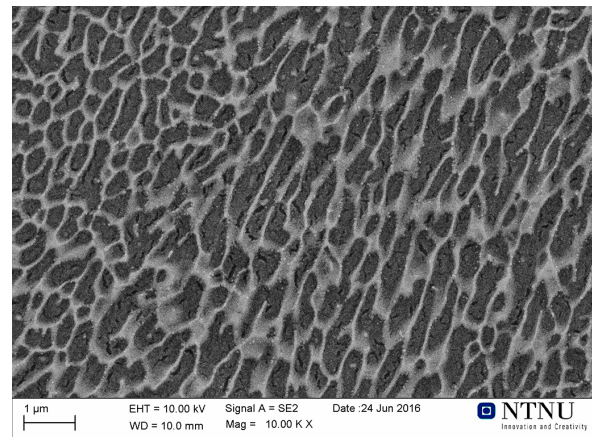
(e) Weck above view.

(f) Weck side view.

Figure 4.25: SEM images of AlSi10Mg specimen with various surface preparations.
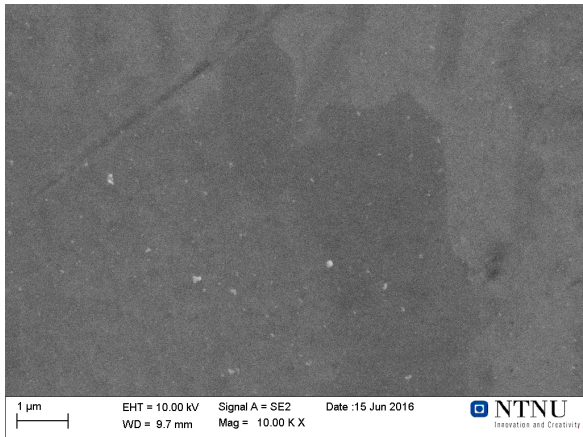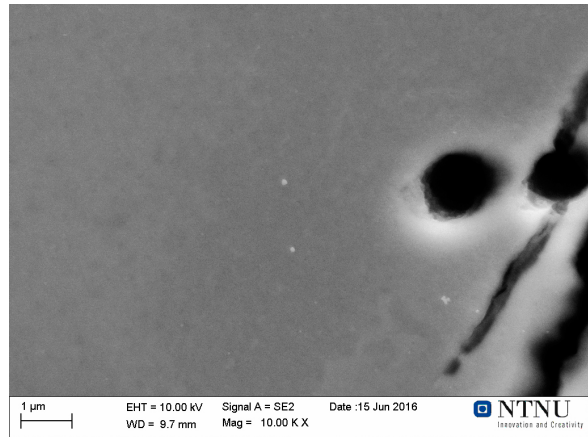
(a) Polished above view.

(b) Polished sided view.
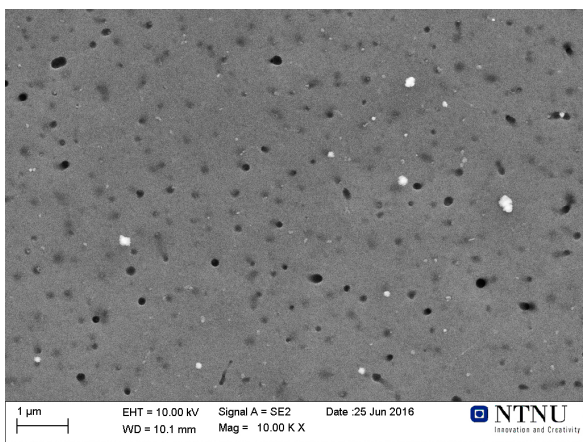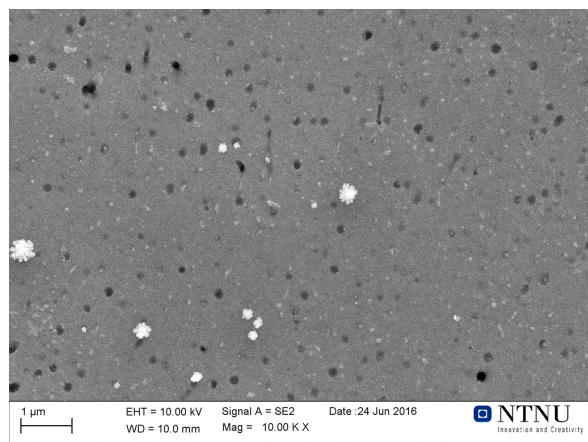
(c) Keller above view.

(d) Keller side view.
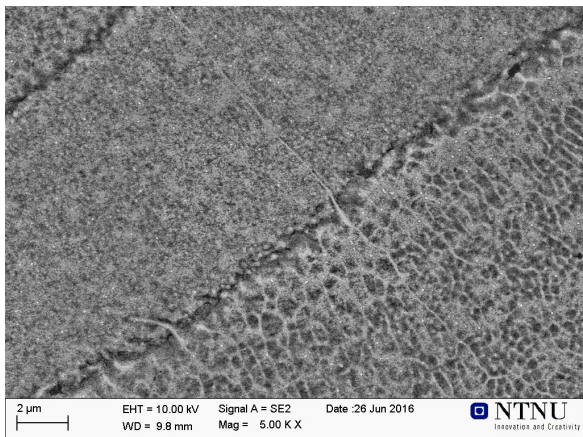
(e) Weck above view.
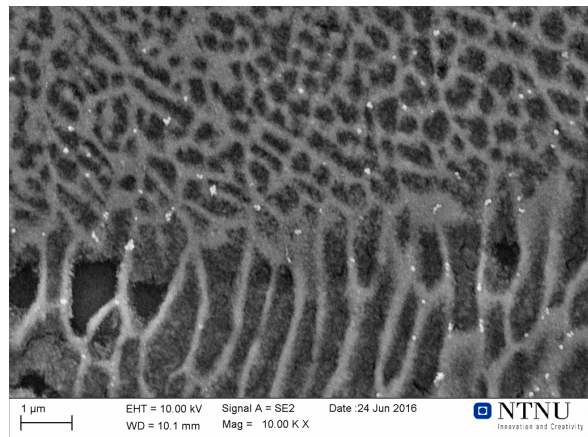
(f) Weck side view.

Figure 4.26: SEM images of AA6061 specimen with various surface preparations.

4.4 Material structure

The macrostructure dominated by porosity has been described in section 4.2. This section is dedicated to the material structure on a smaller scale, focusing on features such as scan tracks and grain structure, with only occasional references to porosity.

4.4.1 AlSi10Mg

The optical micrograph in figure 4.27 shows the above view of an AlSi10Mg sample etched in Keller's etch. The scan tracks clearly go along on of two perpendicular directions, as indicated by the coordinate system in red. These two directions clearly indicate the two scanning directions of the alternating pattern of the scanning strategy. Some of the scan tracks are very long, while others appear nearly circular. This is a result of two factors. First, the polished surface is not perfectly parallel to the fabrication plane. Second, the cross-section is a specific plane that is not perfectly aligned with the top or bottom of a layer. Thus the melt pool geometries may appear more variable than what is actually the case.

The greatest width of a scan track is found to be about 220 μm, while the greatest length extends beyond the image (> 960 μm). Two such measurements are shown in figure 4.27.

The micrograph also shows a peculiar colouration at the scan track boundaries (melt pool contours). The inside of the melt pools (the bulk) appears orange while the contours have a green-blue tint. This is an effect of the etching using Keller's etch during surface preparation. Thus it reveals that the interaction between the etchant and the material is different at the contours compared to the bulk of the melt pools.
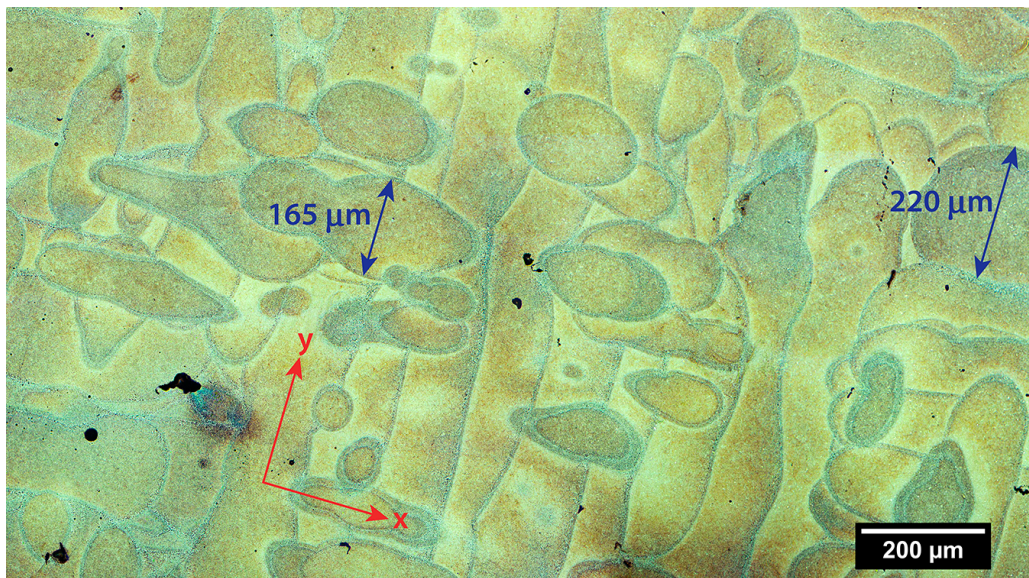
Figure 4.27: OM micrograph of AlSi10Mg above view.

Figure 4.28 shows a similar micrograph for the side view. The coordinate system in yellow shows the building direction (z-axis) and the fabrication plane represented by the xy-axis. Similarly to the case in the above view of figure 4.27, the side view of figure
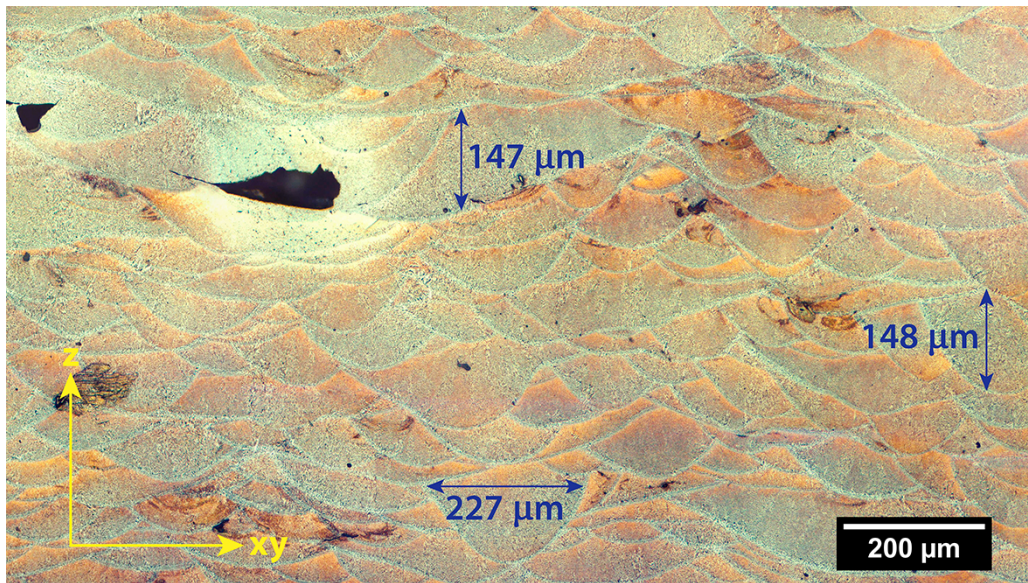
Figure 4.28: OM micrograph of AlSi10Mg side view.

4.28 is not perfectly aligned with a plane perpendicular to the fabrication plane. Again, this is due to the cutting and polishing of the surface which cannot for practical reasons be perfectly aligned to the building direction. The result is that there are two types of scan track geometry in the image. The most numerous is a parabolic geometry, which is quite similar to the structure of arc-welding using multiple passes. The second geometry is much wider along the xy-axis. These two geometries represent the different scanning directions. The parabolic shapes are melt pools oriented roughly normal to the plane of the image, while the long geometries are oriented roughly in the plane of the image.

In the side view of figure 4.28 the maximum scan track width was found to be 227 μm. This is similar to the maximum width found in the above view. In addition, the side view can give an estimate to the penetration depth of the melt pools. As shown in figure 4.28, the maximum height of the scan tracks was measured to be 148 μm. However, all the melt pools are 'cut off' by layers above, so the measured height of the scan track is only a low estimate of the actual penetration depth of the melt pool.

(a)

(b)
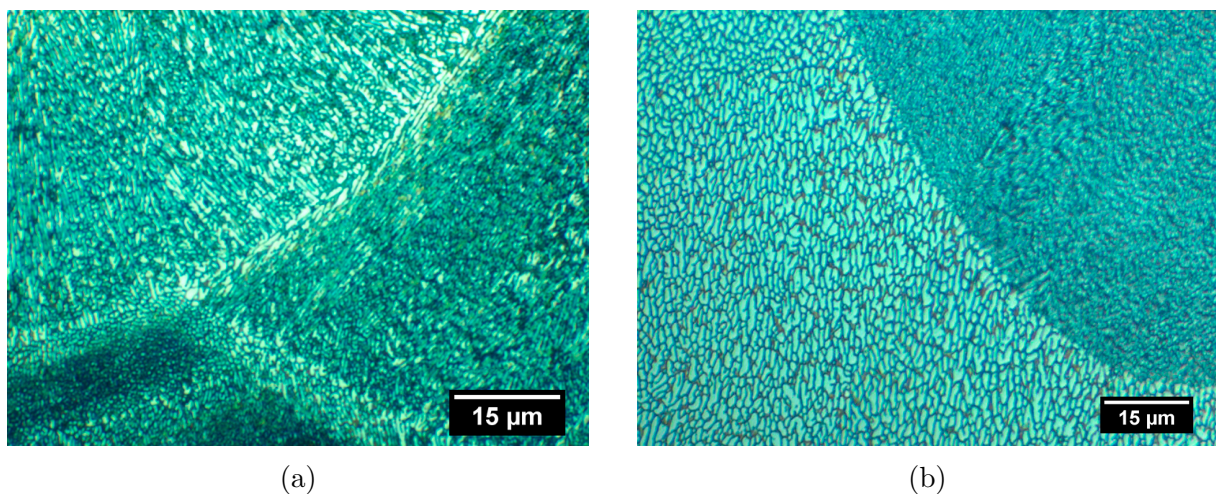
Figure 4.29: OM images of melt pool contours in AlSi10Mg.

Figure 4.29 shows high magnification optical micrographs of the melt pool contours in the AlSi10Mg side view samples etched in Weck's reagent. The figure reveals the cellular microstructure of the material. Figure 4.29a also shows clear signs of epitaxial growth from the melt pool boundary towards the middle.

The grain structure appears to be far more coarse at the melt pool boundary compared to the bulk of the melt pools. This could explain the blue-green tint shown in figures 4.27 and 4.28 at the edges of the scan tracks. The coarser structure at the grain boundary is confirmed by the SEM images of samples etched in Weck's reagent shown in figure 4.30. Note that figures 4.30a and 4.30c is clear evidence of epitaxial growth as the direction of columnar growth is different on either side of the melt pool contours. Figure 4.30d shows that the melt pool contours stop very abruptly at the edges of oxide pores. The contours in all the SEM images are roughly 2-3 μm wide.

(a)

(b)

(c)

(d)
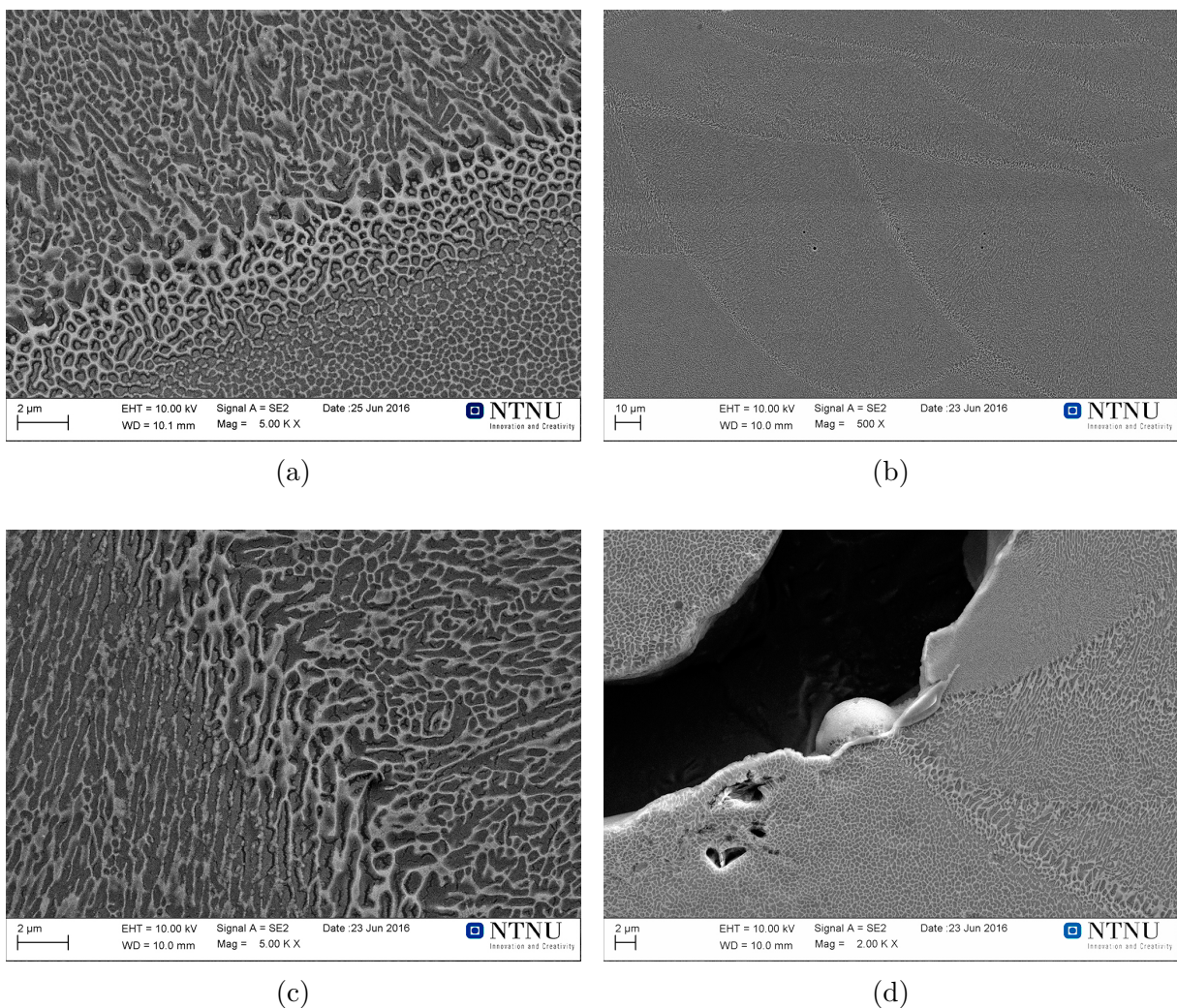
Figure 4.30: SEM images of melt pool contours in AlSi10Mg.
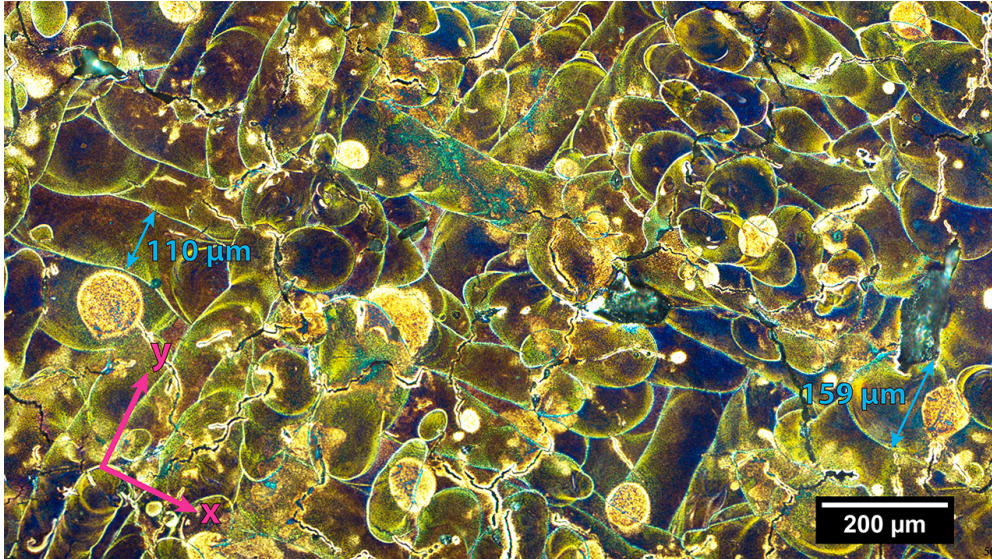
Figure 4.31: OM micrograph of AA6061 above view.

4.4.2 AA6061

Figure 4.31 shows the above view of the sample etched in Weck's reagent. As with the AlSi10Mg specimen, the scan track structure in this orientation shows the two scanning directions clearly. The maximum width was recorded as 159 μm which is considerably less than that of the AlSi10Mg sample. Note also that the melt pools cut to be nearly circular are imaged as very bright.

Figure 4.32 shows the side view of the sample etched in Weck's reagent, again with strong similarities to the AlSi10Mg specimen. However, the scan tracks appear wider in the fabrication plane and shorter in the building direction. The maximum recorded height was 106 μm and the maximum width of 119 μm. However, due to overlapping patterns this is likely much lower values than the actual height and width of the fused zone.
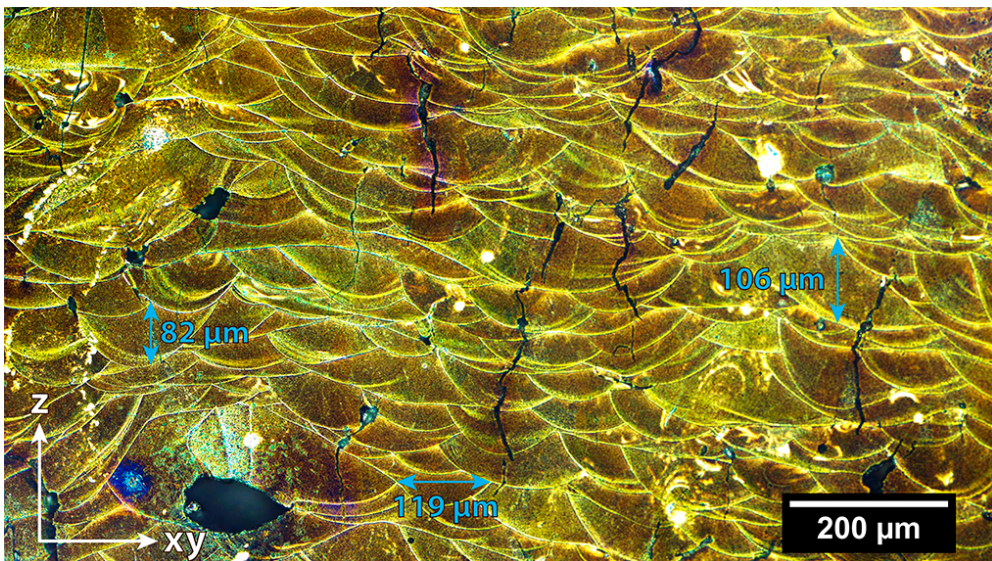
Figure 4.32: OM micrograph of AA6061 side view.
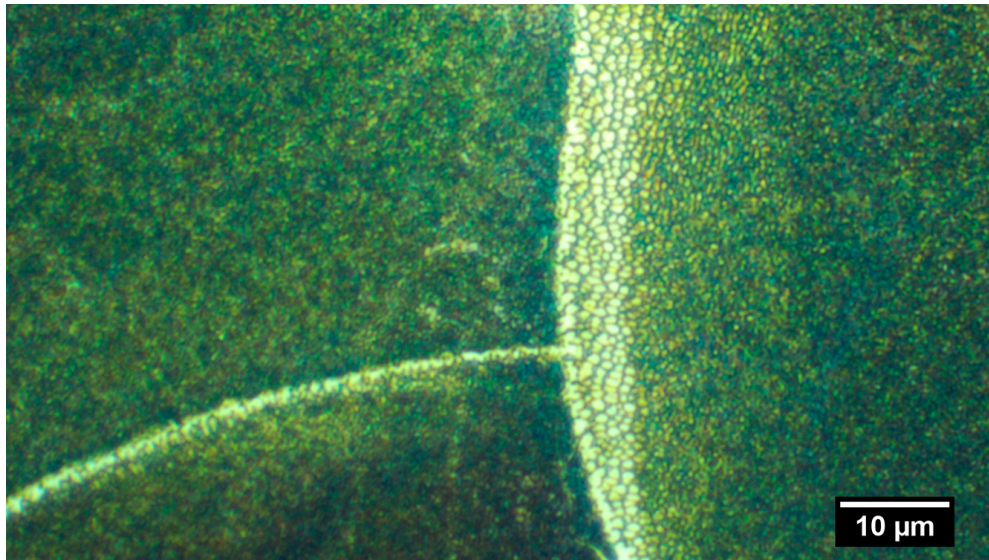
Figure 4.33: OM image of melt pool contour in AA6061.

Figure 4.33 shows a high magnification optical micrograph of melt pool contours in the Weck's etched AA6061 specimen. The cellular structure of the contour is very similar to that of the AlSi10Mg samples. Clearly there is epitaxial growth in the AA6061 specimens. This is confirmed in SEM images of the specimen shown in figure 4.34. The melt pool contours in AA6061 differ from those of AlSi10Mg in that there is a thin line ($\sim 0.2\mu$m thickness) from which epitaxial growth occurs. The width of the band with severely coarser grains is slightly greater too; roughly 6 μm based on the images in figure 4.34.
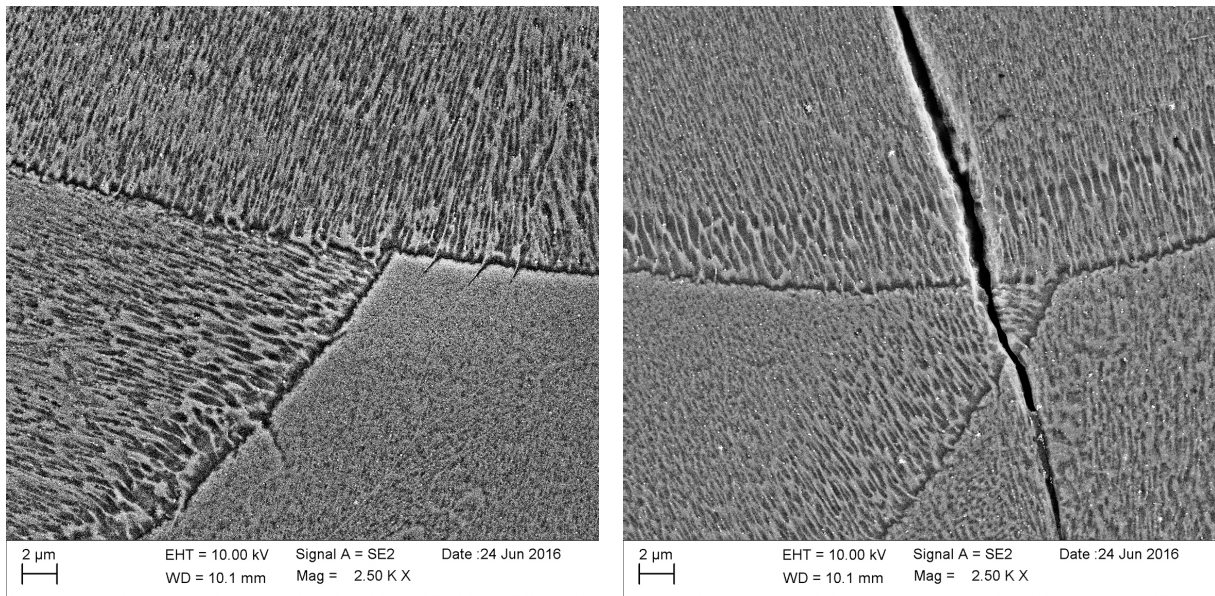
(a)

(b)

Figure 4.34: SEM images of melt pool contours in AA6061.

4.5 Mechanical properties

4.5.1 Fracture during post-processing

The first indication of the relevant mechanical properties of the two materials occurred during part removal from the fabrication platform. Using a hammer and chisel, the AlSi10Mg part was successfully removed as the support structure fractured from the impact of the chisel (see figure 4.35).
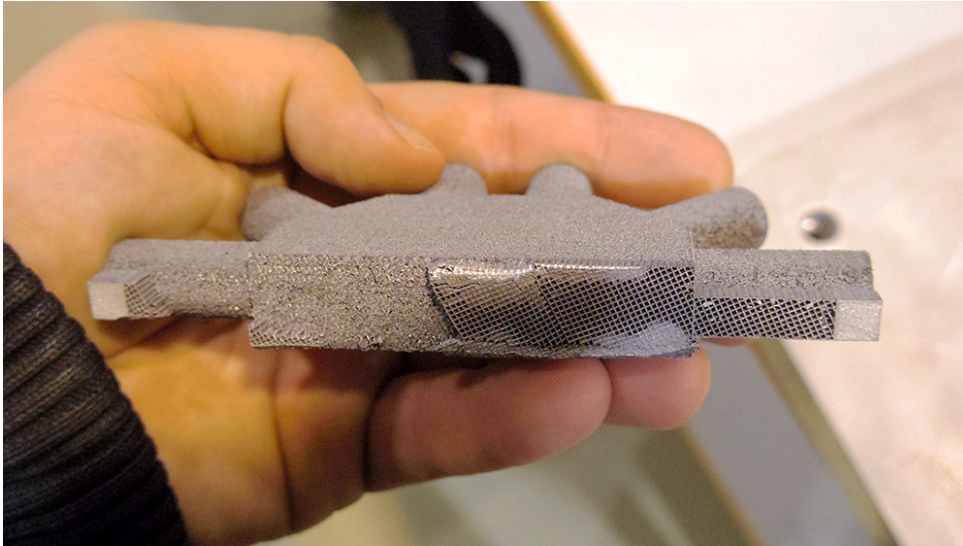
Figure 4.35: AlSi10Mg part after post processing.

However, during removal of AA6061 the cylinder fractured before the support structure. This suggested that AA6061 was a weaker material. Instead the part was removed from the fabrication platform using a saw. The cylinder that tore off was kept as a fracture surface for later studies, while part of the B_{rest} material was used to produce the TT_{90} tensile specimen.

(a) Removal by chisel.
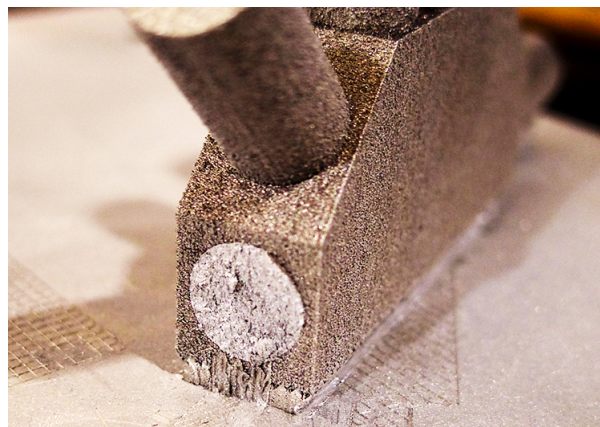
(b) Fracture

Figure 4.36: Fracture of AA6061 part during post processing.

4.5.2 Compression testing
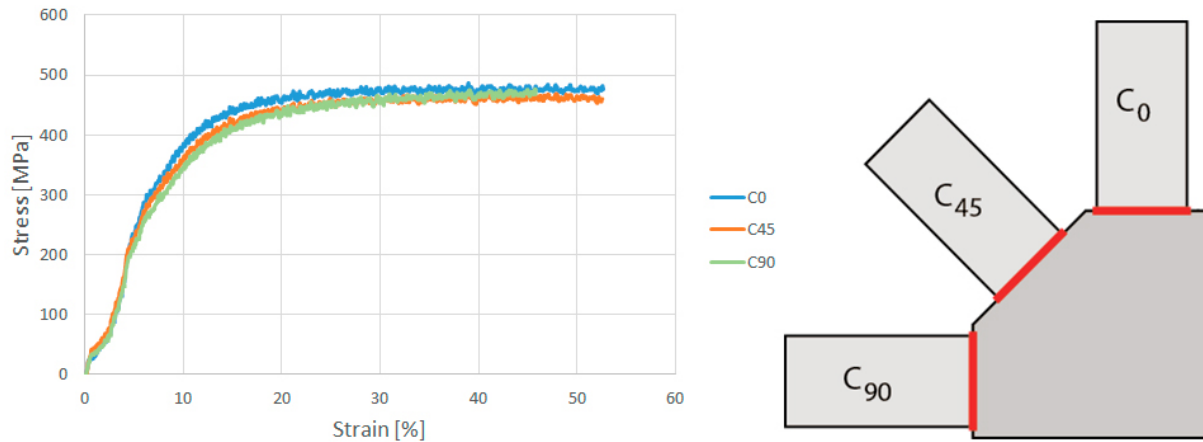
Figure 4.37: Compressive stress-strain plot for AlSi10Mg.

AlSi10Mg

The compressive stress-strain relationship recorded for the AlSi10Mg specimens, along with a diagram of the orientations, is given in figure 4.37. All the orientations show a very similar stress-strain relationship. The specimens were tested in the following order; C_{90}, C_{45} and finally C_0. Loading criterion was set to 64 kN for the first test, which was reached by the C_{90} specimen. For the remaining two specimen toe load criterion was increased to 70 kN. This is why the C_{90} data reaches a lower maximum strain in the figure. The C_{45} specimen fractured at a maximum stress of 471 MPa. Meanwhile the C_0 specimen was stopped due to the time criterion. Images of the specimens after compression testing are given in figure 4.38.

(a) C_0.   (b) C_{45}.   (c) C_{90}.
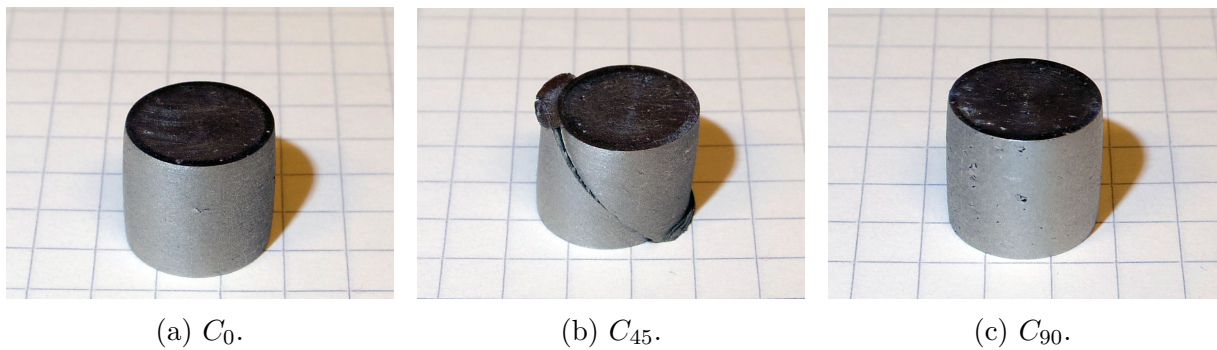
Figure 4.38: AlSi10Mg specimen after compression testing.

AA6061

Figure 4.39 shows the stress-strain relationship for the AA6061 specimens. There is a clear difference in the flow stress of the two materials. The flow stress of AlSi10Mg is roughly twice that of AA6061. Also unlike the plot for AlSi10Mg, there is a subtle indication of anisotropy as the C_{90} plot is a little higher than the other two. For all the AA6061
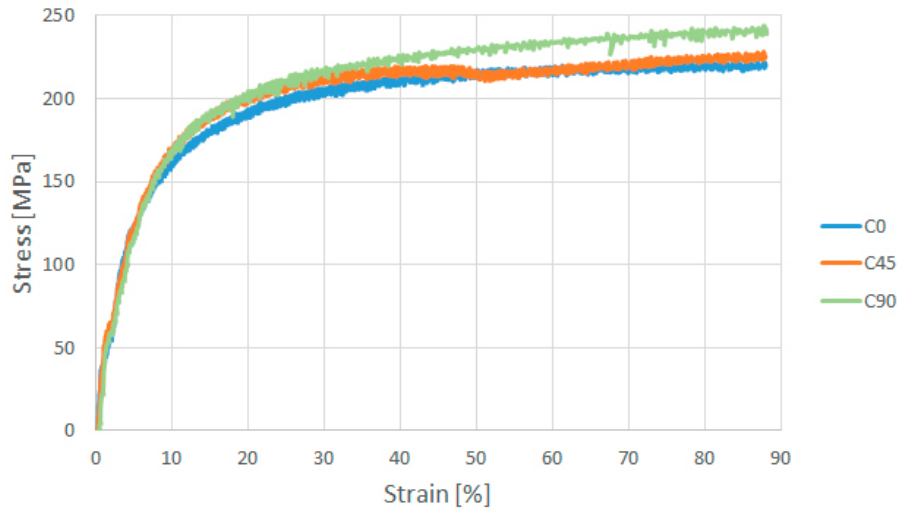
Figure 4.39: Compressive stress-strain plot for AA6061.

specimen the minimum height criterion was breached before the other criteria. Figure 4.40 shows images of the specimen after compression testing. The surfaces of these specimen are rougher than those of AlSi10Mg, and they show signs of barrelling.

(a) C_0.

(b) C_{45}.

(c) C_{90}.
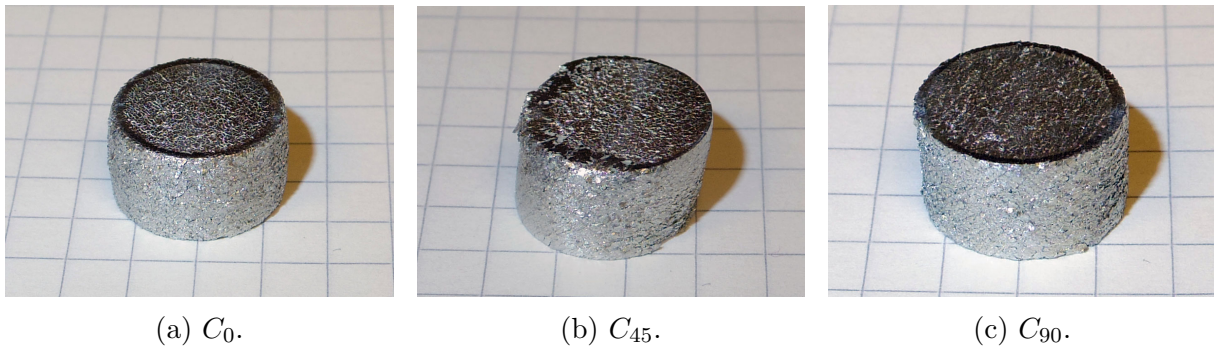
Figure 4.40: AA6061 specimen after compression testing.

Flow stress

The flow stress for each material was calculated as the average of the last 100 datapoints in each series. The results along with the stopping criterion are given in table 4.3. As the AlSi10Mg C_{45} specimen fractured at 471 MPa, the flow stress value of 466 MPa is dubious.

	AlSi10Mg		AA6061	
Specimen	σ_{fl} (MPa)	Stopping criterion	σ_{fl} (MPa)	Stopping criterion
C_0	481	Time	220	Height
C_{45}	466	Fracture	226	Height
C_{90}	471	Load	241	Height

Table 4.3: Results of compression tests.

(a) AlSi10Mg.

(b) AA6061.
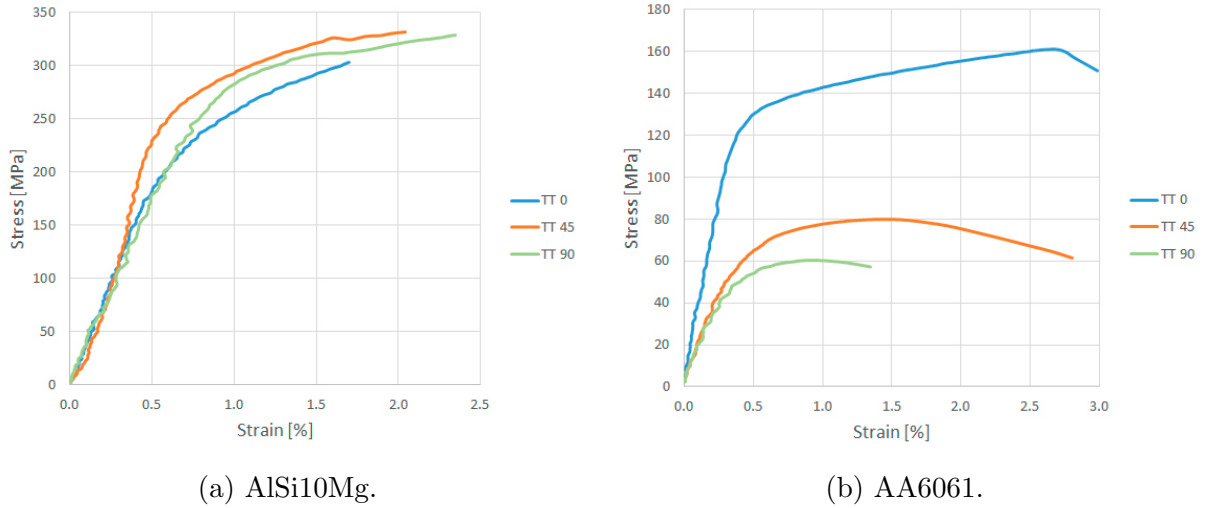
Figure 4.41: Tensile stress-strain plots.

4.5.3 Tensile testing

The tensile stress-strain plots of the two materials are shown in figure 4.41. The plots show that there is a considerable difference in strength between the two materials in tension, as was the case for compression. Also like the case for compression, the AlSi10Mg shows much less clear signs of anisotropy compared to AA6061. There are however some differences. In the compressive tests the C_{90} AA6061 specimen showed slightly greater strength than the other directions. In the tensile tests on the other hand, the TT_{90} AA6061 specimen proved the weakest. A summary of the results are found in table 4.4.

Specimen	AlSi10Mg			AA6061		
	E (GPa)	σ_y (MPa)	σ_{UTS} (MPa)	E (GPa)	σ_y (MPa)	σ_{UTS} (MPa)
TT_0	39	239	303	33	134	161
TT_{45}	43	287	332	18	67	80
TT_{90}	33	288	329	15	56	61

Table 4.4: Results of tensile tests.

5 Discussion

The findings of the experimental work will be considered from several perspectives in this chapter. This thesis was the first investigation of AM aluminium conducted at the Department of Materials Science and Engineering at NTNU. As a result, many of the experimental methods were developed during the time of writing the thesis. The discussion therefore begins with an evaluation of the experimental methods with regard to their practicality and the value of the results. The remainder of the chapter will be a discussion of the results themselves in order to characterize the powders and produced material.

5.1 Evaluation of experimental methods

5.1.1 Powder

Prior to this study the reactivity of the raw material powders was uncertain. As a safety precaution, the powders were first studied in a controlled atmosphere using a glove bag. However, observations from initial work in the glove bag suggested that the powder was not as reactive as initially suspected. While some of the precautions may have been superfluous, the limitations of working in a controlled environment produced a creative solution of analysing the powder; namely casting the powder in epoxy and studying the particles' size and shape using binary images.

Micrographs of the cast samples did not show signs of much reactivity between the powder and the epoxy. Therefore this method of casting may be simplified in future work by removing the glove bag from the process. However, much more powder should be added to the epoxy to avoid removing too much of the sample during sample preparation. The type of epoxy used in this study was clear after hardening, and stirring of the powder was not required for good adhesion of the powder to the mounting. Stirring should therefore be avoided in the future.

The method of stitching micrographs together for a large sample set was effective. By measuring tens of thousands of powder particles, a precise particle size distribution was generated for both powders. There were however some weaknesses of the method. The process was quite time consuming compared to recording only a few micrographs. Despite the resolution of the resulting combined micrograph being very high, the resolution power remained low because of the low magnification objective used. This was a problem because noise in the image was of similar size to the smallest particles, as was clear in the produced size distribution plots.

Once the powders were considered fairly unreactive, they were analysed in a SEM. When compared to the SEM micrographs, the resolution of the OM samples is very low. Thus the SEM micrographs were more useful to describe the geometry of the powder particles, and they also gave a good indication of the size distribution as well. However, casting the powders enabled capturing images of the particles' interior, something not possible in a SEM.

5.1.2 Component model and production

The design of the component successfully achieved its three goals; being suitable for material characterization, containing extra material (a symmetrical design) and serving as a demonstration piece. In this study only the above and side view orientations were studied in detail, but the 45° orientation may in future provide further insight into the structure. All cylinders were used for mechanical testing except for the cylinder torn off during removal from the fabrication platform. Instead material from the base of the component was used to produce the tensile specimen. Future removal should be done more carefully by using another method such as wire EDM to avoid damaging the component. The main drawback to this design is the material waste. By only printing the sections of the specimen to be evaluated, less machining of specimen would be required, reducing production costs.

5.1.3 Etchants

Little research has been done to find suitable surface preparations for AM aluminium samples. Most research on AM aluminium is focused on AlSi alloys, for which etching in Keller's reagent is suitable. However, this preparation is not suitable for al other aluminium samples, as shown in this study.

An overview of the results from the surface preparation evaluation is shown in table 5.1. A polished sample is suitable for evaluating porosity, but does not reveal the scan tracks or the microstructure. Weck's reagent provided the best samples for both materials for SEM analysis. Keller's etch is suitable for AlSi10Mg but not for AA6061. Weck's reagent on the other hand s suitable for both AlSi10Mg and AA6061, but the colouration provides so much contrast that Weck's is unsuitable for evaluating porosity.

	AlSi10Mg			AA6061		
Investigation	Polished	Keller	Weck	Polished	Keller	Weck
OM - Porosity	Excellent	Good	Poor	Excelent	Good	Poor
OM - Scan tracks	Poor	Excellent	Good	Poor	Poor	Good
OM - Microstructure	Poor	Good	Good	Poor	Poor	Good
SEM	Poor	Good	Excellent	Poor	Poor	Excellent

Table 5.1: Overview of surface preparation evaluation.

5.1.4 Binary image analysis

Binary image analysis of combined micrographs was conducted to systematically investigate porosity in the samples. The analysis categorized different types of porosity fairly well, with the notable exception of metallurgical porosity. The flaw was to assume metallurgical porosity to be within the size range of 7-62 μm (area of 40-3000 μm^2). However, later SEM micrographs showed that most metallurgical porosity is much smaller. The method may be improved by using higher magnification micrographs, but this will in turn require many more micrographs to be recorded and stitched together to cover the same surface area of the specimen.

Large oxide pores containing unmelted powder particles were revealed in both materials by SEM micrographs. In addition, similar oxide pores that did not contain unmelted powder was also found in both materials. Meanwhile in the binary images, the large oxides could be identified, but unfortunately no method was found to distinguish between oxide pores containing and not containing unmelted powder. Nonetheless, the SEM micrographs suggest that the smallest pores containing unmelted powders are of a size on the same order of magnitude as the proposed limit of 3000 μm^2.

Where the binary image analysis excelled was in quantifying the fraction of the porosity caused by the different types of pores. No comparable result was found in the literature study. Most relevant literature focuses on AlSi10Mg alloys, meaning crack initiation and growth in AM aluminium has not received much attention. This binary image analysis can quantify the shape, size and orientation of the cracks as well as their average distance from each other.

5.1.5 Mechanical testing

As previously described, the limited amount of material was a challenge for mechanical testing. In comparison to standard specimen dimensions commonly used in material testing, the specimen in this study were relatively small. Particularly the tensile specimen were tested over a very limited cross-section. Both the compression and tensile specimen were an integral part of the component design. The design was made in advance of any material characterization, so the amount of porosity (particularly in the AA6061 material) was unexpected. As such material defects are not homogeneously spread in the material, the uncertainty of the measured strength is very high.

For future work, both the quantity and size of specimen should be increased to evaluate the material's properties with more precision. The results from this thesis give only a rough estimate. Standard practice is to test at least three specimen. Given that three orientations were evaluated in this study, a total of at least nine specimen should have been prepared for a reliable evaluation of the mechanical properties of the material.

5.2 Characterization of powders

5.2.1 Reactivity of powder

Neither of the powders showed any noticeable signs of reaction when exposed to either air or water. The conditions were the same for all the cases; the powder was delivered in a sealed container filled with an inert gas. The container was opened inside the glove bag filled with nitrogen. After staying in the glove bag for about 12 hours the powders were taken out of the bag into atmospheric surroundings and then aquatic surroundings.

One explanation for the lack of reaction is that the powders may already have been exposed to oxygen. Despite repeating the process of evacuating and then filling the glove bag several times, there will always be a small amount of residual oxygen. Only a very small amount of oxygen is required to produce a protective film around the powder particles. The AlSi10Mg powder in particular may have been exposed to oxygen before it was delivered to the author. This powder was used and recycled multiple times in previous productions. As with the glove bag, there is always a little residual oxygen in the PBF machine. In either case, a thin oxide layer on the particle surfaces would discourage a violet reaction as there is less surface for oxygen to react width. This explanation would also help explain the porosity of the AlSi10Mg product material. Oxide layers around unmelted powder may have discouraged wetting sufficiently to produce oxide pores, as proposed by Louvis, Fox, and Sutcliffe [8].

Another explanation for why no noticeable reaction took place is that the powder particles are too large to react violently. The binary analysis of the powders indicated that the median particle sizes of AlSi10Mg and AA6061 were 31.7 and 28.2 μm respectively. That means half of all the powder particles are larger than this value. The volumetric fraction of powders greater than these sizes would be far greater than 50%. It may be that a few small particles reacted with oxygen, but the heat was absorbed by larger nearby particles. Thus stopping the reaction from spreading.

5.2.2 Size and circularity distribution

Powder	Given range	Average	Median	Peak	Standard deviation
AlSi10Mg	25-53 μm	36.4 μm	31.7 μm	15$\pm$0.5 μm	22.2 μm
AA6061	20-63 μm	32.8 μm	28.2 μm	21 $\pm$0.5μm	19.0 μm

Table 5.2: Given vs measured data of powder size.

Table 5.2 compares the given size range to the measured size parameters for the two powders. Note that the peak frequency of AlSi10Mg is outside the given range, while the peak of AA6061 is at the lower edge of the range. These data are based on the OM micrographs where particles of area less than 25 μm^2 (size less than 5.6 μm) are filtered out of the dataset. That could mean the measured data is an overestimate if too many small particles were filtered away.

The small powder size of AlSi10Mg may partly be attributed to the recycling of the powder which is known to deform and sometimes fracture particles. The AA6061 powder

however was newly received from the supplier and had never been used in production before. It may be that the size range is based on the volumetric fraction rather than the frequency.

For both materials the average powder particle size is greater than the layer thickness used for the production of the components ($\Delta z_{\text{layer}} = 30 \mu$m). This means the deposited layers are to a large extent only one powder particle in height. The packing factor will be increased if smaller particles are deposited alongside larger ones to fill voids between large particles.

The circularity of AA6061 is greater than that of AlSi10Mg. That may be caused by variations in production of the two suppliers, but this may also be characteristic of AA6061 being a fresh powder while AlSi10Mg has been recycled a number of times. The SEM micrographs of AlSi10Mg show particles that look deformed rather than fractured.

5.3 Characterization of materials

5.3.1 Porosity

The relative density measurements are in line with findings from other studies. AlSi10Mg parts usually have relative densities of 95-99.9%, and the average of the four samples (two above view and two side view) was 97.1%. AA6061 samples have been found be of 80-89% relative density in the literature, and this sample was recorded as 87.5%. Both of these densities rely on the assumption that the area fraction is roughly equal to the volume fraction of pores. Although the characteristics of the different pore types were found in literature, this type of quantitative analysis was absent.

The two orientations of AlSi10Mg had nearly identical amounts of metalugical pores, cracks and disrupted oxides, while there were more large oxides found in the above view than side view. The amount of metallurgical pores and disrupted oxides in AA6061 were similar in the above and side views, while the amount of cracks and large oxides were less similar. In total the above view was the slightly more porous in both materials.

The metallurgical pores were very small in both samples. SEM analyses found to be in the range of 0.5-3 μm in AlSi10Mg samples, but in a larger range of 0.5-10 μm in AA6061 samples. There are several possible explanations for this. The AA6061 melt pool may have dissolved more gases, or have solidified more quickly blocking the escape of the bubbles. Another explanation is that because the AA6061 material is weaker, it will yield more space to an equivalent bubble in AlSi10Mg of the same pressure. Yet another explanation is that this is simply a statistical anomaly as only a handful of metallurgical pores were examined from each sample in SEM.

The AA6061 samples contain considerably more of every pore type than the AlSi10Mg samples. Unfortunately, the data could not determine if one of the materials had more large oxide pores containing unmelted powders. However, the SEM micrographs did observe such pores in both materials. This means that both materials experienced occasional lack of fusion in production.

5.3.2 Cracks

The amount of cracks is the largest difference between the porosity characteristics of the two materials. Cracks were negligible in the AlSi10Mg samples (0.04%), but prevalent in the AA6061 samples (6.9% on average). There are two major differences between the materials. One is the powder geometry, the other is the composition. Given that the cracks often span over several hundred micron, they seem unlikely to be caused by powder geometry. Differences in composition makes much more sense. AlSi alloys are suitable for casting in part because silicon expands while aluminium shrinks during solidification. Thus the silicon counteracts the overall shrinkage. Given that the AlSi10Mg alloy contains roughly 15 times more silicon than AA6061, this could be decisive with regard to crack growth. In addition, the cracks look a lot like cracks produced from hot cracking found in fusion welding. Hot cracking is known to be caused by solidification shrinkage of alloys with large solidification intervals and high solidification shrinkage. Therefore the difference is solidification shrinkage between the alloys is a strong candidate for explaining the difference in porosity characteristics between the alloys.

In the above view, the cracks formed in what appears to be random orientations. In the side view on the other hand, the cracks were clearly oriented along the building direction. Despite the very different crack structure, the two orientations had a nearly identical distribution of nearest neighbour distances between cracks. The most frequent distance between cracks was 107μm with a standard deviation of 40 μm. This is in the range of both the hatching distance (Δy_h= 105 μm), the spot size (d_{spot}=150μm) as well as the scan track width and depth found in the OM micrographs of AA6061. For now it is unclear if any of these parameters correlate with the crack nearest neighbour distance.

5.3.3 Scan tracks

The scan tracks are the traces of the weld pools, but they also reflect information of the production process. Studying the scan tracks is therefore a way to connect the production process parameters to the metallurgical process occurring on a much smaller scale. Such were the results in this study.

The scan tracks revealed the alternating pattern of the scanning strategy when imaged using optical micrographs. At this large scale the scan track width and height could be measured. For AlSi10Mg, the widest tracks were found to be roughly 220 μm while the largest height was found to be 148μm. For AA6061, the widest scan track was 159 μm and the greatest height was found to be 106 μm. Note that the width and height of the scan tracks are not the same as the fusion width and penetration depth of the melt pool because the upper part of the melt pool has been remelted by the layer above. They do however serve as minimum values. The scan track width are different from each other, but both greater than the laser spot size. This means the spacial resolution of AM parts is strongly material dependent. Also note that because the scan track height is more than three times the layer thickness, the penetration depth of the melt pool must be even greater. That means all parts of the bulk material are melted and remelted several times.

There is much to gain if the melt pool geometry can be deduced from the scan tracks because of the similarities to fusion welding. Models for heat flow in fusion welding have been developed for many decades, and because they are based on principles of physics

such as the heat equation, they may be applicable for PBF processes. However, the size and time scales are much smaller in PBF processes compared to fusion welding. For example, the scanning speed for producing this part was 800 mm/s, which is much faster than any normal welding speed.

5.3.4 Microstructure

Studying the scan tracks of the AlSi10Mg samples at high resolution (using both SEM or OM), the characteristic melt pool contour microstructure was observed. Such epitaxial growth in AlSi10Mg has been documented by several recent research articles [10, 23]. This fine grained structure is often referred to as 'cellular' and attributed to the precipitation of silicon from the aluminium α-phase during the rapid solidification of the melt pool. The most coarse cellular structure was found where several melt pore contours met. This is where the material is heated to just below the melting point several times allowing much silicon do diffuse out of the α-phase without being absorbed by the melt. The largest cells were found to be several micron in diameter and the cell walls would reach over 800 nm. The cell size quickly diminished with distance from the melt pool contours. In the middle of the melt pools, the structure was much finer with a cell size of roughly 200 nm.

Epitaxial growth was also observed when studying the AA6061 samples in a similar manner at high resolution. A cellular structure much like that found in the AlSi10Mg samples was observed at the melt pool contours. The AA6061 alloy does not contain enough alloying elements for the cell walls to be precipitated phases. Instead, the micrographs must be showing the grain structure of the α-phase. That means the cellular epitaxial structure is a consequence of the thermal conditions in the rapidly solidifying melt pool. This is in line with solidification theory for a high crystal growth rate. The columnar structure is visible up to a distance of roughly 6 μm from the contour. After this the structure changes abruptly to cells not easily resolved in the SEM.

5.3.5 Mechanical properties

The flow stress of AlSi10Mg was found to be more than twice that of AA6061. The resistance to flow may in part be explained by the solid solution strengthening that silicon provides when dissolved in the α-phase. In addition, the silicon precipitates provide secondary phases that increase the amount of phase boundaries in the material. The material has been characterized as very fine-grained with α-phase cells surrounded by silicon precipitates. Thus the strength of AlSi10Mg comes from solution strengthening, secondary phase strengthening as well as a fine grain structure.

Meanwhile the AA6061 structure is limited to one phase. Due to the rapid solidification of the PBF process, all alloying elements are likely in supersaturated solid solution (SSSS). No clearly secondary phases such as β'' or β' were visible in the SEM micrographs. The alloy is strengthened by a fine structure, but weakened by severe porosity. During the compression test the pores would have collapsed which may explain why the surfaces of the compressed specimens as much rougher than those of the AlSi10Mg compression specimens. The crack structure may also explain why the C_{90} specimen showed greater

strength than that of the other two specimen. The cracks were oriented normal to the compression direction for this specimen and would therefore collapse quickly.

The crack orientation may also explain why the yield strength of the TT_0 was so much greater than that of TT_{45} and TT_{90}. For the latter two, the cracks were at 45° and perpendicular to the direction of the tensile stress. Stress concentrated around crack tips would easily initiate crack growth and lead to fracture. Meanwhile the TT_0 with cracks roughly parallel to the direction of stress showed a strength more than twice that of the others.

Meanwhile the AlSi10Mg specimen were found to have considerable strength. The ultimate tensile strengths of the TT_0, TT_{45} and TT_{90} AlSi10Mg specimen were found to be 239, 287 and 288 MPa respectively, which is quite comparable a T6 tempered 359.0 casting alloy with an ultimate tensile strength of 275 MPa.

6   Conclusion

From this investigation of an AlSi10Mg and an AA6061 aluminium apllow powder and the components produced from them by a PBF-process the following conclusions may be drawn:

- The powders did not pose a serious fire or explosion hazard as long as they are handled with care.

- Binary image analyses of rasters of merged optical micrographs of the powders were successful in producing the size and circularity distributions of the powders. The AlSi10Mg powder was found to have an average diameter of 36.4 μm and an average circularity of 0.67. The AA6061 powder was found to have an average diameter of 32.8μm and an average circularity of 0.73

- SEM analyses are more practical and provide better images of the powders with regard to geometry

- The relative density of polished samples of AlSi10Mg was found to be 97.9%. The porosity was oxide pores of diameters greater than 60 μm, some of which contained unmelted powders.

- The relative density of polished samples of AA6061 was found to be 87.5%. The porosity was mostly cracks, which were oriented randomly in the fabricaion plane and along the building axis.

- Keller's etch was well suited to resolve the scan tracks of AlSi10Mg but not for AA6061. Weck's reagent was well suited for etching both materials.

- Epitaxial growth was found in both samples. This suggests that the melt pool contour structure arises from the thermal conditions during solidification to a large degree, and of alloy composition to a lesser degree.

References

[1]   Carl Brancher. "Additive and the ideal of 'batch of one' manufacture". In: *Metal Powder Report* (2016).

[2]   Todd M. Mower and Michael J. Long. "Mechanical behavior of additive manufactured, powder-bed laser-fused materials". In: *Materials Science and Engineering: A* 651 (2016), pp. 198–213.

[3]   Ian Gibson, David Rosen, and Bret Stucker. *Additive Manufacturing Technologies. 3D printing, Rapid Prototyping, and Direct Digital Manufacturing.* 2nd ed. Springer, 2015.

[4]   Chee Kai Chua and Kah Fai Leong. *3D Printing and Additive Manufacturing. Principles and Applications.* 4th ed. World Scientific, 2015.

[5]   Stephen Mellor, Liang Hao, and David Zhang. "Additive manufacturing: A framework for implementation". In: *International Journal of Production Economics* 149 (2014), pp. 194–201.

[6]   Eleonora Atzeni and Alessandro Salmi. "Economics of additive manufacturing for end-usable metal parts". In: *The International Journal of Advanced Manufacturing Technology* 62.9 (2012), pp. 1147–1155.

[7]   Donald R. Askeland and Pradeep P. Phulé. *The Science and Engineering of Materials.* Cengage learning, 2008.

[8]   Eleftherios Louvis, Peter Fox, and Christopher J. Sutcliffe. "Selective laser melting of aluminium components". In: *Journal of Materials Processing Technology* 211.2 (2011), pp. 275–284.

[9]   K. G. Prashanth et al. "Microstructure and mechanical properties of Al–12Si produced by selective laser melting: Effect of heat treatment". In: *Materials Science and Engineering: A* 590 (2014), pp. 153–160.

[10]   Chunze Yan et al. "Microstructure and mechanical properties of aluminium alloy cellular lattice structures manufactured by direct metal laser sintering". In: *Materials Science and Engineering: A* 628 (2015), pp. 238–246.

[11]   Nesma T. Aboulkhair et al. "Reducing porosity in AlSi10Mg parts processed by selective laser melting". In: *Additive Manufacturing* 1–4 (2014), pp. 77–86.

[12]   D. Buchbinder et al. "High Power Selective Laser Melting (HP SLM) of Aluminum Parts". In: *Physics Procedia* 12, Part A (2011), pp. 271–278.

[13]   ASTM. *Standard Specification for Aluminum-Alloy 6061-T6 Standard Structural Profiles.* Standard B308/B308M-10. West Conshohocken, PA: ASTM International, 2010.

[14]   ISO/ASTM. *Standard Terminology for Additive Manufacturing.* Standard 52900-15. West Conshohocken, PA: ASTM International, 2015.

[15]   The Economist. *Heavy metal. Three-dimensional printing may help entrench the world's engineering giants.* Berlin, 2014.

[16]   CGTrader. *Eiffel Tower High detailed*. Published by user *'squir'*. Nov. 2014. URL: `www.cgtrader.com/3d-models/architectural-exterior/landmark/eiffel-tower-high-detailed` (visited on 02/07/2016).

[17]   Thingiverse. *Eiffel tower*. Published by user *'Newcandle'*. July 2015. URL: `http://www.thingiverse.com/thing:912478` (visited on 03/07/2016).

[18]   Lucas Mearian. *Review: LulzBot Mini 3D printer delivers outstanding details*. Jan. 2015. URL: `http://www.computerworld.com/article/2868817/review-lulzbot-mini-3d-printer-delivers-outstanding-details.html` (visited on 01/07/2016).

[19]   EOS e-Manufacturing Solutions. *Additive Manufacturing, Laser-Sintering and industrial 3D printing - Benefits and Functional Principle*. URL: `http://www.eos.info/additive_manufacturing/for_technology_interested` (visited on 03/07/2016).

[20]   Stratasys Direct Manufacturing. *Direct Metal Laser Sintering*. URL: `https://www.stratasysdirect.com/solutions/direct-metal-laser-sintering/` (visited on 03/07/2016).

[21]   Loong-Ee Loh et al. "Numerical investigation and an effective modelling on the Selective Laser Melting (SLM) process with aluminium alloy 6061". In: *International Journal of Heat and Mass Transfer* 80 (2015), pp. 288–300.

[22]   Manickavasagam Krishnan et al. "On the effect of process parameters on properties of AlSi10Mg parts produced by DMLS". In: *Rapid Prototyping Journal* 20.6 (2014), pp. 449–458.

[23]   Diego Manfredi et al. "From Powders to Dense Metal Parts: Characterization of a Commercial AlSiMg Alloy Processed through Direct Metal Laser Sintering". In: *Materials* 6.3 (2013), p. 856.

[24]   Jan Ketil Solberg. *Teknologiske Metaller og Legeringer*. NTNU, 2010.

[25]   Jon Holmestad. "Scanning Transmission Electron Microscopy Studies of Grain Boundary Segregation relevant to Intergranular Corrosion in Al-Mg-Si-Cu Alloys". Norwegian University of Science and Technology, Jan. 2015.

[26]   Gene Mathers. *The welding of aluminium and its alloys*. Woodhead Publishing, 2002. ISBN: 1855735679.

[27]   Baker et al. *ASM Handbook, Volume 03 - Alloy Phase Diagrams*. ASM International, 1992. ISBN: 978-0-87170-381-1.

[28]   J. Zhang et al. "Equilibrium pseudobinary Al–Mg2Si phase diagram". In: *Materials Science and Technology* 17.5 (2001), pp. 494–496.

[29]   Kim Blommedal. "Corrosion Development in Welded AA6082 Alloys". Norwegian University of Science and Technology, June 2013.

[30]   Gordon Aylward and Tristan Findlay. *SI Chemical Data*. 6th ed. John Wiley & Sons, Inc, 2008. ISBN: 9780470816387.

[31]   R. Winston Revie and Herbert H. Uhlig. *Corrosion and Corrosion Control: An Introduction to Corrosion Science and Engineering*. John Wiley & Sons, Inc, 2008. ISBN: 9780471732792.

[32]   Paul L. Miller and Ana Navarro. "Hazardous Reactions of Aluminum Powder with Water in the Propellant, Explosive and Pyrotechnic (PEP) Industries". In: *United States Defense Technical Information Center* (1996).

[33]   J. F. Lancaster. *Metallurgy of welding*. 6th ed. Abington Publishing, 1999. ISBN: 1855734281.

[34]   Einar Braathu. *Metallurgisk ordbok*. 2nd ed. NORGRAF AS, 2003. ISBN: 8291466033.

[35]   Øystein Grong. *Metallurgical Modelling of Welding*. The Institute of Materials, 1997. ISBN: 1861250363.

[36] A. B. Spierings, M. Schneider, and R. Eggenberger. "Comparison of density measurement techniques for additive manufactured metallic parts". In: *Rapid Prototyping Journal* 17.5 (2011), pp. 380–386.

[37] Lore Thijs et al. "Fine-structured aluminium products with controllable texture by selective laser melting of pre-alloyed AlSi10Mg powder". In: *Acta Materialia* 61.5 (2013), pp. 1809–1819.

[38] Erhard Brandl et al. "Additive manufactured AlSi10Mg samples using Selective Laser Melting (SLM): Microstructure, high cycle fatigue, and fracture behavior". In: *Materials & Design* 34 (2012), pp. 159–169.

[39] Karolien Kempen et al. "Mechanical Properties of AlSi10Mg Produced by Selective Laser Melting". In: *Physics Procedia* 39 (2012), pp. 439–446.

[40] Konrad Bartkowiak et al. "New Developments of Laser Processing Aluminium Alloys via Additive Manufacturing Technique". In: *Physics Procedia* 12, Part A (2011), pp. 393–401.

[41] Ulrich Albanus and Matthias Hofmann. *Safety Requirements for LaserCUSING*. Presentation. Lichtenfels, Germany.

[42] ASTM. *Standard Practice for Microetching Metals and Alloys*. Standard E407-07. West Conshohocken, PA: ASTM International, 2015.

[43] Li Gao, Yohei Harada, and Shinji Kumai. "Microstructural characterization of aluminum alloys using Weck's reagent, part I: Applications". In: *Materials Characterization* 107 (2015), pp. 426–433.

[44] G.P. Dinda, A.K. Dasgupta, and J. Mazumder. "Evolution of microstructure in laser deposited Al–11.28%Si alloy". In: *Surface and Coatings Technology* 206.8–9 (2012), pp. 2152–2160.

[45] ConceptLaser GmbH. *CL 30AL/CL 31AL. Aluminium alloy.* Material data sheet. Lichenfels, Germany, 2012. URL: http://www.conceptlaserinc.com/wp-content/uploads/2014/10/CL-AL30_31AL_Englisch.pdf (visited on 07/07/2016).

[46] ASTM. *Standard Specification for Aluminum-Alloy Permanent Mold Castings*. Standard B108/B108M. West Conshohocken, PA: ASTM International, 2015.

[47] E. Atzeni et al. "Abrasive Fluidized Bed (AFB) finishing of AlSi10Mg substrates manufactured by Direct Metal Laser Sintering (DMLS)". In: *Additive Manufacturing* 10 (2016), pp. 15–23.

[48] W. King et al. "Overview of modelling and simulation of metal powder bed fusion process at Lawrence Livermore National Laboratory". In: *Materials Science and Technology* 31.8 (2015), pp. 957–968.

[49] F. Verhaeghe et al. "A pragmatic model for selective laser melting with evaporation". In: *Acta Materialia* 57.20 (2009), pp. 6006–6012.

[50] LPW Technolgy Ltd. *LPW Company Brochure. Total Powder Management.* Promotional Brochure. Cheshire, UK, 2015. URL: http://www.lpwtechnology.com/cms/lpw-content/uploads/2016/02/V.001-LPW-Company-Brochure.pdf (visited on 07/10/2016).

[51] Autodesk Inc. *AutoCAD. Design every detail.* 2016. URL: http://www.autodesk.com/products/autocad/overview (visited on 07/01/2016).

[52] Struers. *EpoFix Kit. 1 l resin, 130 ml hardener and required consumables (40200029).* 2016. URL: https://e-shop.struers.com/CA/EN/products/Mounting/Cold_mounting_resin/EpoFix_Kit_1_l_resin_130_ml_hardener_and_required_consumables(40200029).aspx (visited on 03/01/2016).

[53] Sigma-Aldrich. *Aldrich Atmosbag. Two-hand, non-sterile, size S, closure type, Zipper-lock.* 2016. URL: `http://www.sigmaaldrich.com/catalog/product/aldrich/z530204` (visited on 02/25/2016).

[54] Struers. *OP-S. Standard colloidal silica suspension for final polishing (40700000).* 2016. URL: `https://e-shop.struers.com/FI/EN/products/Polishing/Silica_Oxide/OP-S_004_m_1_l(40700000).aspx` (visited on 03/02/2016).

[55] Adobe System Inc. *Adobe Photoshop CC.* 2016. URL: `http://www.adobe.com/products/photoshop.html` (visited on 05/02/2016).

[56] *ImageJ.* 2016. URL: `https://imagej.nih.gov/ij/index.html` (visited on 05/20/2016).

[57] Yuxiong Mao. *Nearest Neighbor Distances Calculation with ImageJ.* 2016. URL: `https://icme.hpc.msstate.edu/mediawiki/index.php/Nearest_Neighbor_Distances_Calculation_with_ImageJ` (visited on 05/28/2016).

[58] Henry S. Valberg. *Applied Metal Forming. Including FEM Analysis.* Cambridge University Press, 2010.